POLITECNICO DI TORINO

Master's Degree in Biomedical Engineering

Master's Degree Thesis

Alpha Binaural Beats and Brain Entrainment: A Machine Learning-Based Assessment of Short-Term Effects

Supervisors	Candidates
Prof. Luca MESIN	Riccardo CAPELLI
Ing. Matteo RAGGI	Leonardo DONATI

A.Y. 2024/2025

Summary

In recent years, binaural beats (BBs) have attracted growing interest in the scientific community for their potential to non-invasively modulate brain activity, based on the brainwave entrainment hypothesis. BBs are an auditory phenomenon that occurs when two tones of slightly different frequencies are presented separately to each ear, and the brain perceives a third tone corresponding to the frequency difference. Numerous studies suggest that such stimulation can influence neurophysiological parameters and mental states related to relaxation, attention, and emotional regulation. However, current literature is highly heterogeneous in terms of protocols, frequencies, duration, and results, with most studies focusing on prolonged stimulation ($\geq$10 minutes).

This study aims to explore the efficacy of a brief (1-minute) alpha-band (7–13 Hz) stimulation to evaluate the emergence of short-term neurophysiological effects and gain insights into rapid activation mechanisms. The experiment involved 14 subjects (mean age: 23.8 $\pm$ 2.5 years) who participated in two sessions separated by a 5-minute rest period, with simultaneous electroencephalography (EEG) and electrocardiography (ECG) recordings during exposure to BBs and a sham condition, using a personalized protocol based on each participant's Individual Alpha Frequency (IAF).

Each 10-minute session alternated BBs and sham segments, delivered via JBL headphones in a quiet room, with participants' eyes closed and monitored to avoid drowsiness. EEG signals were acquired using the Enobio 8 system and ECG via a Polar H10 chest strap. Data were preprocessed through filtering, artifact rejection, and segmentation. EEG features related to spectral activity, functional connectivity, and signal complexity were extracted, along with heart rate variability (HRV)-related ECG parameters.

The experimental setup was supported by the Neuroelectrics Instrument Controller 2 (NIC2) for data acquisition and MATLAB for audio generation and signal analysis. After preprocessing, several feature selection techniques were explored,

and Recursive Feature Elimination (RFE) was selected to retain the most relevant features for each subject, reducing the total to 10%.

Among all participants, the most significant features were related to signal complexity (Higuchi Fractal Dimension, HFD) and brain synchronization (Phase Locking Value, PLV). Subsequently, a subject-specific Support Vector Machine (SVM) classifier was implemented to track prediction trends over time during both sessions.

The analysis revealed two diverging trends: an increasing trend for BBs recognition and a decreasing one for sham. However, the classification accuracy did not show significant deterioration, maintaining good overall recognition rates (Sham = 70.54% ± 8.00%, BBs = 68.75% ± 7.54%). Wilcoxon signed-rank tests showed no significant differences between the two sessions ($p \geq 0.05$).

In conclusion, the study demonstrated the presence of short-term effects induced by BBs stimulation, although it did not clearly distinguish between conditions across all sessions. Future studies could aim to determine the minimum duration of BBs stimulation required to produce a consistent and significant effect by modifying the experimental protocol. Additionally, increasing the sample size and employing a high-density EEG system would be necessary to reduce inter-subject variability and improve the overall quality of the analysis.

Acknowledgements

We would like to express our deepest gratitude to our supervisors, Prof. Luca Mesin and Prof. Matteo Raggi, for giving us the opportunity to work on this thesis and for their invaluable guidance throughout its development. Their insightful suggestions, continuous support, and constructive feedback greatly contributed to the quality of our work. Beyond the academic support, their mentorship has played a significant role in our professional and personal growth, and we are truly thankful for the experience of working under their supervision.
Riccardo and Leonardo.

"La perfezione non è il nostro obiettivo — è la nostra tendenza... Poi che una cosa non riesca perfetta c'è da aspettarselo, proprio perché tendiamo alla perfezione. L'importante è che ci sia stato impegno da parte nostra."
- YouTubo Anche Io

Table of Contents

List of Figures

Acronyms

AB	Alpha/Beta Power Ratio
AI	artificial intelligence
ApEn	Approximate Entropy
ASSR	auditory steady-state response
AT	Alpha/Theta Power Ratio
AV	atrioventricular
BB	binaural beat
BBs	Binaural Beats
CAR	common average referencing
CMI	cortical modulation index
CMRR	common-mode rejection ratio
CMS	Common Mode Sense
CNS	central nervous system
CPU	central processing unit
CVRR	Coefficient of Variation of RR intervals
DRL	Driven Right Leg
ECG	Electrocardiography
EEG	Electroencephalography
EMG	electromyogram
FFR	frequency-following response
HFD	Higuchi Fractal Dimension
HFOs	high-frequency oscillations
HR	Heart Rate
HRV	Heart Rate Variability

IAF	Individual Alpha Frequency
IFCN	International Federation of Clinical Neurophysiology
IVC	inferior vena cava
KFD	Katz Fractal Dimension
MEG	magnetoencephalography
ML	machine learning
MOC	medial olivocochlear
NIC2	Neuroelectrics Instrument Controller 2
OOB	Out-of-Bag
PE	Permutation Entropy
PLV	Phase-Locking Value
PFD	Petrosian Fractal Dimension
PNS	peripheral nervous system
PR	PR interval
PSD	Power Spectral Density
QRS	QRS complex
RBF	Radial Basis Function
RFE	Recursive Features Elimination
RMSSD	Root Mean Square of the Successive Differences
SA	sinoatrial
SDNN	Standard Deviation of NN intervals
SVC	superior vena cava
SVM	Support Vector Machine
VC	Vapnik–Chervonenkis

Chapter 1

Introduction

1.1 Nervous System

The nervous system monitors and responds to changes in the internal and external environment of the body. It controls perception, behavior, memory, and voluntary movements. Comprising all neural tissue, it transmits information throughout the body. The central nervous system (CNS), made up of the brain and spinal cord, handles integration and coordination. The peripheral nervous system (PNS) includes all neural tissue outside the CNS[1].

1.1.1 Anatomy and Physiology of the Brain

The brain is divided into two distinct hemispheres and four primary lobes: the parietal, frontal, temporal, and occipital lobes, each with specialized functions that contribute to various aspects of cognition, sensory processing, and motor control:

- **The frontal lobe** lies in front of the central sulcus and is divided into key areas: the prefrontal cortex, the premotor cortex and the primary motor cortex, which is essential for motor function. Damage in this area can impair motor tasks on the opposite side and affect expressive language (Broca's area), higher functions such as emotions, personality and decision-making. It also houses the brain's micturition center and the frontal eye fields, which control saccadic eye movements. Lesions in the frontal lobe can cause disinhibition, cognitive deficits, and regression to primitive reflexes, with eye movement changes depending on whether the cause is a lesion or a seizure[2].

- **The temporal lobe** processes sensory input for emotions, memory, and language comprehension. It houses the primary auditory cortex and Wernicke's area, responsible for language understanding, with lesions causing receptive

aphasia. The medial temporal lobe includes key structures like the hippocampus, where damage leads to anterograde amnesia, and is a common site for epilepsy, with seizures causing emotional changes, déjà vu, or olfactory hallucinations. Bilateral amygdala damage can result in Kluver-Bucy syndrome, characterized by disinhibited behaviors. Damage to the optic radiation in the temporal lobe may cause a "pie in the sky" visual defect, and posteromedial lesions can lead to achromatopsia[2].

- **The parietal lobe** integrates sensory input with the visual system and is involved in perception and sensation. The primary somatosensory cortex, located in the postcentral gyrus, processes contralateral sensory information. Damage to the dominant parietal lobe can cause Gerstmann's syndrome, with symptoms like agraphia, acalculia, finger agnosia, and left-right disorientation. Lesions in the non-dominant parietal lobe result in hemispatial neglect, leading to difficulties in self-care [2].

- **The occipital lobe** is the primary center for visual processing in humans. Its primary visual cortex, located in Brodmann Area 17 within the calcarine sulcus, is essential for vision. Damage to one occipital lobe may cause homonymous hemianopsia and visual hallucinations, while bilateral damage can lead to cortical blindness, marked by loss of sight with preserved light reflexes. Anton syndrome, a condition where patients deny their visual loss despite being blind, is associated with cortical blindness. Other effects of occipital damage include visual illusions, such as altered object size or abnormal coloration[2].

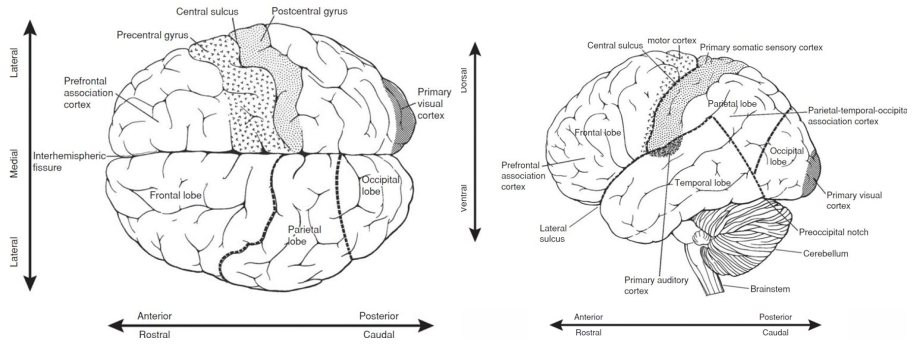

Figure 1.1: Cerebral Anatomy: **(a)** Dorsal view and **(b)** Lateral view. Adapted from[3].

1.1.2 Cerebral Cortex

The cerebral cortex is the outermost layer of the cerebrum, measuring approximately 1.5 to 4 mm in thickness. It consists of gray matter, which is the most functionally important layer as it contains neuronal cell bodies and unmyelinated axons responsible for processing information. Beneath it lies the white matter, composed primarily of myelinated axons that facilitate communication between different brain regions.

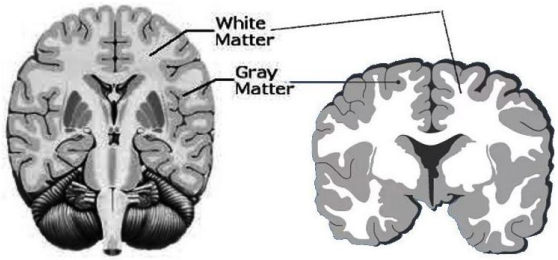

Figure 1.2: Gray matter and white matter. Adapted from[4].

In newborns, the cerebral cortex grows rapidly, adapting to the constraints of a small skull. Because the skull is not completely fixed at birth, the cortex develops a highly convoluted structure with gyri and sulci, maximising the surface area for cognitive and sensory processing. This unique convolution is essential to accommodate the large number of neurons required for the brain's complex functions[5].

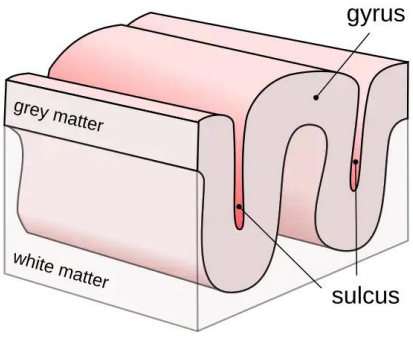

Figure 1.3: Illustration of gyri and sulci in the human brain. Adapted from[6].

1.1.3 Subcortical areas

The main subcortical areas of the brain that interact with the cortex and are intimately involved in motor and sensory functions include:

- **The brainstem** serves as a bridge connecting the cerebrum and cerebellum to the spinal cord. It houses key centers responsible for autonomic functions like breathing, heart rate, temperature regulation, digestion, and wake-sleep cycles. Composed of both white and gray matter, its white matter contains fiber tracts that relay voluntary motor signals from the cerebral cortex and somatosensory information from the spinal cord to the brain[7].

- **The cerebellum** coordinates voluntary movement and refines motor activity by processing sensory input from the brain and spinal cord. It also plays a role in cognitive functions like attention, language, pleasure response, and fear memory[8].

- **The thalamus**, a gray matter structure of the diencephalon, acts as a relay station between the brain and body, processing sensory and motor signals and regulating consciousness, sleep, and wakefulness. It consists of nuclei that handle sensory input, with specific nuclei dedicated to visual, auditory, and somatosensory information. The thalamus also connects to the limbic system, playing a role in memory and learning. While primarily gray matter, it contains white matter structures like the medullary laminae. The reticular nucleus modulates signals from other thalamic nuclei but does not project to the cortex. Advances in neuroimaging have improved the understanding and surgical accessibility of the thalamus[9].

- **The basal ganglia**, a cluster of subcortical nuclei, primarily regulate motor control and also influence cognition, reward, and emotion. Key structures include the striatum (caudate and putamen), globus pallidus, subthalamic nucleus, and substantia nigra. Motor control is managed through two opposing pathways: the direct pathway, which promotes movement, and the indirect pathway, which inhibits movement. Dopamine from the substantia nigra modulates these pathways by exciting the direct pathway (via D1 receptors) and inhibiting the indirect pathway (via D2 receptors). Dysfunction of the basal ganglia is linked to motor disorders such as Parkinson's and Huntington's diseases[10].

1.1.4 Neurons and Glial Cells

Neurons are the cells which are considered to be the core of nervous tissue. They are responsible for electrical signals that transmit information about sensations

and produce movements in response to these stimuli, as well as inducing thought processes within the brain. An important part of the function of neurons lies in their structure, or shape. The three-dimensional shape of these cells makes the immense number of connections within the nervous system possible.[11] Neurons consist of a cell body (soma) with a nucleus and organelles, along with specialized structures for communication. Dendrites receive signals from other neurons at synapses, while the axon hillock integrates these signals and propagates them through the axon to axon terminals, where chemicals transmit signals to other cells. Myelin, produced by glial cells, insulates axons to increase signal speed, with nodes of Ranvier "recharging" the signal along the way. Neurons rely on extensive networks of connections, with some, like Purkinje cells, receiving inputs from thousands of other neurons[12].

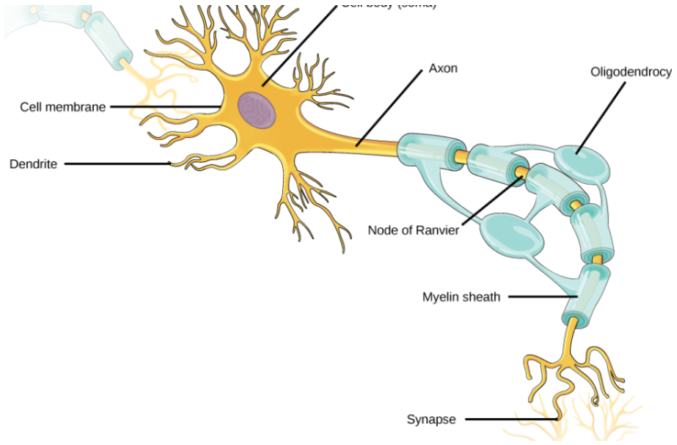

Figure 1.4: Neurons contain organelles common to many other cells, such as a nucleus and mitochondria. They also have more specialized structures, including dendrites and axons. Adapted from[12].

Glial cells, which outnumber neurons by tenfold, are essential for nervous system function. They guide developing neurons, buffer harmful ions and chemicals, and produce myelin sheaths to insulate axons and enhance signal speed. Glia also play active roles in responding to nerve activity and modulating communication between neurons. Without glial cells, neurons could not function properly. Their importance is further underscored by the fact that many brain tumors result from glial cell mutations. Neurons, meanwhile, rely on dendrites, axons, and synapses for communication, with extensive networks like Purkinje cells receiving thousands of inputs[11, 12].

1.1.5 Synapses

The human brain contains about 86 billion neurons that communicate through electrochemical signals at specialized junctions called synapses. A synapse consists of a presynaptic terminal, where an electrical signal (action potential) triggers neurotransmitter release, and a postsynaptic terminal containing receptors that bind these neurotransmitters. Synaptic connections can range from a few to hundreds of thousands per neuron[13].

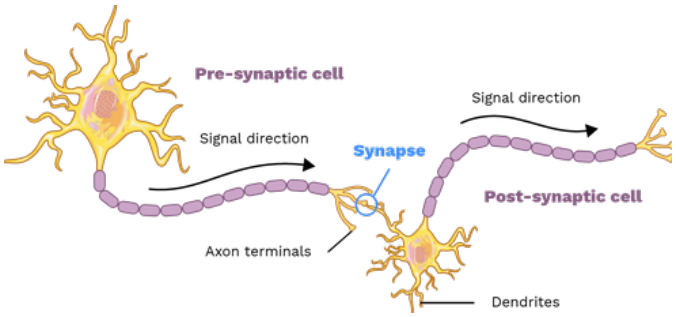

Figure 1.5: Signal transmission from the presynaptic neuron to the postsynaptic neuron. Adapted from[14]

Chemical synapses, the most common type in mammals, involve neurotransmitters crossing a synaptic cleft, with a delay of 0.5–1 ms. Synaptic types include axodendritic (usually excitatory), axosomatic (inhibitory), and axoaxonic (modulatory). In contrast, electrical synapses use gap junctions for direct current flow between neurons, enabling faster communication with minimal delay[13].

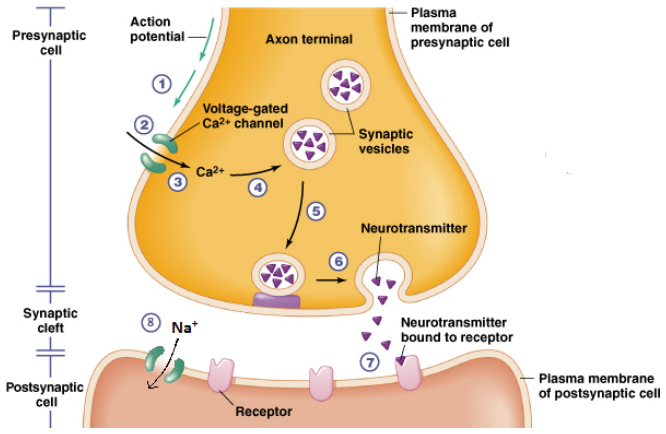

Figure 1.6: Synaptic transmission from presynaptic to postsynaptic neuron via neurotransmitter release and receptor activation. Adapted from[15].

Neurons rely on glial cells for development, growth guidance, and reuptake of excess neurotransmitters. Axons transport neurotransmitters to presynaptic terminals, while dendrites receive and integrate signals. During development, synapses form in a precise sequence, starting with large motor neurons, followed by sensory neurons and glial cells. This orchestrated process ensures accurate neuronal communication and network functionality in the central nervous system[13].

1.2 Electroencephalogram (EEG) signal

1.2.1 Background and Historical Development

An electroencephalogram (EEG) records the electrical potentials generated by cortical neurons through scalp electrodes. This methodology was first demonstrated by Richard Caton in 1875 and later applied to human subjects by Hans Berger in 1924[16]. Despite significant advancements in neuroimaging techniques, EEG continues to serve as the cornerstone paraclinical tool for seizure evaluation[16].

Modern digital EEG systems capture data from at least 128 channels at sampling rates above 10 kHz with 24-bit resolution and can detect synchronous discharges from cortical regions of roughly 10 cm^2.

Well-trained technicians and experienced clinical neurophysiologists are needed to collect and correctly interpret EEG signals.

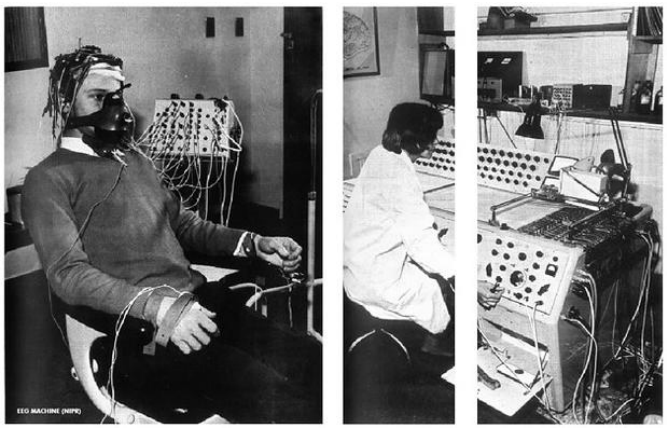

Figure 1.7: Hans Berger's first encephalograph. Adapted from[17].

1.2.2 Physiology of EEG Signals

As mentioned above, scalp electrodes detect the summated dipolar fields produced by synchronized excitatory and inhibitory postsynaptic potentials in cortical pyramidal cells. These signals arise from ionic currents flowing in the extracellular space

of dendritic membranes in cortical layers III to V, where pyramidal neurons are densely packed. Since cell membranes act as electrical insulators, only extracellular currents pass through the brain tissue and skull to the scalp electrodes, unfortunately intracellular currents remain inaccessible. The biophysical phenomenon that allows propagation of these local field potentials is known as volume conduction.

Excitatory postsynaptic potentials, driven by sodium influx into distal dendrites, generate a local extracellular negativity at the synapse (an active sink) and a compensating positivity at a distance (a passive source). Inhibitory postsynaptic potentials produce the opposite pattern, with chloride influx creating extracellular positivity at the synapse (active source) and negativity at the passive sink.

The anatomical arrangement of pyramidal neurons in palisades, with apical dendrites aligned perpendicular to the cortical surface, enables coherent dipole formation across large neuronal populations. When tens of square centimeters of cortex are synchronously activated, these individual dipoles summate into electrical currents detectable by scalp electrodes. In contrast, action potentials are brief, spatially discrete, and largely asynchronous, contributing minimally to surface EEG recordings. The requirement for widespread, synchronized activity and the smearing effect of volume conduction impose limits on EEG's spatial resolution.

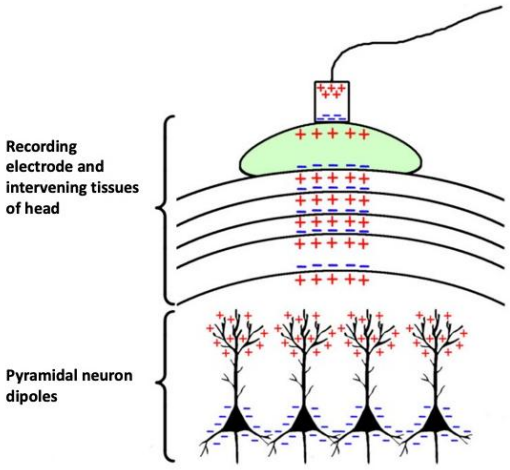

Figure 1.8: Representation of the electric dipole formed by pyramidal neurons through the scalp. Adapted from[18].

The resulting dipole orientation and cortical location shape the scalp potential topography, which can be visualized through voltage or amplitude maps.

In a relaxed, awake state, the dominant EEG rhythm is the 7–13 Hz posterior alpha rhythm, a product of oscillatory interactions between cortex and thalamus. Engaging in mental tasks desynchronizes this alpha activity, producing lower-amplitude, higher-frequency beta waves in the 13–30 Hz range. During sleep and under encephalopathic conditions, slower theta waves (4–7 Hz) and delta waves ($<$ 4 Hz) predominate, as will be explained later in subsection 1.2.5.

In the process of development, EEG patterns evolve from discontinuous neonatal rhythms to continuous adult-like rhythms detected at about eight years of age. The primary neuronal sources of these rhythmic waveforms reside in cortical layers III and V, where pyramidal cell bodies and the extensive dendritic tree generate dipolar fields.

Together, the interplay of synaptic anatomy, neuronal synchronization, and volume conduction underlies the rich tapestry of EEG signals recorded at the scalp. Understanding these anatomical and physiological principles is essential for interpreting EEG patterns in both clinical and research settings[19].

1.2.3 Overview of Non-Invasive Scalp EEG Electrodes

Scalp EEG electrodes serve as the non-invasive interface between the patient and the recording system[16]. Each electrode consists of a cup-shaped disc made of inert metal (commonly silver/silver-chloride or gold) filled with electrolytic paste, ensuring stable ion exchange and a consistent electrode potential[19]. When voltage is applied at the metal–paste interface, current flows according to Ohm's law ($V = I \cdot R$), while in alternating-current circuits impedance (Z) replaces resistance ($V = I \cdot Z$).[19]

To minimize thermal noise and avoid salt-bridge artifacts, electrode impedances should be maintained between approximately 100 Ω and 10 kΩ through meticulous skin preparation and the use of a high-sodium-concentration conductive paste[19].

Electrode placement follows the International 10–20 system as extended by the IFCN, relying on cranial landmarks (nasion, inion, pre-auricular points) and spacing electrodes at 10% or 20% intervals of the measured distances between them[19]. Each site is labeled with a letter denoting the underlying brain region (e.g., Fp for frontal-polar, T for temporal) and a number (or "z") for midline electrodes; odd numbers indicate left-hemisphere sites, even numbers right, and higher numbers more lateral locations. The addition of the inferior temporal chain beyond the classic array extends coverage to basal temporal regions, thereby improving diagnostic yield and localization accuracy of epileptic discharges[19]. For

studies requiring greater source-localization precision, high-density configurations with 5% spacing can be used, though these are less practical for routine or long-term monitoring.

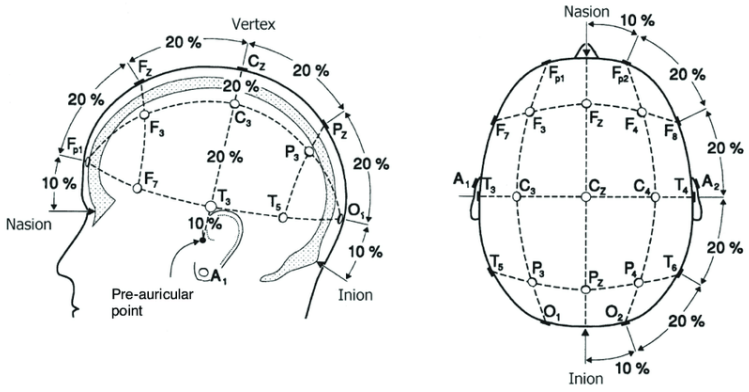

Figure 1.9: 10-20 EEG system. Adapted from[20].

Modern EEG amplifiers feature high input impedances that tolerate electrode impedances up to 10 kΩ without compromising signal fidelity, provided that electrode contact remains stable. Semi-invasive sphenoidal electrodes—stainless-steel, silver, or platinum wires inserted lateral to the foramen ovale via the zygomatic arch—allow deeper temporal recordings but at the expense of increased patient discomfort and procedural risk[19]. Finally, ground and reference electrodes, together with auxiliary ECG, EMG, and respiratory channels, are essential for identifying and removing physiological artifacts, and impedances should be checked immediately after application, at the start and end of recording, and whenever stability is in doubt.

1.2.4 EEG acquisition methods

EEG signals can be acquired using various montages and referencing strategies, which influence the quality, interpretability, and spatial resolution of the recorded data. The main acquisition configurations include monopolar (referential), bipolar, and common average referencing, each with specific technical and physiological implications.

In a **monopolar** (or referential) configuration, each electrode records the potential difference between a scalp location and a common reference electrode, which is typically placed on an electrically neutral site such as the mastoid, earlobe, or the vertex (Cz)[21]. This method provides high signal amplitude and is widely used in

clinical applications, although it can be susceptible to reference contamination and common-mode artifacts.

The **bipolar** montage involves calculating the potential difference between two adjacent scalp electrodes. This approach improves the location of cortical activity and reduces common noise, as artifacts common to both electrodes tend to cancel each other out. Bipolar recordings are particularly useful for detecting localised discharges[22].

A more refined technique is **differential acquisition**, where signals are measured between a pair of electrodes, often processed with high common-mode rejection ratio (CMRR) amplifiers. This configuration improves signal quality by reducing ambient noise and is commonly used in research-grade EEG systems and dry electrode setups[23].

Other methods include **common average referencing** (CAR), where the average of all electrode signals is used as a dynamic reference. This strategy can mitigate reference bias and is beneficial in dense-array EEG recordings[24].

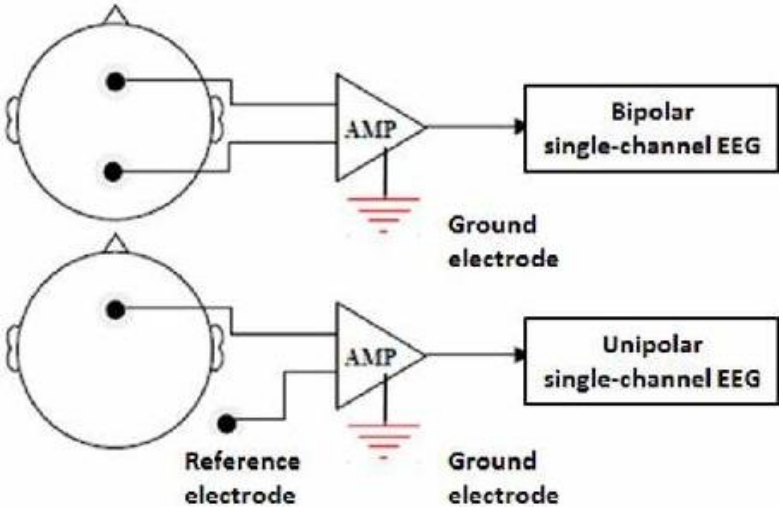

Figure 1.10: Differences between bipolar and unipolar eeg acquisition. Adapted from[25].

Modern EEG caps (electrode caps) often support flexible referencing configurations through integrated active or passive electrodes, enabling high spatial resolution and adaptability for specific experimental paradigms. Understanding the implications of each acquisition method is critical for optimizing data quality and ensuring the reliability of EEG-based analyses.

1.2.5 Brain Rhythms

EEG signals consist of distinct frequency bands, each associated with different brain states. The primary EEG rhythms include:

- **Delta** (0.5–4 Hz) : Predominant in deep sleep, especially in the frontocentral regions. Pathological delta waves in awake states indicate encephalopathy or focal cerebral dysfunction[26].

- **Theta** (4–7 Hz) : Common in drowsiness and early sleep stages (N1, N2), originating in the frontocentral regions. It shifts posteriorly with increasing drowsiness. Emotional states can enhance theta activity in young individuals, while focal theta in awake states suggests cerebral dysfunction[26].

- **Alpha** (7–13 Hz) : The dominant rhythm in awake adults, seen in the occipital regions with eyes closed. It disappears with eye opening or mental effort. Slowing of alpha indicates cerebral dysfunction. Mu rhythm, a central variant, attenuates with motor activity but not eye opening[26].

- **Beta** (13–30 Hz) : Most prominent in the frontal and central regions, increasing with drowsiness and sedative use. It is typically low in amplitude but can be suppressed by cortical injury or fluid collections[26].

- **High-Frequency Oscillations (HFOs)** (>30 Hz) : Includes gamma (30–80 Hz), ripples (80–200 Hz), and fast ripples (200–500 Hz). Gamma rhythms aid sensory integration, while HFOs are linked to epileptic activity, with fast ripples indicating epileptogenic regions[26].

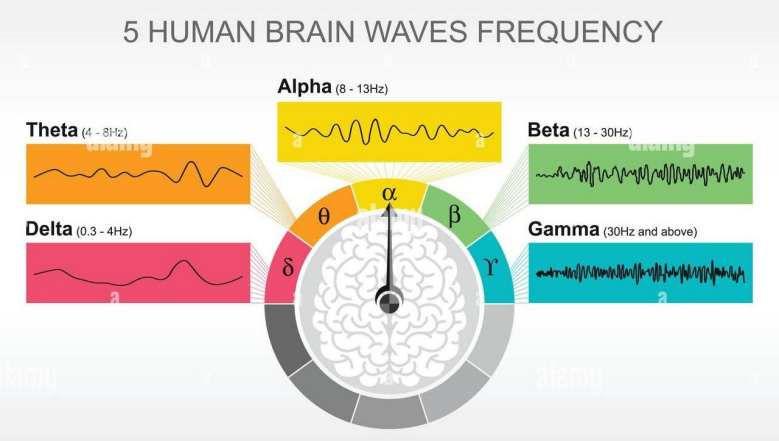

Figure 1.11: Quadrant diagram depicting the five principal brain rhythms—delta (0.5–4 Hz), theta (4–8 Hz), alpha (8–13 Hz), beta (13–30 Hz), and gamma (30–100 Hz)—along with their frequency bands and associated cognitive functions. Adapted from[27].

1.3 Cardiovascular System

The cardiovascular system is a closed circulatory network comprising the heart, blood, and vessels, responsible for transporting oxygen, nutrients, hormones, and waste products throughout the body[28]. The heart functions as a dual pump: the right side drives deoxygenated blood through the pulmonary circuit, while the left side propels oxygenated blood into the systemic circulation[29]. Arteries and arterioles conduct blood under high pressure, while capillaries facilitate exchange with tissues, and veins return blood under low pressure[30]. Cardiac output, determined by stroke volume and heart rate, adapts dynamically to metabolic demands[31]. Neurohormonal control mechanisms, including autonomic inputs and endocrine signals, ensure homeostatic regulation of blood pressure and tissue perfusion[30]. Efficient cardiovascular function is critical for maintaining internal balance and supporting cellular metabolism[29].

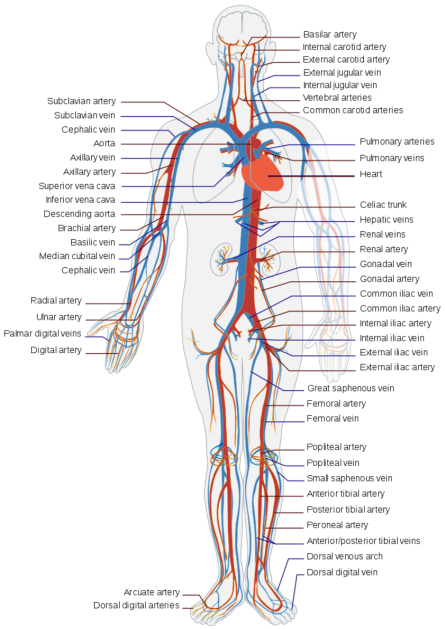

Figure 1.12: Cardiovascular system. Adapted from[32].

1.3.1 Anatomy of the Heart

The heart is a midline, cone-shaped muscular pump about the size of a fist, weighing roughly 300 g and nestled in the middle mediastinum, with its base formed mainly by the left atrium and its diaphragmatic surface resting on the central tendon of the diaphragm[33]. Its fibrous pericardium, continuous with the great vessels and diaphragm, envelops two serous layers whose reflections create the transverse and oblique pericardial sinuses[33]. Internally, an obliquely oriented interventricular septum bulges rightward—owing to the left ventricle's thicker wall—and divides the right ventricular chamber (characterized by trabeculae carneae, pectinate muscles, and the moderator band) from the left ventricle (noted for its robust trabeculae and aortic vestibule)[33]. The right atrium, receiving the superior vena cava (SVC) and inferior vena cava (IVC) and housing the fossa ovalis and crista terminalis, conducts blood through the tricuspid valve into the right ventricle, which outflows via the pulmonary valve into the pulmonary trunk[33]. The left atrium, forming the heart's base, receives four pulmonary veins into its smooth chamber and channels blood through the mitral valve into the high-pressure left ventricle, which then ejects through the aortic valve into the ascending aorta[33]. A figure-of-eight fibrous skeleton anchors all four valves and electrically isolates atria from ventricles, ensuring coordinated contractions[33]. Impulses originate at the sinoatrial node in the right atrium, pass to the AV node at the septal tricuspid cusp, then travel via the His–Purkinje system to elicit ventricular contraction, all finely tuned by

sympathetic and parasympathetic innervation[33]. Finally, the coronary arteries arise from the aortic sinuses—right and left—supplying myocardium whose venous return drains via the great, middle, and small cardiac veins into the coronary sinus, with additional drainage through Thebesian veins directly into the chambers[33].

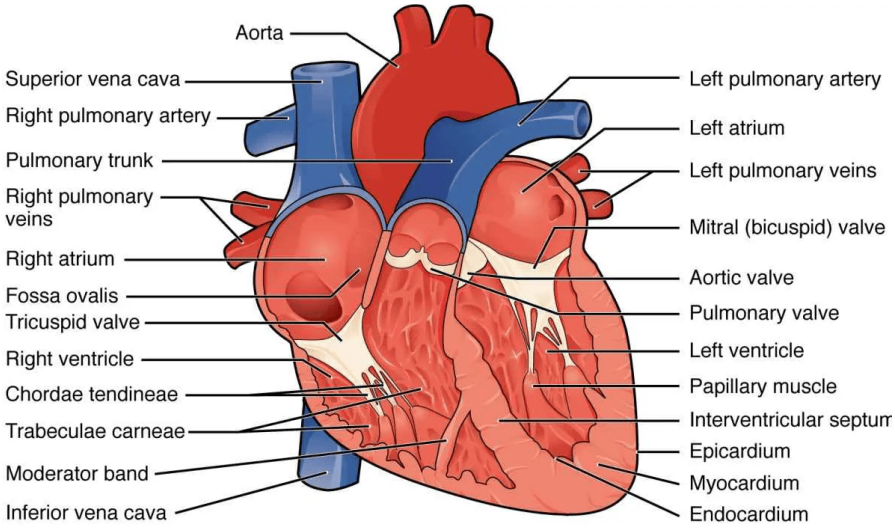

Figure 1.13: Heart Cross-section (frontal view). Adapted from[34].

1.3.2 Physiology of the Heart

The cardiovascular system hinges on the heart's role as a dual pump: its chambers generate the pressure necessary to propel blood through both pulmonary and systemic circuits, and they adjust stroke volume to match venous return via the Frank–Starling mechanism. Within this closed loop, arterial and venous networks distribute blood to every tissue, with total peripheral resistance determined by vessel diameter and blood viscosity[35]. Under resting conditions, venous return largely governs cardiac output, but during intense activity or in disease states, the heart's intrinsic contractile capacity can become the limiting factor. Exchange across capillary beds ensures that oxygen and nutrients reach cells while metabolic byproducts are removed, driven by the balance of hydrostatic and oncotic pressures[35]. Short-term regulation of arterial pressure depends on the interplay between cardiac output, peripheral resistance, and rapid baroreceptor reflexes, whereas long-term pressure homeostasis is achieved through renal control of fluid volume and the renin–angiotensin–aldosterone axis[35].

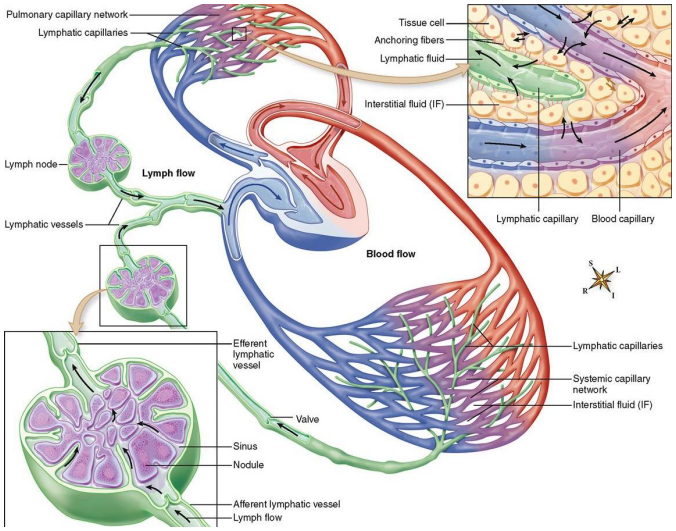

Figure 1.14: Capillary and lymphatic exchange. Adapted from[36].

Locally, tissues fine-tune blood flow to match metabolic demand via functional hyperemia and autoregulation, safeguarding oxygen delivery even when systemic pressures fluctuate. The coronary circulation exemplifies this, employing robust autoregulatory mechanisms and collateral vessels to maintain perfusion despite changing loads. Endothelial and smooth muscle cells integrate mechanical forces (such as shear stress) and chemical signals (including nitric oxide and metabolic autacoids) to modulate vascular tone. Autonomic innervation further refines cardiovascular responses: sympathetic and parasympathetic pathways swiftly adjust heart rate and vessel diameter to meet moment-to-moment demands[35]. Blood composition—hematocrit and plasma protein levels—affects viscosity and oncotic pressures, thereby influencing cardiac workload and capillary filtration[35]. In parallel, cardio-renal feedback loops link changes in arterial pressure and flow to renal salt and water excretion, closing the integrative control circuit[35]. The lymphatic system complements these processes by returning interstitial fluid to the bloodstream, preventing edema and maintaining fluid balance[35]. Finally, chronic stimuli such as regular exercise or sustained hypertension drive structural remodeling of the heart and vessels, enabling the system to adapt to altered hemodynamic demands over time[35].

1.4 Electroencephalographic (ECG) signal

The electrocardiogram (ECG or EKG) is a non-invasive recording of the heart's electrical activity obtained through electrodes affixed to the skin[37]. First described by Willem Einthoven in 1902, it quickly became indispensable for diagnosing and

monitoring cardiovascular disorders[37].

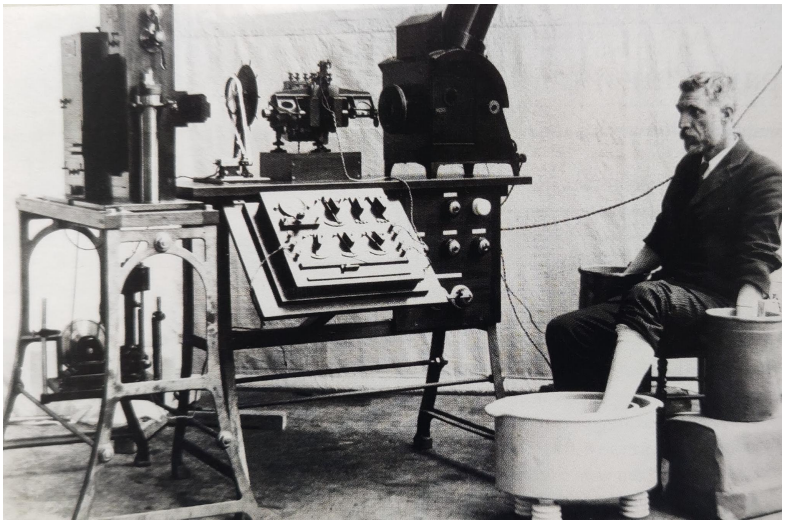

Figure 1.15: Einthoven's first ECG machine. Adapted from[38].

A standard 12-lead ECG employs six limb leads (I, II, III, aVR, aVL, aVF) and six precordial leads (V1–V6) to capture electrical vectors in both frontal and horizontal planes[37]. During normal sinus rhythm, impulses originate at the sinoatrial (SA) node and propagate through the atria, generating the P wave[37]. A brief delay at the atrioventricular (AV) node produces the PR interval on the tracing. Rapid, synchronous depolarization of the ventricles yields the QRS complex, which reflects coordinated contraction. Ventricular repolarization follows as the T wave, completing the main waveform sequence. Proper skin preparation—cleaning, shaving, and application of conductive gel—minimizes artifacts and ensures high-fidelity tracings[37].

Accurate electrode placement is critical for reliable regional assessment of myocardial electrical activity.

Modern ECG machines convert the analog cardiac signal into digital form using front-end analog-to-digital converters, typically sampling at rates ranging from 1,000 to 15,000 Hz. These high sampling rates are essential for preserving the fine temporal structure of the electrocardiogram and enhancing the detection of pacemaker spikes as well as high-frequency components within the QRS complex[40]. Signal fidelity is further maintained through digital filtering techniques: low-frequency filtering with a cutoff at 0.05 Hz, implemented via zero-phase digital filters, effectively reduces baseline wander without compromising the integrity of the ST segment, while high-frequency filtering—using cutoffs of at least 150 Hz in adults and up to 250 Hz in infants—allows accurate representation of the rapid

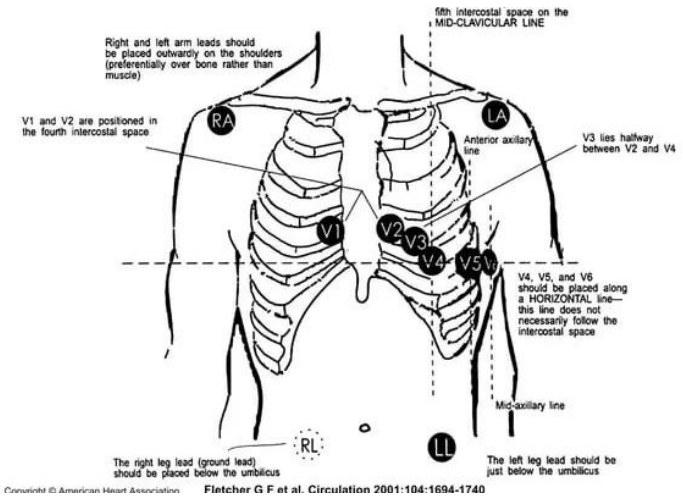

Figure 1.16: 12-leads ECG placement. Adapted from[39].

upstroke velocities and subtle notches that are often clinically relevant.

To minimize beat-to-beat variability and background noise, digital electrocardiographs construct representative average or median complexes for each lead. This template-based approach facilitates more stable measurements, especially when combined with time-coherent, simultaneous acquisition across all twelve leads, which allows for global determination of intervals by identifying the earliest onset and latest offset of any waveform in any lead[40]. Automated algorithms then process these templates to derive key diagnostic parameters such as the P-wave duration, PR interval, QRS duration, and QT interval, supporting diagnostic classification workflows. However, despite the sophistication of digital analysis, the involvement of a trained clinician remains essential to interpret subtle abnormalities and to distinguish pathological signals from artifacts that automated systems might overlook.

The interpretative process typically follows a structured approach, beginning with an evaluation of heart rate, rhythm, and electrical axis, and proceeding to detailed analysis of waveform morphology and interval durations.

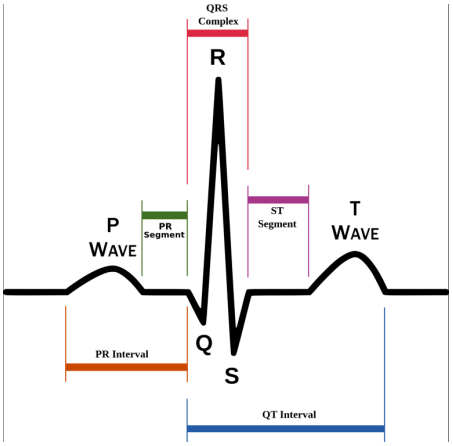

Figure 1.17: Normal ECG signal with his different features. Adapted from[41].

Beyond the confines of the clinic, continuous ECG monitoring is increasingly performed through telemetry systems, Holter monitors, and wearable devices, which extend the temporal window for arrhythmia detection and support long-term management strategies[37]. To facilitate storage and transmission, digital compression techniques are routinely applied, generally without significant degradation of diagnostic fidelity.

As technology advances, standards for template fidelity and interval measurement algorithms continue to evolve, with promising developments on the horizon including adaptive filtering and machine learning–based interpretation systems. However, in the context of these innovations, the fundamental principles of electrocardiography remain unchanged: thorough understanding of the origin of the waveform, accurate identification of morphological features, and a methodical approach to interpretation are still the cornerstones of ECG analysis.

1.5 Reconstructing Sound in the Auditory Pathway

Sound waves enter the outer and middle ear, where the ossicles amplify vibrations and transmit them into the fluid of the cochlea. Within the cochlea, pressure waves travel along the basilar membrane, bending hair-cell stereocilia against the tectorial membrane and opening potassium channels to convert mechanical energy into receptor potentials. Spiral ganglion neurons bundle into the auditory nerve, carrying frequency-specific and intensity-dependent signals first to the cochlear nuclei, which preserve the tonotopic map. From there, fibers ascend to the superior olivary complex, where interaural time and level differences are computed for spatial

localization. The lateral lemniscus and inferior colliculus integrate these binaural cues and begin scene analysis by segregating overlapping sound sources. The medial geniculate nucleus of the thalamus relays and refines auditory patterns before they reach the primary auditory cortex. In cortex, tonotopic organization persists, with clusters of neurons tuned to similar frequencies reconstructing complex features such as speech envelopes and phonemes. Higher-order auditory areas then extract speaker identity and other salient sound characteristics through distributed neural networks. Finally, descending pathways from the auditory cortex dynamically modulate hair-cell responsiveness and brainstem processing to adapt reconstruction based on attention and context[42].

Moreover, the medial olivocochlear (MOC) efferent system exerts a feedback control on outer hair cell electromotility, improving signal detection in noise and protecting the cochlea from acoustic overstimulation[43]. Corticofugal fibers originating in layer V of the primary auditory cortex project to both the superior olivary complex and the cochlear nucleus, mediating rapid plasticity and sharpening frequency tuning at peripheral and brainstem levels[44]. These descending pathways operate on multiple timescales, from fast oscillatory modulation in the delta–theta bands linked to attentional shifts to longer-term synaptic changes underlying auditory learning and memory[44]. In cortex, belt and parabelt regions are organized into parallel ventral and dorsal streams: the ventral stream analyzes sound identity and phonemic structure, while the dorsal stream integrates auditory with sensorimotor information for spatial and sequence processing[45]. Moreover, corticothalamic projections to the medial geniculate nucleus form recurrent loops that refine temporal precision and context-dependent gating of incoming signals[46].

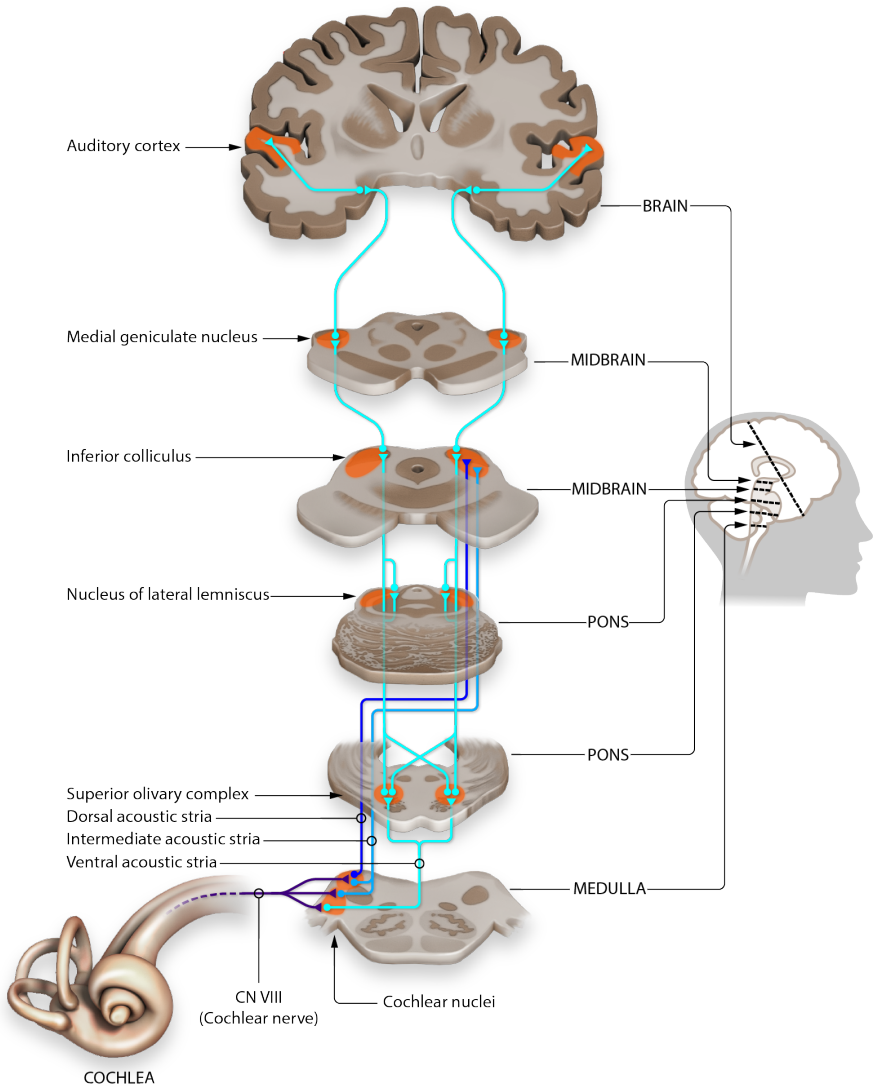

Figure 1.18: From the ear to the cerebral cortex. Adapted from[47].

Chapter 2

Binaural Beats

2.1 Understanding Binaural Beats: Fundamentals and Mechanisms

Combining two pure tones that differ slightly in frequency produces amplitude fluctuations at a rate equal to their frequency difference. If both tones reach the same ear, these physical intensity modulations are heard as acoustic beats. Presenting two tones with a slight frequency mismatch to each ear separately creates a perception of a third tone—a binaural beat—that oscillates at the absolute difference between the tones[48]. However, when one steady-frequency tone is delivered to each ear, listeners still perceive beats—even though there are no intensity changes at the ears themselves[49]. These "binaural beats" arise in the brain, where neural signals from the two ears converge in central auditory pathways, with origins thought to lie subcortically in the medial nucleus of the superior olivary complex[50]. Oster (1973) showed that, within the medial superior olive, each cycle of the presynaptic signal evokes a synchronized spike potential ("microphone theory"), whereas groups of fibers discharge in volley at higher frequencies ("volley theory"), thus enabling phase information to be conveyed up to 1 kHz despite the limits of neural phase-locking[51]. The perceived modulation depth of binaural beats is very low (approximately 3 dB), well below the intensity variations required for monaural beats, and this value establishes the minimum detection threshold for binaural beats in the brain[51]. Furthermore, adding white noise enhances the sensation of beats via a stochastic resonance mechanism, whereby random noise reinforces subthreshold phase fluctuations without altering the physical intensity of the sound[51]. Finally, studies using evoked potentials reveal significant differences in waveform amplitude and latency between monaural and binaural beats, confirming two distinct processing pathways within central auditory pathways[51]. Binaural beats can entrain cortical activity at both the specific frequency of the beat[49] and

cross-frequency modulations, such as theta beats driving interhemispheric alpha synchronization[52]. They also seem to modulate mood[53], pain perception[54], and cognitive performance in memory tasks[55].

In addition, these percepts align with canonical EEG rhythms—Delta (0.5–4 Hz), Theta (4–7 Hz), Alpha (7–13 Hz), Beta (13–30 Hz) and Gamma (>30 Hz)—each associated with different cognitive states such as deep sleep, meditation, relaxation, and active consciousness. Acoustically, binaural beats can be framed as the sensation of a moving sound source generated by an interaural phase difference: two ear-specific signals

$$s_l(t) = \sin\Big(2\pi f_1 t\Big), \tag{2.1}$$

$$s_r(t) = \sin\Big(2\pi f_2 t\Big), \tag{2.2}$$

are equivalent to a single carrier at

$$f_{\text{carrier}} = \frac{f_1 + f_2}{2} \tag{2.3}$$

with amplitude normalization at

$$f_{\text{mod}} = \frac{|f_2 - f_1|}{2} \tag{2.4}$$

because

$$s_r(t) = \sin\Big(2\pi f_1 t + \Phi(t)\Big), \qquad \Phi(t) = 2\pi(f_2 - f_1)\, t \tag{2.5}$$

This linear phase shift implements an interaural time-difference cue that listeners interpret as lateralized motion. Perception is optimal for carrier frequencies below 1.5 kHz(ideally <1 kHz[56]) and modulations under 35–40 Hz, beyond which beats are poorly resolved[57].

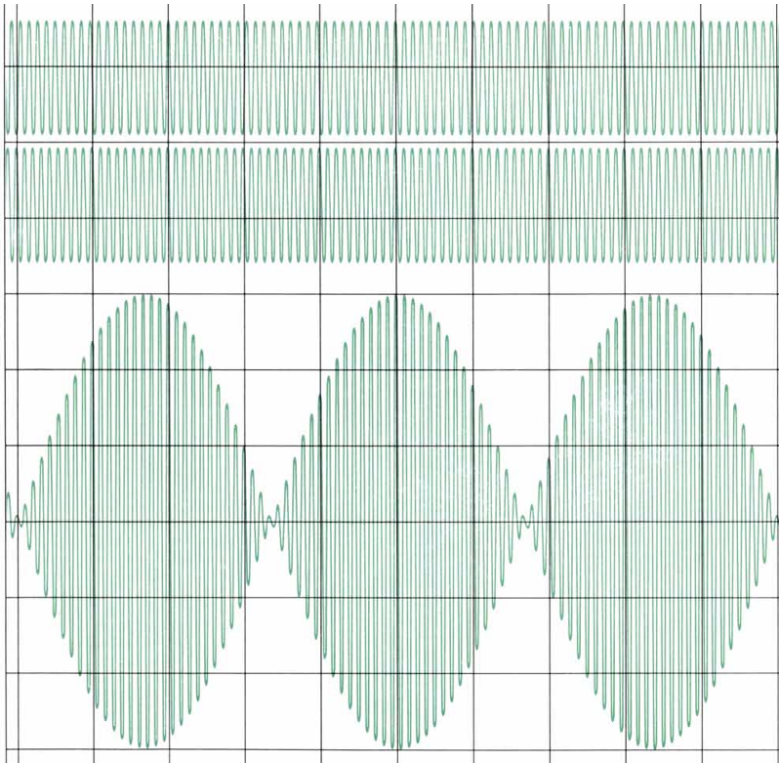

Figure 2.1: This diagram(adapted from[51]) illustrates binaural beats:
Top: two pure sine waves at slightly different frequencies (f_1 and f_2), same amplitude but out of phase.
Bottom: their sum—a carrier at the average frequency whose amplitude is modulated by a slow "beat" at $|f_2 - f_1|$.

2.2 The Brainwave Entrainment via Binaural Beats

The brainwave entrainment hypothesis proposes that rhythmic auditory or visual stimulation at a given frequency can induce the brain's electrical activity to oscillate in time with that external rhythm or its harmonics[58]. Early support came from studies showing time-locked auditory steady-state responses (ASSRs) and frequency-following responses (FFRs) during binaural-beat presentation [59, 60].

What makes entrainment via binaural beats especially attractive is the well-established mapping between EEG frequency bands—Delta (0.5–4 Hz), Theta (4–7 Hz), Alpha (7–13 Hz), Beta (13–30 Hz), Gamma (>30 Hz)—and distinct physiological and psychological states, from deep sleep and meditation to active concentration and arousal[61]. Consequently, researchers have tested whether delivering binaural

beats at target frequencies can induce corresponding changes in cognition, emotion, and autonomic function: effects on working memory, attention, mood regulation, pain perception, relaxation, mind wandering, creativity, and hypnotic susceptibility have all been reported[61].

2.3 Binaural Beats in Research: A State-of-the-Art Review

Several studies have investigated the neurophysiological and psychological effects of binaural beats (BBs), yet the results are highly variable depending on many factors such as frequency range, protocol, and measures used. Some experiments reported promising results in terms of brain entrainment and emotional modulation, while others failed to find significant effects, highlighting inconsistencies that merit further examination. Indeed, a substantial number of foundational experiments failed to observe significant shifts in EEG spectral power, phase coherence, or event-related potentials in response to binaural-beat stimulation—raising doubts about true entrainment[62, 63, 64]. Furthermore, stimulation parameters vary dramatically across studies—in carrier frequency, beat rate, tone duration, and presentation mode (continuous versus pulsed, focused listening versus distraction)—and control conditions range from pure tones and monaural beats to pink noise, silence or single-tone carrier[65, 66]. Despite these methodological challenges, recent neuroscientific work continues to explore this phenomenon, emphasizing the need for standardized stimulation protocols and empirical validation of entrainment within each study.

Many studies aimed to examine if BBs can entrain cortical oscillations and induce measurable changes in EEG or behavioral markers. For example, research using low-frequency BBs (4–7 Hz) generally reported more consistent effects than those using higher frequencies. Shamsi et al. showed that exposure to 7 Hz theta BBs resulted in a decrease in EEG complexity and increased theta power, suggesting reliable cortical entrainment, especially when analyzed using Higuchi fractal dimension[67]. One MEG study, instead, found that slow BBs at 4 and 6.66 Hz caused auditory steady-state responses localized primarily to auditory and parietal cortices, indicating successful entrainment[68].

Conversely, protocols that make use of BBs in the alpha or beta ranges (10–20 Hz) showed more ambiguous results. For instance, Kasprzak et al.[69] demonstrated that exposure to 10 Hz alpha-range binaural beats elicited a narrow EEG spectral peak precisely at the stimulus frequency in 4 out of 18 subjects, providing evidence of cortical entrainment. However, this effect was accompanied by a significant overall reduction in alpha-band (8–12 Hz) spectral power, suggesting

that entrainment at this frequency might coexist with general alpha suppression. Solcà et al.[52]further observed that 10 Hz binaural beats significantly enhanced interhemispheric coherence specifically within the alpha band (9–11 Hz) between auditory cortices, an effect interpreted as binaural integration rather than direct entrainment, as it occurred without corresponding amplitude changes or behavioral effects. Consistent with this, Ioannou et al.[70] showed that alpha-band (9–12 Hz) binaural beats elicited robust steady-state responses in the EEG alpha band and significantly modulated cortical connectivity patterns, enhancing global synchronization (PLV) but reducing direct cortico-cortical connectivity (PLI), specifically in musicians. In contrast, a study designed to evoke alpha (10 Hz) and beta (20 Hz) entrainment found no reliable frequency-following response in EEG signals, suggesting that continuous moderate-intensity tones may be insufficient for driving oscillatory activity in these bands[71]. This aligns with the findings of a personalized BB study, which tailored theta and beta frequencies based on heart rate, but failed to produce frequency-specific changes in EEG power, instead showing generalized modulations predominantly in auditory areas[72].

Some studies incorporated behavioral or physiological measures in addition to EEG. In one EEG-fMRI experiment, alpha BBs overlaid on vehicle noise produced mood alterations and alpha-band entrainment, offering multimodal evidence for BB-induced changes. Similarly, a case report using inaudible BBs embedded in brown noise and ambient music found EEG relaxation effects and improved peripheral physiology in all participants, reinforcing the utility of BBs for emotional regulation [73].

However, not all BB protocols produced successful results. A study using gamma (40 Hz) BBs didn't yield changes in attention or anxiety as measured by the Attention Network Test, suggesting that high-frequency BBs may not influence cognitive performance in this context. Similarly, to assess cortical responses to BBs in the alpha and beta band, no consistent entrainment was found across participants, and in some cases, exposure to BBs led to opposite effects such as alpha desynchronization. On the other hand, targeted applications of theta BBs showed more promise in modifying cognitive characteristics. For instance, theta BBs increased anterior theta activity and enhanced hypnotic susceptibility in low- and medium-susceptible individuals, underscoring the interaction between baseline traits and BB efficacy[74].

In terms of methodology, the diversity in EEG analysis techniques (power spectral density, phase-locking value PLV and fractal dimension) also plays a role in the observed variability. While spectral analyses often failed to detect entrainment, more subtle measures such as connectivity (PLV/CMI) and EEG complexity showed

BB-related effects even in the absence of clear spectral peaks[75].

In conclusion, the current state of the art suggests that theta and delta BBs are more likely to produce robust and replicable changes in brain dynamics, especially when combined with sensitive analysis methods or with behavioral tasks. In contrast, higher-frequency BBs (alpha, beta, gamma) show ambiguous outcomes, often failing to entrain the brain unless protocol parameters (e.g., carrier frequency, duration, intensity) are optimised. Further experiments are needed to establish the conditions under which BBs can be reliably used for cognitive and emotional modulation.

Chapter 3

Machine Learning

Machine Learning (ML) is a subfield of artificial intelligence that focuses on the design and study of algorithms capable of learning from data and improving performance on a given task through experience. As defined by Tom Mitchell (1997), "A computer program is said to learn from experience E with respect to some class of tasks T and performance measure P, if its performance at tasks in T, as measured by P, improves with experience"[76].

In practice, machine learning involves the construction of mathematical models capable of making predictions, classifications or pattern recognition on the basis of complex and often high-dimensional data. Unlike traditional programming, where rules are explicitly encoded by a human, machine learning systems automatically deduce patterns and decision logic from observed data[77].

Machine learning algorithms are typically classified into supervised learning and unsupervised learning, depending on the type of data and feedback available during training. In supervised learning, the algorithm is trained on labeled data, where both the input and the corresponding output are defined. The goal is to learn a mapping function that can generalise well to unseen data. Common supervised methods include linear regression, support vector machines, decision trees, and neural networks[78].

In contrast, unsupervised learning deals with unlabeled data. The algorithm attempts to uncover hidden patterns or intrinsic structures in the data without explicit guidance. This includes tasks such as clustering (e.g., k-means) and dimensionality reduction (e.g., principal component analysis), which are widely used for data exploration, visualization, and preprocessing[79].

3.1 Random Forest

Random Forests are a supervised learning method introduced by Leo Breiman[80] in 2001. The core idea is to construct an ensemble of decision trees, denoted by $\{h(x, \theta_k)\}$, where each tree is trained using a random vector θ_k drawn independently from the same distribution. For classification tasks, each tree casts a vote, and the forest outputs the class receiving the majority of votes. In regression, the output is the average of the predictions of the trees.

Formally, a random forest is a collection of classifiers $\{h(x, \theta_k)\}_{k=1}^{K}$, with the θ_k acting as sources of randomness, such as sampling the training set (bagging) or selecting a random subset of features at each split. These mechanisms guarantee that individual trees are different from each other, which is crucial to reduce overfitting and improving generalization.

To assess how confident the forest is in its predictions, Breiman introduces the concept of the **margin function**, defined as:

$$\mathrm{mg}(X, Y) = \mathbb{E}_k \left[I(h_k(X) = Y) \right] - \max_{j \neq Y} \mathbb{E}_k \left[I(h_k(X) = j) \right], \tag{3.1}$$

where $I(\cdot)$ is the indicator function, X is an input vector, and Y is its true class label. The margin measures how often the correct class is predicted compared to any other class. A higher margin results in a higher confidence and a lower chance of misclassification.

Using this, the **generalization error** of the forest is defined as the probability that the margin is negative:

$$PE^* = \mathbb{P}_{X,Y}(\mathrm{mg}(X, Y) < 0). \tag{3.2}$$

An important theoretical result is that, under the Strong Law of Large Numbers, the generalization error of a random forest converges almost surely as the number of trees increases:

$$PE^* \to \mathbb{P}_{X,Y} \left(\mathbb{P}_\theta(h(X, \theta) = Y) - \max_{j \neq Y} \mathbb{P}_\theta(h(X, \theta) = j) < 0 \right). \tag{3.3}$$

Breiman further analyzes the performance of the forest in terms of two key quantities: the **strength** of individual classifiers and the **correlation** between them. The strength s is defined as the expected margin:

$$s = \mathbb{E}_{X,Y} \left[\mathbb{P}_\theta(h(X, \theta) = Y) - \max_{j \neq Y} \mathbb{P}_\theta(h(X, \theta) = j) \right]. \tag{3.4}$$

The average correlation $\bar{\rho}$ quantifies the similarity in prediction errors across trees. The generalization error admits the following upper bound:

$$PE^* \leq \frac{\bar{\rho}(1-s^2)}{s^2}. \tag{3.5}$$

This inequality illustrates that to minimize error, one should aim for strong individual classifiers (high s) and low correlation between them (low $\bar{\rho}$).

In practice, each tree is trained using a technique called **bagging** (Bootstrap Aggregating), where the training set is sampled with replacement. Furthermore, at each node, a random subset of the input features is selected to determine the best partition, a method known as **random feature selection**. These sources of randomness are essential for reducing the correlation between trees and enhance the ensemble's robustness.

A particularly elegant feature of random forests is the use of **out-of-bag** (OOB) samples. Since each tree is trained on a bootstrap sample, roughly one-third of the data is not used for that tree and can be used as a validation set. This allows estimation of the generalization error, strength, correlation, and even variable importance, without needing a separate validation set.

For regression problems, the structure remains the same, except that the output of each tree is a real-valued prediction. The overall forest prediction is given by:

$$\hat{f}(x) = \frac{1}{K}\sum_{k=1}^{K} h(x, \theta_k). \tag{3.6}$$

The mean squared prediction error also converges:

$$\mathbb{E}_{X,Y}\left[\left(Y - \hat{f}(X)\right)^2\right] \to \mathbb{E}_{X,Y}\left[\left(Y - \mathbb{E}_\theta h(X,\theta)\right)^2\right], \tag{3.7}$$

and satisfies an analogous upper bound:

$$PE^*_{\text{forest}} \leq \bar{\rho} \cdot PE^*_{\text{tree}}, \tag{3.8}$$

where PE^*_{tree} is the average error of the individual trees.

In summary, Random Forests combine simplicity, flexibility, and strong empirical performance. They are accurate and robust to overfitting, handle noisy data well, scale effectively to high-dimensional inputs, and are competitive with boosting methods such as AdaBoost. Furthermore, they require little parameter tuning and can be easily parallelised, making them a practical choice for many real-world applications.

3.2 Support Vector Machine

The **Support Vector Machine (SVM)**, as introduced by Cortes and Vapnik in their seminal 1995 paper[81], is a supervised learning model designed for classification

problems. The central idea of SVMs is to find a decision boundary that not only separates the data but does so with the *largest possible margin*, thereby improving the model's generalization ability. The core intuition is to first map the input vectors $x \in \mathbb{R}^n$ into a high-dimensional feature space $\mathcal{Z}$ via a non-linear transformation $\phi(x)$, and then to find a hyperplane in this new space that best separates the data. The decision function is linear in the feature space, and takes the form $f(x) = \text{sign}(w \cdot \phi(x) + b)$, where w is the weight vector and b is the bias term.

The optimal hyperplane is defined as the one that maximizes the margin between the two classes, where the margin is the distance between the hyperplane and the nearest data points from each class, known as the *support vectors*. For linearly separable data, the optimization problem can be written as minimizing $\frac{1}{2}\|w\|^2$ subject to the constraints $y_i(w \cdot x_i + b) \geq 1$ for all i, where $y_i \in \{-1, +1\}$ are the class labels[81]. This is a convex quadratic programming problem, and the solution vector w can be expressed as a linear combination of the training inputs: $w = \sum_{i=1}^{\ell} \alpha_i y_i x_i$, where $\alpha_i \geq 0$ are Lagrange multipliers, and only the points that lie on the margin (i.e., the support vectors) have non-zero α_i. The classification function thus becomes $f(x) = \text{sign}\left(\sum_{i=1}^{\ell} \alpha_i y_i x_i \cdot x + b\right)$.

In the more general case where the data is not linearly separable, the formulation is extended with the introduction of slack variables $\xi_i \geq 0$ that allow for some margin violations, leading to the *soft margin SVM*. The corresponding optimization problem becomes minimising $\frac{1}{2}\|w\|^2 + C\sum_{i=1}^{\ell} \xi_i$, subject to $y_i(w \cdot x_i + b) \geq 1 - \xi_i$ and $\xi_i \geq 0$. Here, the regularisation parameter $C > 0$ controls the compromise between maximising the margin and minimising the classification error on the training data.

One of the most powerful aspects of the SVM is the so-called *kernel trick*, which enables the algorithm to operate in the high-dimensional feature space $\mathcal{Z}$ without explicitly computing $\phi(x)$. This is done by replacing all dot products $\phi(x_i) \cdot \phi(x_j)$ with a kernel function $K(x_i, x_j) = \phi(x_i) \cdot \phi(x_j)$. This allows efficient computation even when $\mathcal{Z}$ is extremely high- or even infinite-dimensional. Common choices of kernel functions include the linear kernel $K(x, x') = x \cdot x'$, the polynomial kernel $K(x, x') = (x \cdot x' + 1)^d$, and the radial basis function (RBF) or Gaussian kernel $K(x, x') = \exp\left(-\frac{\|x-x'\|^2}{2\sigma^2}\right)$[82]. The final classification function using kernels is then $f(x) = \text{sign}\left(\sum_{i=1}^{\ell} \alpha_i y_i K(x, x_i) + b\right)$.

From a theoretical perspective, Vapnik established a generalization bound based on the number of support vectors. Specifically, the expected error rate is bounded above by the ratio of the expected number of support vectors to the number of training examples:

$$\mathbb{E}[\text{error}] \leq \frac{\mathbb{E}[\text{number of support vectors}]}{\text{number of training samples}}$$

[83]. This implies that the fewer the support vectors, the better the generalization,

independent of the dimensionality of the feature space. Therefore, a well-constructed SVM with a small support set can generalize well even in spaces with millions or billions of dimensions.

The paper also presents extensive experimental results that compare SVMs with classical learning algorithms such as neural networks and k-nearest neighbors. In tasks such as handwritten digit recognition using the USPS and NIST datasets, SVMs with polynomial kernels of degrees up to 7 achieved error rates around 4.2%–4.3%, outperforming more complex neural networks like LeNet-1 and LeNet-4[84]. Remarkably, even with high-degree polynomials corresponding to feature spaces with 10^{16} dimensions, the SVMs showed no signs of overfitting, largely due to their margin-maximizing nature and the sparsity induced by the support vector expansion.

In conclusion, the support-vector network introduced by Cortes and Vapnik represents a significant progress in supervised learning, combining a solid theoretical foundation in VC theory, margin maximization, and convex optimization. It offers high flexibility through kernel functions, robustness to overfitting even in high dimensions, and consistently strong performance across a wide range of real-world classification problems. The use of the support vector expansion, kernel substitution, and soft margin formulation together forms a cohesive and powerful framework for statistical learning.

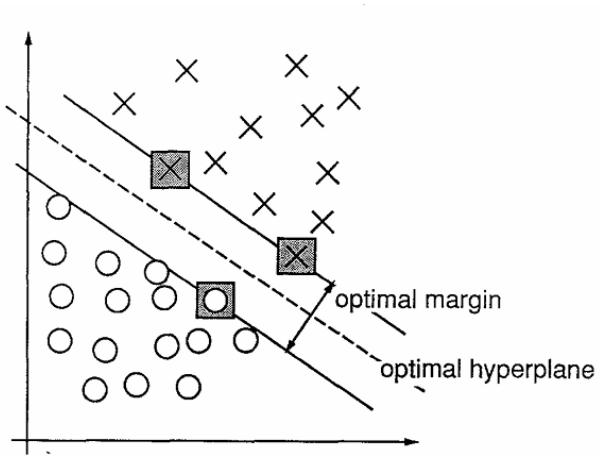

Figure 3.1: An example of a separable problem in a 2 dimensional space. The support vectors, marked with grey squares, define the margin of largest separation between the two classes. Adapted from[81].

Chapter 4

Materials and Methods

4.1 Instrumentation and Software

The instrumentation used in this research includes the Enobio 8 EEG headset by Neuroelectronics, equipped with eight channels to record EEG signals from participants. Real-time EEG visualization, data acquisition, and transfer between the Enobio headset and the computer were facilitated by NIC2 software. Participants listened to binaural beats using JBL TUNE 660NC headphones, while their ECG signals were recorded using a Polar H10 chest-strap heart rate sensor. Finally, MATLAB software, enhanced by several specialized toolboxes, was employed for audio generation and for the filtering, preprocessing, and analysis of the acquired EEG and ECG data.

4.1.1 Enobio 8

The Enobio 8, developed by Neuroelectrics, is a flexible and high-precision EEG device designed to meet the need for research and clinical applications. It features eight recording channels and supports DC coupling, offering a bandwidth that ranges from 0 Hz to 125 Hz. The system operates at a sampling rate of 500 samples/s and delivers a 24-bit dynamic range, allowing for the detection of EEG signals as small as 0.05 µV.

To ensure data fidelity, the Enobio 8 maintains measurement noise below 1 μV_{RMS} and features an input impedance greater than 1 GΩ, optimizing signal quality across all channels. In addition to EEG recording, the device incorporates a built-in three-axis accelerometer, capable of capturing movement data at 100 samples/s, which is particularly useful for monitoring subject motion during experiments[85].

The Enobio kit includes a neoprene cap (Figure 4.1) designed with 39 electrode positions, arranged following the international EEG 10–20 system. If additional

electrode positions are required, users can conveniently add new openings using the provided neoprene punch tool.

Figure 4.1: Enobio8 Neoprene cap[85].

The device supports wireless data transmission via Wi-Fi and includes a rechargeable battery that provides an operating time of approximately 16 h, facilitating unconstrained, mobile EEG sessions. The Enobio 8 is compatible with a variety of electrode types (Figure 4.2) , including Drytrodes (dry electrodes), NG Geltrodes (wet electrodes with conductive gel) and Foretrodes, which can be used either dry or with gel. This versatility allows for greater flexibility in experimental design and enhances participant comfort across different use cases.

For this research, NG Geltrode electrodes (Figure 4.2b) were chosen due to their advanced design, which allows direct scalp access after positioning the cap. This feature significantly simplifies skin preparation and gel application, improving the quality of the EEG signal. These electrodes are constructed from sintered silver/silver chloride (Ag/AgCl) pellets, each measuring 4 mm in diameter, ensuring excellent electrical conductivity, reliability, and superior signal integrity. The electrode contact surface is circular, covering an area of 1.75 cm^2. Furthermore, NG Geltrode electrodes show exceptional operational longevity, specifically designed to support continuous EEG recordings of up to 50 hours. This makes them especially suitable for extensive and intensive monitoring sessions, ensuring reliable and consistent EEG data collection.

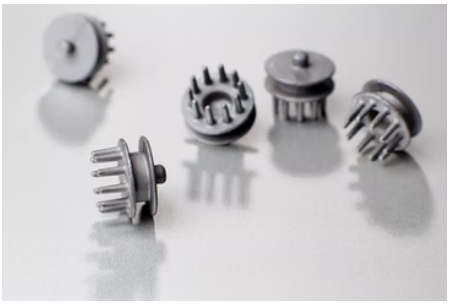

(a) Drytrode.

(b) NG Geltrode.

(c) Foretrode.

Figure 4.2: Types of electrodes compatible with the Enobio 8[85].

The conductive gel used was Neurgel (Figure 4.3) because of its advantageous properties suitable for application on intact skin. It serves as an effective medium between the body and the recording equipment, ensuring low impedance, high signal stability, and minimizing the risk of bridging effects between electrodes[86].

Figure 4.3: Conductive gel[86].

To facilitate the direct connection of the mandatory reference electrodes, Common Mode Sense (CMS) and Driven Right Leg (DRL), onto the mastoid skin, disposable oval-shaped FIAB electrodes (Figure 4.4) measuring 36x45 mm were selected. These electrodes feature a silver chloride (SSC) sensor, snap connection, foam backing, and solid gel, thus ensuring optimal electrical reference quality during EEG signal acquisition[87].

Figure 4.4: FIAB electrodes (F9089/100 - 36x45 mm)[87].

The electrodes are connected to the NecBox (Figure 4.5) through a dedicated connector (Figure 4.6) that provides eight channels for EEG electrodes and two additional channels for the CMS (Common Mode Sense) and DRL (Driven Right Leg) reference electrodes. The NecBox functions as the central unit of the Enobio 8 system, enabling signal acquisition, initial data processing, and wireless transmission to a computer. It operates on a self-contained, rechargeable battery with an approximate runtime of 6.5 hours. The device is securely attached to the neoprene cap using a Velcro patch, allowing for quick and efficient mounting[85].

Figure 4.5: Necbox[85].

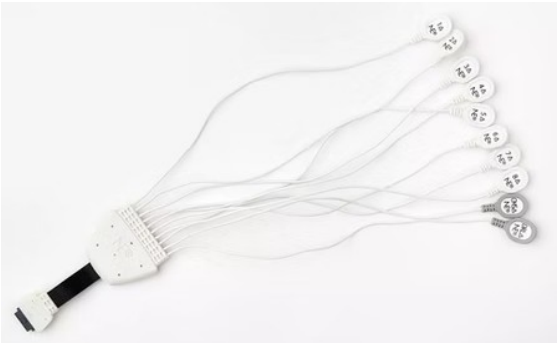

Figure 4.6: Dedicated connector[85].

4.1.2 NIC2 Software

The Neuroelectrics Instrument Controller (NIC), specifically the NIC2 version, is an integrated software environment designed for the comprehensive management of both Starstim and Enobio devices. It offers both basic and advanced operating modes, allowing users to design and monitor experiments involving electroencephalography (EEG) and/or non-invasive brain stimulation through transcranial current stimulation (tCS).

Once the NecBox is connected to the NIC software, the settings interface becomes available, enabling users to manage TCP connections to and from NIC2, activate double-blind mode, enable the synchronizer, or invert EEG signal polarity for display purposes. The software also provides the option to apply EEG line

noise filtering, with a 50 Hz filter for use in Europe and a 60 Hz filter for North America. Additionally, a bandpass filter can be applied to the EEG signal solely for visualization purposes[88].

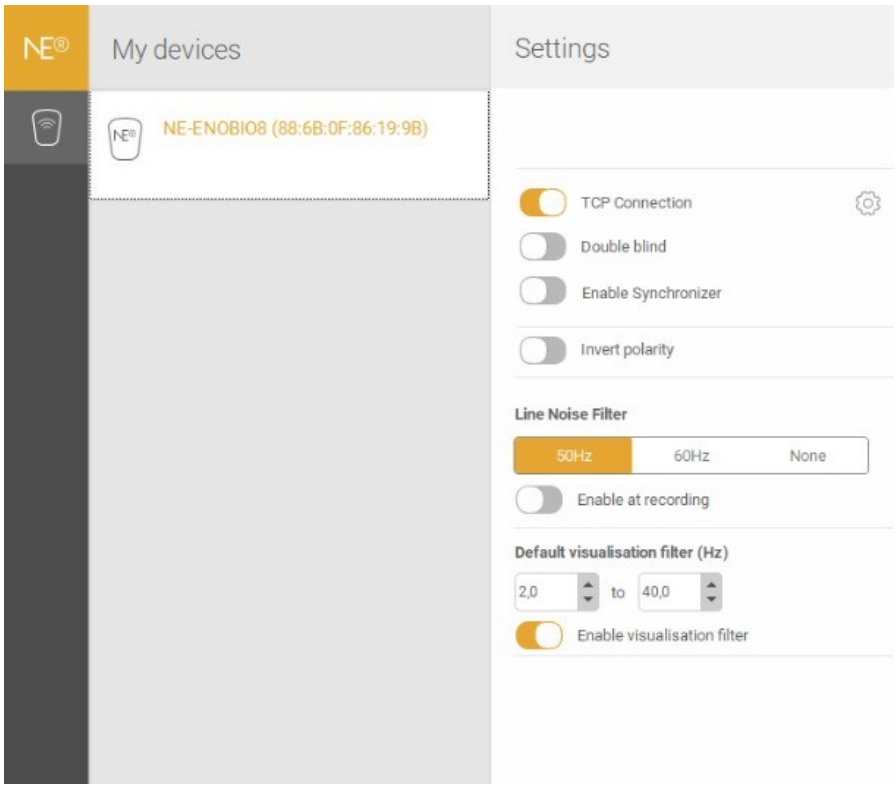

Figure 4.7: Setting used during registrations.

After configuring the initial settings, the next step involves creating the protocol (Figure 4.8), which may consist of one or multiple phases. In multi-phase protocols, the electrode montage must remain consistent across all phases, regardless of the specific function assigned to each channel. During this stage, users define the duration and electrode placement. A head diagram is displayed, illustrating the standard 10-10 coordinate system used in EEG recordings, accompanied by a predefined color-coding scheme:

- **Green:** Available positions under the current montage configuration;
- **Purple:** Channels assigned to EEG in the current phase;
- **Green with border:** Available positions currently assigned to EEG in other phases of the same protocol;
- **White:** Positions not available in standard montage models[88].

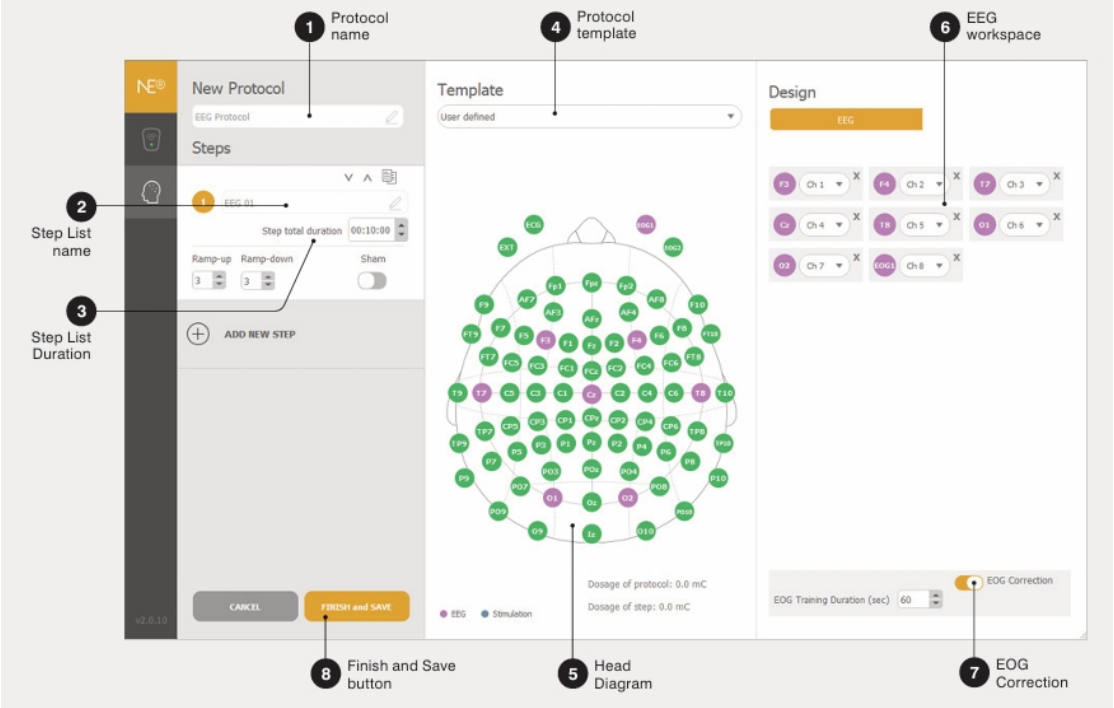

Figure 4.8: Protocol Design[88].

Once the protocol is loaded, the LiveView panels are launched (Figure 4.9), from which data recording can be initiated. These panels display the subject's EEG signals in real-time, even before the actual recording begins. Users can define a custom time window for signal visualization (with a default duration of 10 seconds), and this window is continuously updated in real time. The amplitude scale can be manually adjusted or set to automatic mode, which adapts the scaling dynamically based on the incoming signal.

In NIC2, EEG signal quality is evaluated using the Quality Index (QI), which is recalculated every two seconds. The QI is derived from four key parameters:

- **Line Noise:** Signal power (μV^2) within the line noise frequency band (50 Hz $\pm$ 1 in the EU; 60 Hz $\pm$ 1 in the US);
- **Main Noise:** Signal power within the standard EEG frequency band (1–40 Hz);
- **Offset:** Mean value of the EEG waveform;
- **Drift:** Although drift is measured, it is not included in the QI calculation due to high inter-subject variability. High drift values do not necessarily indicate poor signal quality[88].

The QI is computed based on the parameters listed above, using the following formula:

$$QI(t) = \tanh\left(\sqrt{\left(\frac{\text{Offset}(t)}{280\,\text{mV}}\right)^2 + \left(\frac{\text{MainNoise}(t)}{250\,\mu\text{V}}\right)^2 + \left(\frac{\text{LineNoise}(t)}{100\,\mu\text{V}}\right)^2}\right) \quad (4.1)$$

The QI follows a color-coded scheme:

- **Green (QI: 0.0–0.5):** Excellent signal quality;
- **Orange (QI: 0.5–0.8):** Good signal quality, sufficient for recording;
- **Red (QI: 0.8–1.0):** Poor signal quality.

However, occasional poor signal quality (red) during a recording session does not necessarily compromise the integrity of the ongoing test[88].

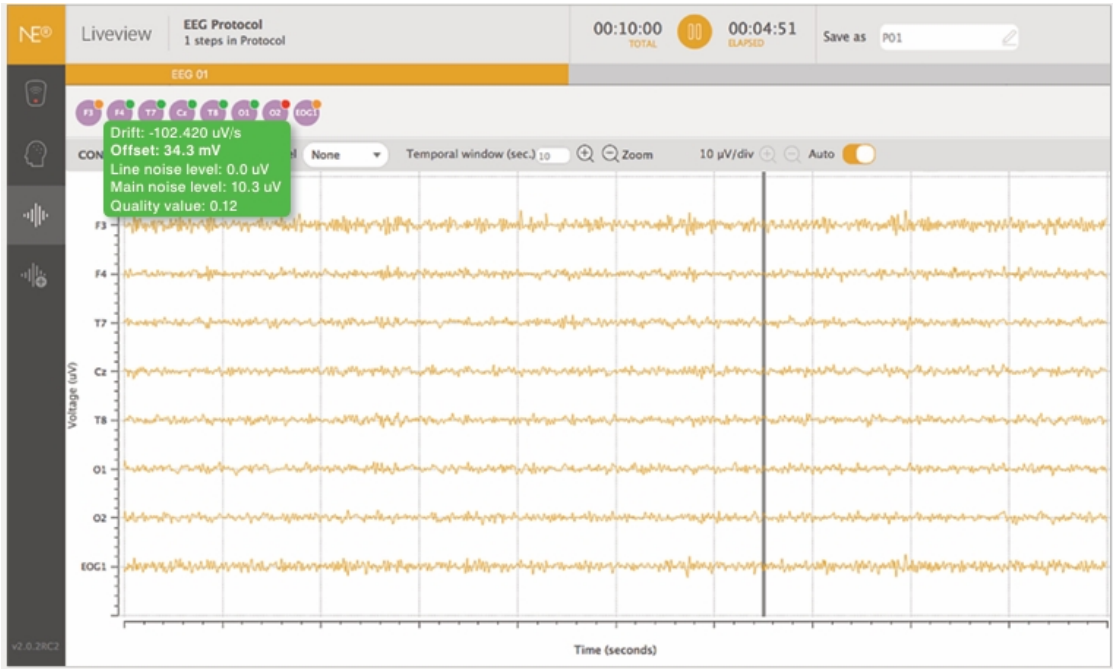

Figure 4.9: Example of EEG recording session[88].

In addition to real-time visualization of EEG signals, the LiveView panel provides access to several other graphical representations. Specifically, it allows real-time monitoring of the accelerometers embedded within the NecBox, the EEG spectrogram, band power distributions, a scalp map illustrating the spatial distribution of signal power, and a cortical map displaying the distribution of electrical dipoles across the brain surface[88].

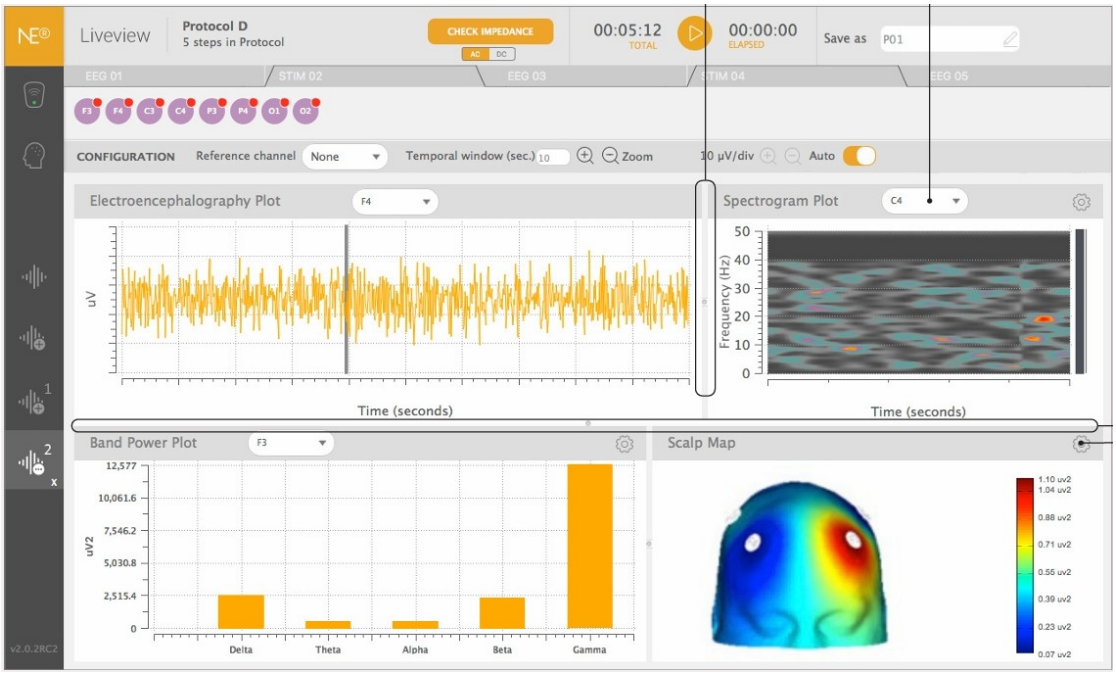

Figure 4.10: Example of EEG graphical features[88].

4.1.3 JBL TUNE 660NC

The headphones (Figure 4.11) used for the reproduction of binaural beats in this study were characterized by a frequency response range of 20 Hz to 20 kHz and an impedance of 32 Ω. They offer a sensitivity of 100 dB SPL at 1 kHz with an input power of 1 mW, and a maximum sound pressure level (SPL) of 96 dB. Furthermore, the device supports high-quality wireless audio streaming via Bluetooth 5.0, enabling a cord-free connection to smartphones or tablets, thereby enhancing usability and minimizing physical constraints during experimental sessions[89].

Figure 4.11: JBL TUNE 660NC[89].

4.1.4 Polar H10

The Polar H10 is a high-precision heart rate sensor used in this study for the acquisition of electrocardiographic (ECG) signals. It is paired with the Polar Pro chest strap, which ensures top-quality and interference-free electrical signal measurement. The sensor supports dual connectivity via Bluetooth® and ANT+™, enabling compatibility with a wide range of external devices and the possibility of two simultaneous Bluetooth connections. It also features an internal memory capable of storing one complete training session, which can be synchronized with the Polar Beat application after data acquisition. The device operates at a sampling frequency of 125 Hz, making it suitable for precise physiological monitoring.

The Polar H10 operates within a temperature range of –10 °C to +50 °C (14 °F to 122 °F), and is powered by a CR 2025 battery with an approximate lifespan of 400 hours. Its battery compartment is sealed using a silicone O-ring (20.0 x 0.90 mm) to ensure durability and resistance to moisture. The connector components are made of ABS, ABS reinforced with glass fiber, polycarbonate (PC), and stainless steel, offering both robustness and lightweight performance. The accompanying Polar Pro chest strap is machine-washable and constructed from a blend of 38% polyamide, 29% polyurethane, 20% elastane, and 13% polyester, with integrated silicone prints to enhance fit and stability during use[90].

Figure 4.12: Polar H10[90].

4.1.5 MATLAB

MATLAB is a high-level programming platform widely used by engineers and scientists worldwide to analyse data and design systems that shape modern innovation. Its applications span a wide range of domains, including active safety systems in automotive engineering, interplanetary space missions, medical monitoring devices, smart power grids, and LTE cellular networks. Within academic and research contexts, MATLAB is a fundamental tool for tasks such as machine learning, signal and image processing, computer vision, communication systems design, computational finance, robotics, and control systems engineering.

What makes MATLAB particularly effective in scientific and engineering workflows is its matrix-based language, which provides a natural and expressive way to perform complex numerical computations. The platform features a highly interactive desktop environment that supports iterative exploration, design, and problem solving. Integrated graphics and data visualization tools make it possible to quickly generate plots and gain insights from experimental results. In addition, MATLAB includes dedicated apps for activities such as curve fitting, data classification, signal analysis, and control system tuning.

To support a broad spectrum of research demands, MATLAB offers a large ecosystem of add-on toolboxes that cover specialised applications across engineering and science. These toolboxes provide pre-built algorithms that accelerate development and reduce the need to code from the beginning. Moreover, users can build custom applications using graphical user interfaces, further enhancing interactivity and usability.

MATLAB's interoperability is another key advantage: it interfaces seamlessly with languages such as C/C++, Java®, .NET, Python, SQL, and Microsoft® Excel®, allowing for the integration of MATLAB algorithms into broader software systems. The platform also supports high-performance computing workflows by enabling code execution on large datasets, computing clusters, and cloud environments.

Finally, MATLAB offers royalty-free deployment options, making it possible to share applications with end users without additional licensing requirements[91].

4.2 Experimental Protocol

4.2.1 Partecipants

The experimental sample consisted of 14 university students (7 males and 7 females), aged between 20 and 30 years, recruited from the University of Turin and the Polytechnic University of Turin. All participants reported no hearing loss or auditory disorders. The male subgroup had a mean age of 25.3 years (SD = ±1.4), while the female subgroup had a mean age of 22.3 years (SD = ±2.9), ensuring balanced gender representation in the sample.
Prior to participation, all subjects were instructed to abstain from recreational drug use for at least 24 hours, avoid caffeine intake for at least 12 hours, and ensure a minimum of 8 hours of sleep the night before the experiment. These requirements aimed to reduce the influence of external factors on EEG signal quality.
None of the participants had prior familiarity with binaural beats and were not informed in detail about the nature of the study or the experimental protocol, in order to minimize potential placebo effects. Informed consent was obtained from all participants for the processing and use of the data collected during the experimental sessions.

4.2.2 Experimental Setup

Participants were seated on a chair in a quiet room between 3:00 PM and 6:00 PM. This time window was chosen to ensure that subjects were not overly fatigued by daily activities. Throughout the entire duration of the test, participants were instructed to keep their eyes closed and to wear a sleep mask in order to minimize external distractions and maintain focus on the experimental task.
Once the neoprene EEG cap was fitted, access to the scalp was achieved through the predefined holes in the cap, where the electrodes were to be positioned. To prepare these sites, specialized plastic-tipped syringes (Figure 4.13) provided with the Enobio 8 kit were used. These syringes allowed for precise application of the conductive gel, after which the electrodes were inserted into place. The electrodes were selected to provide broad scalp coverage, enabling a comprehensive mapping of the participant's brain activity. Following the international 10–20 system, eight electrodes were placed: two frontal (F3, F4), two parietal (P3, P4), two temporal (T7, T8), and two occipital (O1, O2). The two reference electrodes, CMS (Common Mode Sense) and DRL (Driven Right Leg), were positioned on the left and right mastoid processes, respectively.

Figure 4.13: Curved plastic-tipped syringe[92].

To record the ECG signal, the Polar H10 chest strap was employed. It was positioned directly below the sternum and securely tightened to ensure optimal skin contact, while taking care not to overtighten, in order to avoid discomfort or restriction.
The setup used during the stimulation phase differed from the baseline configuration due to the addition of headphones, which were necessary for the delivery of the binaural beats.

Figure 4.14: Test setup.

Figure 4.15: Baseline setup.

4.2.3 Baseline

Once the instrumentation setup was completed, baseline EEG recording was initiated. The protocol involved a 5-minute recording session conducted in a quiet room, with participants instructed to keep their eyes closed and wear a sleep mask. Subjects were asked to relax and remain as still as possible to minimize motion-related artifacts, such as eye blinks and muscle movements, which could compromise signal quality.

Acquiring a clean baseline was a crucial step in the experimental procedure, as the resulting EEG data were subsequently used to determine the subject's Individual Alpha Frequency (IAF). IAF served as the customised frequency reference for generating subject-specific binaural beats in the following stages of the experiment.

Figure 4.16: Side view during Baseline Registration.

4.2.4 Estimation of Individual Alpha Frequency

The Individual Alpha Frequency (IAF) was computed using a custom MATLAB function, designed to analyze pre-filtered baseline EEG signals recorded from eight channels. The function takes three input parameters: the filtered EEG signal, the number of channels, and the sampling frequency. It returns the mean IAF across channels, the per-channel IAF values, the power spectral density, and the corresponding frequency vector.
To begin, the mean of the EEG signal was removed to eliminate DC offset. The power spectral density (PSD) was then estimated using Welch's method, with a Hamming window of length equal to the sampling frequency, an overlap of 50%, and an FFT length of 500.
IAF was determined by analyzing the alpha frequency band, defined in the range

of 7–13 Hz. The corresponding indices in the frequency vector were identified, and the PSD values within this band were extracted for each channel.
The IAF for each channel was computed as the spectral center of gravity using the formula:

$$\text{IAF}_i = \frac{\sum_{k=1}^{N} f_k \cdot P_i(f_k)}{\sum_{k=1}^{N} P_i(f_k)} \tag{4.2}$$

where:

- IAF_i is the individual alpha frequency for channel i,
- f_k is the k-th frequency in the alpha band,
- $P_i(f_k)$ is the power spectral density of channel i at frequency f_k,
- N is the number of frequency points in the alpha band.

After calculating IAF_i for all channels, the final IAF value for the subject was obtained by averaging the individual values:

$$\text{IAF}_{\text{mean}} = \frac{1}{C} \sum_{i=1}^{C} \text{IAF}_i \tag{4.3}$$

where C is the number of EEG channels considered ($C = 8$ in this case). The resulting IAF value was then rounded to two decimal places to facilitate interpretation and subsequent use in the experimental protocol.

4.2.5 Custom Binaural Beats

After acquiring the baseline EEG and computing the IAF, a customised MATLAB script was implemented to generate an auditory stimulation protocol composed of alternating sham and BBs segments. The main goal of this code was to produce a composite stereo audio signal used during the stimulation phase of the experiment, with BBs centered around each subject's IAF to ensure individualised neuromodulation.
The stimulation protocol alternates between sham audio segments and binaural beat impulses. Each impulse lasts 60 seconds and is followed by a sham signal of equal duration, repeated for a total of five cycles. The carrier frequency for the binaural beats was fixed at 250 Hz.

Sham Signal Generation:
The sham signal is defined as a stereo sinusoidal waveform with both channels

oscillating at the same frequency, set to the carrier frequency offset by half of the subject's IAF:

$$f_{\text{sham}} = f_{\text{carrier}} + \frac{\text{IAF}}{2} \tag{4.4}$$

This signal is generated over a time vector corresponding to the specified sham duration (60 seconds), and is duplicated across both audio channels to ensure no interaural frequency difference is present, thereby eliminating the binaural effect.

Binaural Beats Impulse:

Each binaural impulse is generated using the custom function, which creates a stereo sound signal by assigning different frequencies to the left and right channels:

- Left channel: a pure tone at the carrier frequency ($f_{\text{carrier}} = 250$ Hz)
- Right channel: the same tone modulated by the subject's IAF ($f_{\text{carrier}} + \text{IAF}$)

The difference in frequency between the two channels produces the perceptual illusion of a beat frequency equal to the IAF. The function returns a two-channel matrix, corresponding to the stereo signal.

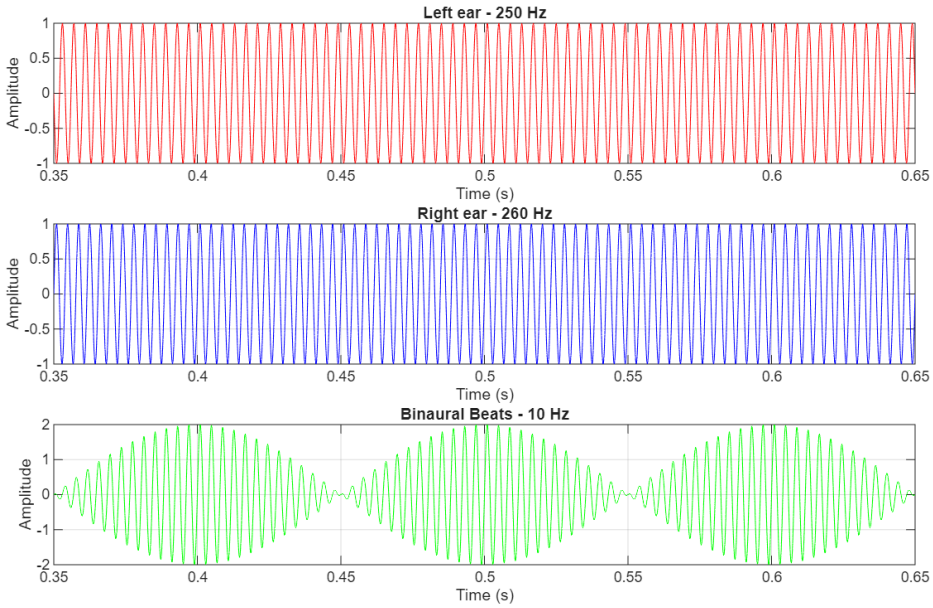

Figure 4.17: Example of BBs signal.

Signal Composition:

The complete stimulation signal is built by sequentially appending sham and BBs segments. A total of five repetitions are concatenated into a single stereo audio track, as follows:

$$\texttt{signal} = [\texttt{sham}, \texttt{BBs}, \texttt{sham}, \texttt{BBs}, \dots]$$

This alternating structure ensures controlled exposure to both conditions while maintaining consistent timing and frequency properties across subjects. The final signal is suitable for playback during EEG recording sessions and is designed to test the effects of IAF-based binaural stimulation under carefully matched control conditions. Additionally, the use of alternating stimuli aims to assess the immediate and acute effects of binaural beats, while minimizing the risk of drowsiness or sleep onset in participants during the session.

4.2.6 Experimental Procedure

Upon generation of personalized binaural beats, two identical 10-minute experimental sessions were conducted (Figure 4.19).
The participant was instructed to relax and remain motionless—as during the baseline recording—while listening to the generated signal. Throughout each session, the EEG signal was continuously monitored in order to promptly terminate the trial if adverse acquisition conditions arose (e.g., by tracking the signal QI to avoid prolonged periods of poor-quality data, and by observing the participant to prevent drowsiness or microsleeps that could compromise the results).
Between the two sessions, the participant removed both headphones and the eye mask for at least five minutes to reestablish baseline conditions and avoid any carry-over effects from the first session.

4.3 Signal Preprocessing and Analysis

In this chapter, we provide a detailed description of the preprocessing steps applied to EEG and ECG data. This procedure is critical for removing noise and artifacts, transforming raw signals into cleaner and more reliable forms from which relevant and representative features can be effectively extracted.

The selected features will be presented together with a detailed explanation of their types and the rationale behind their inclusion. This will be followed by a description of the feature selection method applied. Special emphasis will also be placed on the handling of outliers, a critical step aimed at improving the robustness of the analysis and ensuring the reliable detection of meaningful signal patterns, thereby minimizing the risk of drawing inaccurate or misleading conclusions.

Test 1

Test 2

Figure 4.18: EEG traces recorded during the testing sessions. Particular attention is drawn to channels P3–P4–O1–O2, in which the alpha-wave frequency is clearly discernible.

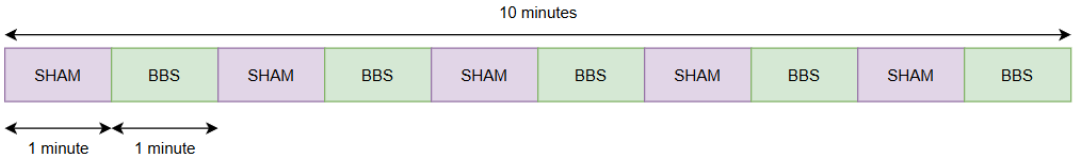

Figure 4.19: 10 minutes session used.

To facilitate this process, several MATLAB scripts were developed to automate the preprocessing workflow. These scripts consistently convert the raw signals from each subject into a structured data set containing the top features selected, simplifying subsequent analyses through improved data organisation and consistency.

4.3.1 EEG filtering

To effectively filter the EEG signal, a fifth-order Butterworth bandpass filter was implemented. This type of filter was selected for its ability to significantly attenuate frequency components outside the desired frequency band, while simultaneously preserving the temporal structure and shape of the original EEG signal. Specifically, the bandpass range was set between 4,Hz and 40,Hz, corresponding to a sampling frequency (Fc) of 500 Hz (Figure 4.20).

The filter was applied using MATLAB's `filtfilt` function, which performs forward-backward filtering to achieve zero-phase distortion (Figure 4.21). This characteristic is particularly important for EEG analysis, as it prevents temporal misalignment that could otherwise compromise subsequent analytical procedures. The outcome of this filtering process is a clean EEG signal, substantially free from high-frequency noise, such as electrical interference, and low-frequency components arising from baseline drift or movement-related artifacts. Consequently, this approach effectively retains the spectral integrity of the EEG within the target frequency range, facilitating reliable feature extraction and advanced statistical analyses.

It should be noted that during EEG acquisition, the Enobio8 device inherently applies a notch filter at 50,Hz, further reducing interference from the electrical mains.

Following bandpass filtering, any remaining artifacts were identified by applying a threshold corresponding to three times the standard deviation of the signal. Detected outlier points were subsequently removed and replaced via linear interpolation between the adjacent signal segments, ensuring continuity and integrity of the EEG data.

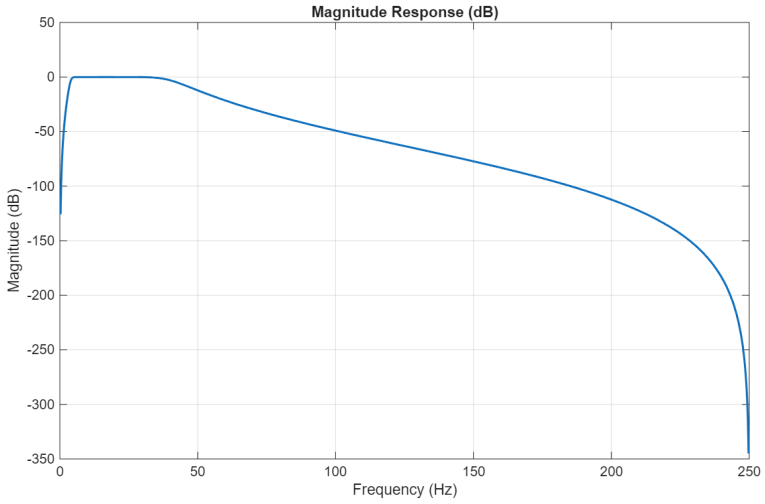

Figure 4.20: EEG frequency response filter.

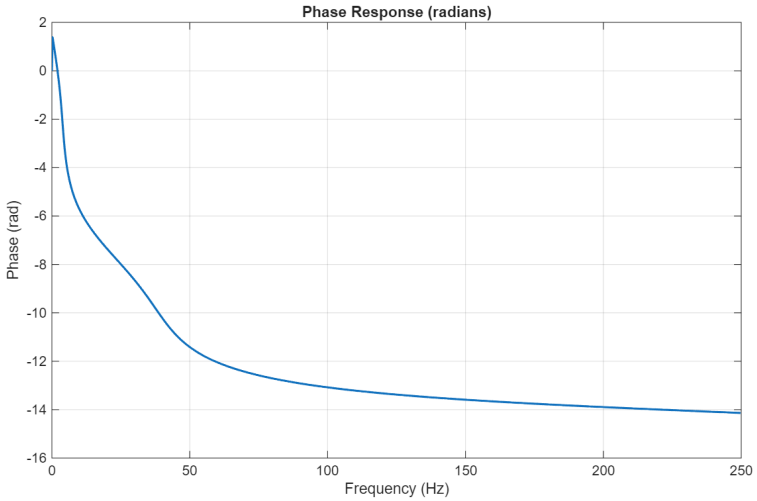

Figure 4.21: EEG phase response filter.

4.3.2 ECG filtering

The electrocardiographic (ECG) signal required resampling at a consistent frequency of 125 Hz due to the inherent variability in the sampling rate provided by the Polar H10 device, which typically records data slightly above 125 Hz but without a constant sampling interval. This resampling step leads to only a negligible loss of data points, which does not significantly impact the quality or subsequent

analyses of the ECG signal.

Following resampling, the ECG recordings were filtered to remove unwanted noise while preserving physiological features essential for accurate analysis. Specifically, a sixth-order Butterworth bandpass filter with a passband ranging from 0.5 Hz to 50 Hz was implemented. The characteristics of this filter were selected to effectively eliminate baseline wander (low-frequency noise below 0.5 Hz) and high-frequency interference (above 50 Hz), without distorting the clinically significant components of the ECG signal, such as the P wave, QRS complex, and T wave.

This implementation ensures minimal phase distortion, particularly when applied in forward-backward mode (zero-phase filtering), thus maintaining the integrity of the ECG waveform for accurate interpretation and subsequent analytical procedures.

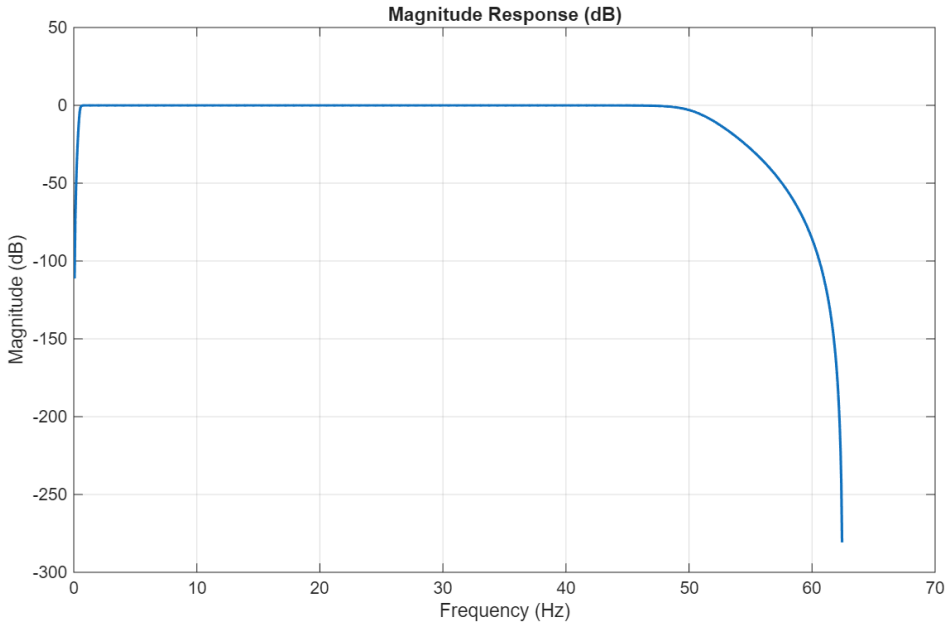

Figure 4.22: ECG filter response.

4.3.3 Signal Segmentation

The signals were segmented while maintaining the distinction between recordings acquired during the Sham condition and those recorded during the presence of Binaural Beats. This choice was made to analyze the two events separately and highlight the characteristic values associated with each condition. As a result, 10 "Sham" and 10 "BBs" recordings (divided into Test 1 and Test 2) were obtained for

each subject.

An additional segmentation step was carried out to significantly increase the amount of available data, evaluate potential Brainwave Entrainment effects [58], and observe the temporal evolution of the features computed in subsequent steps. To this end, each of the previously obtained recordings was divided into 4 segments of 15 seconds each, resulting in a total of 80 recordings per subject across both "BBs" and "Sham" conditions.

4.4 Feature Extraction

One of the key steps of the project is undoubtedly feature extraction. The main objective is to extract features that are as representative as possible of the phenomenon being analyzed, aiming to highlight distinctive aspects. To achieve this, a thorough analysis of the relevant literature was necessary.

In this chapter, we will analyze in detail the calculated features and the criteria employed for their selection. Overall, 148 features were computed from EEG and ECG signals, distributed as follows:

- **EEG**: 16 features (many of which are multi-channel);
- **ECG**: 4 features.

Subsequently, after feature selection (See Section 4.5), these features will be employed in the construction of classifiers aimed at identifying the two experimental conditions, namely BBs and Sham.

4.4.1 EEG Features

EEG signals are characterized by considerable randomness and variability due to the complex nature of brain activities and their sensitivity to physiological and external conditions. Thus, selecting robust and distinctive features becomes crucial to effectively capture meaningful information and patterns from EEG recordings. The chosen features reflect both temporal and frequency domain characteristics, ensuring comprehensive representation of the underlying neurological processes.

- Time Domain Features

- **Hjorth Parameters**

  Hjorth parameters are statistical descriptors originally introduced by Bo Hjorth in 1970 to quantify the time-domain characteristics of EEG signals [93].

They provide a compact representation of signal dynamics through three measures: Activity, Mobility, and Complexity. These features are computationally efficient and widely used in EEG signal processing.

Given a discrete EEG signal $x(t)$ from one channel, the Hjorth parameters are defined as follows:

- **Activity (HA)** : Represents the signal variance and is a measure of its power. It reflects the overall amplitude of the signal fluctuations.
  High Activity indicates a signal with large amplitude fluctuations and is typically associated with states of increased neural engagement or the presence of artifacts (e.g., muscle activity or eye blinks).
  Low activity, conversely, may suggest a relaxed state or low signal variance due to noise suppression or inactivity.

$$HA = \text{var}(x(t)) = \frac{1}{N}\sum_{i=1}^{N}(x_i - \mu)^2 \tag{4.5}$$

  where μ is the mean of the signal and N is the number of samples.

- **Mobility (HM)**: Represents the mean frequency or the proportion of the standard deviation of the signal's first derivative to that of the signal itself.
  High Mobility suggests the presence of higher frequency components in the EEG signal, potentially indicative of alertness or attention.
  Low mobility denotes a signal dominated by low-frequency content, such as those observed during sleep or drowsiness.

$$HM = \sqrt{\frac{\text{var}(\dot{x}(t))}{\text{var}(x(t))}} \tag{4.6}$$

  where $\dot{x}(t)$ denotes the first derivative of the signal.

- **Complexity (HC)**: Reflects the change in frequency or the deviation from a pure sine wave. It is calculated as the ratio of the mobility of the first derivative of the signal to the mobility of the signal itself.
  High Complexity reflects a more irregular or rapidly changing waveform, indicating that the signal contains more intricate frequency modulations. This is often seen in cognitive tasks or when the brain is responding to dynamic stimuli.
  Low complexity implies that the signal is closer to a pure sinusoidal form or exhibits relatively uniform oscillatory behavior.

$$HC = \frac{HM(\dot{x}(t))}{HM(x(t))} = \frac{\sqrt{\frac{\text{var}(\ddot{x}(t))}{\text{var}(\dot{x}(t))}}}{\sqrt{\frac{\text{var}(\dot{x}(t))}{\text{var}(x(t))}}} \tag{4.7}$$

where $\ddot{x}(t)$ is the second derivative of the signal.

These parameters were computed independently for each of the 8 EEG channels in order to characterize the local temporal dynamics of the brain activity.

- **Higuchi Fractal Dimension**

The Higuchi Fractal Dimension (HFD) provides a quantitative measure of complexity and self-similarity in biomedical signals, particularly EEG signals. Introduced by Higuchi in 1988 [94], HFD has been widely adopted due to its effectiveness in characterizing the intricate dynamics of EEG waveforms, offering insights into neurological conditions, cognitive states, and pathologies [95].

The fundamental idea behind HFD involves segmenting the original EEG signal into multiple subsets and evaluating their fractal-like behavior. Specifically, given a discrete EEG time series , subsets are formed according to an integer parameter , defined as follows:

$$X_m^k : x(m), x(m+k), x(m+2k), \ldots, x\left(m + \left\lfloor \frac{N-m}{k} \right\rfloor k\right), \quad m = 1,2,\ldots,k. \tag{4.8}$$

For each subset, the length is computed as:

$$L_m(k) = \frac{N-1}{\left\lfloor \frac{N-m}{k} \right\rfloor k^2} \sum_{i=1}^{\left\lfloor \frac{N-m}{k} \right\rfloor} |x(m+ik) - x(m+(i-1)k)| . \tag{4.9}$$

The average length of all subsets is then calculated by averaging over :

$$L(k) = \frac{1}{k} \sum_{m=1}^{k} L_m(k). \tag{4.10}$$

Ultimately, the Higuchi fractal dimension is obtained from the slope of the linear regression of against , mathematically represented as:

$$\text{HFD} = \frac{d(\log(L(k)))}{d(\log(1/k))}. \tag{4.11}$$

In this analysis, the parameter is typically selected based on the resolution and length of the EEG data segments analyzed. For the present study examining alpha-band EEG activity under sham and BBs conditions, $K_{\max}$ was set to 125. This value ensures a balanced compromise between computational efficiency and accurate estimation of complexity, allowing sufficient detail to differentiate subtle changes in alpha-band dynamics between conditions.

HFD values typically range from 1 to 2, with higher values indicating increased signal complexity and lower values reflecting more regular or deterministic behavior. Thus, higher HFD values may be associated with enhanced neural processing or states of increased cognitive engagement.

- **Katz Fractal Dimension**

The Katz Fractal Dimension (KFD) is a widely utilized nonlinear metric that quantifies complexity and self-similarity characteristics of biomedical signals, including EEG data. Initially proposed by Katz in 1988 [96], this metric is particularly valuable in analyzing temporal dynamics of EEG signals, enabling the discrimination of physiological and pathological states.

KFD quantifies signal complexity based on the waveform's length and diameter. Given a discrete EEG time series , KFD calculation involves several steps. First, the total length of the EEG waveform is computed as the sum of the Euclidean distances between successive data points:

$$L = \sum_{i=1}^{N-1} \sqrt{(x(i+1) - x(i))^2 + 1}. \tag{4.12}$$

Subsequently, the waveform's diameter , defined as the maximal Euclidean distance between the first data point and any other point of the series, is calculated:

$$d = \max_{i=2,\ldots,N} \sqrt{(x(i) - x(1))^2 + (i-1)^2}. \tag{4.13}$$

Finally, the Katz Fractal Dimension is obtained by:

$$\text{KFD} = \frac{\log_{10}(n)}{\log_{10}(n) + \log_{10}(d/L)}, \quad \text{where } n = N - 1. \tag{4.14}$$

For EEG signal analysis, KFD typically yields values greater than or equal to 1, with a perfectly linear signal corresponding exactly to a value of 1. Higher values of KFD indicate increased complexity, irregularity, or randomness in the

EEG signal, reflecting enhanced neural dynamical processes or pathological conditions. Thus, KFD is frequently employed to differentiate cognitive states, detect neurological disorders, or characterize EEG alterations induced by various stimuli.

- **Petrosian Fractal Dimension**

The Petrosian Fractal Dimension (PFD) is a fast and efficient algorithm for estimating the fractal complexity of time series. Originally introduced by Petrosian in the context of signal classification, this metric captures subtle variations in signal irregularity and structural changes [97].

Given a discrete EEG time series $X = \{x_1, x_2, \ldots, x_N\}$, the Petrosian Fractal Dimension is calculated based on the number of sign changes in the first derivative of the signal. The steps are as follows:

1. Compute the length N of the signal.
2. Compute the first-order difference (approximate derivative):

$$\Delta x_i = x_{i+1} - x_i, \quad i = 1, \ldots, N-1. \tag{4.15}$$

3. Count the number M of sign changes in Δx, i.e., the number of times the signal changes direction:

$$M = \sum_{i=1}^{N-2} [\text{sign}(\Delta x_{i+1}) \neq \text{sign}(\Delta x_i)]. \tag{4.16}$$

4. Compute the Petrosian Fractal Dimension:

$$\text{PFD} = \frac{\log_{10}(N)}{\log_{10}(N) + \log_{10}\left(\frac{N}{N+0.4M}\right)}. \tag{4.17}$$

This measure provides a balance between simplicity and sensitivity to signal irregularity.

Low PFD values indicate more regular, less complex signals—often associated with synchronized neural activity or resting states. Higher PFD values reflect increased signal irregularity and complexity, which may indicate more dynamic or desynchronized neural states.

- **Skewness**

Skewness is a statistical measure that quantifies the asymmetry of a probability

distribution around its mean. In the context of EEG signal analysis, skewness provides insights into the temporal distribution characteristics of brain activity, particularly useful in detecting deviations from normal physiological behavior.

Given a discrete time series $X = \{x_1, x_2, \ldots, x_N\}$, the skewness γ is computed as:

$$\gamma = \frac{1}{N} \sum_{i=1}^{N} \left(\frac{x_i - \mu}{\sigma} \right)^3, \tag{4.18}$$

where μ is the sample mean and σ is the standard deviation of the signal. Skewness values can be interpreted as follows:

- $\gamma = 0$: Symmetrical distribution of EEG amplitudes around the mean, often associated with normal or baseline brain activity.
- $\gamma > 0$: Indicates a distribution with a longer or fatter tail on the right side. In EEG, this may reflect transient bursts or artifacts leading to higher amplitude deviations.
- $\gamma < 0$: Indicates a distribution with a longer or fatter tail on the left side. This could correspond to prolonged low-amplitude activities or suppression in EEG signals.

In this study, skewness was calculated using MATLAB's built-in `skewness` function, which computes the sample skewness by applying the standardized third moment of the EEG signal segments. This approach ensures consistent and accurate estimation of signal asymmetry across different experimental conditions.

Skewness can reveal underlying nonlinearities and distributional biases in EEG activity, particularly in responses to stimulation or altered cognitive states.

- **Kurtosis**

Kurtosis is a higher-order statistical moment that quantifies the "tailedness" of a probability distribution. In EEG signal analysis, it serves as a valuable metric for identifying sharp transients or outlier behavior, such as those associated with artifacts or epileptic spikes.

Given a discrete time series $X = \{x_1, x_2, \ldots, x_N\}$, the kurtosis κ is defined as:

$$\kappa = \frac{1}{N} \sum_{i=1}^{N} \left(\frac{x_i - \mu}{\sigma} \right)^4, \tag{4.19}$$

where μ is the sample mean and σ is the standard deviation of the signal. This equation captures the normalized fourth central moment of the distribution.

The interpretation of kurtosis in EEG data is as follows:

- $\kappa > 3$: leptokurtic distribution, indicating sharp peaks and heavy tails—often associated with artifacts or transient neural events.
- $\kappa < 3$: platykurtic distribution, indicating flatter peaks and lighter tails—suggesting a more uniform signal.
- $\kappa \approx 3$: mesokurtic, similar to a normal distribution—indicative of typical background EEG.

Kurtosis was computed using MATLAB's built-in `kurtosis` function, which standardizes the fourth moment by the square of the variance and adjusts for sample bias. This automated calculation enables efficient assessment of amplitude variability and rare events across EEG segments.

- **Permutation Entropy**

Permutation Entropy (PE) is a robust complexity measure introduced by Bandt and Pompe (2002)[98], widely used in the analysis of nonlinear and chaotic time series such as EEG signals. It quantifies the disorder or unpredictability of a signal by examining the relative ordering of values within short subsequences.

Given a univariate discrete time series $X = \{x_1, x_2, \ldots, x_N\}$, the PE algorithm relies on two main parameters:

- Embedding dimension m: the length of the ordinal patterns.
- Time delay τ: the lag between successive elements in the embedding (commonly $\tau = 1$).

From these parameters, a sequence of overlapping vectors is formed:

$$V_i = \{x_i, x_{i+\tau}, x_{i+2\tau}, \ldots, x_{i+(m-1)\tau}\}, \quad i = 1, 2, \ldots, N - (m-1)\tau. \tag{4.20}$$

Each vector is mapped to a permutation pattern based on the relative ranking of its values. The relative frequencies p_j of each of the $m!$ possible patterns are then computed.

The Permutation Entropy is defined as:

$$PE = -\sum_{j=1}^{m!} p_j \log_2(p_j), \tag{4.21}$$

with the convention that $0 \log(0) = 0$.

A custom MATLAB was implemented to calculate PE, where m = 5 and τ = 1 were chosen as appropriate values for 15-second EEG segments, following standard practices.

PE values typically range from 0 to $\log_2(m!)$. In EEG analysis, low PE values indicate a more ordered, regular, and predictable dynamic of the EEG signal. This may reflect increased neuronal synchrony or a state of reduced cortical activation, while high PE values may reflect disorganized neural activity, increased cortical activation, or physiological noise because the signal becomes more complex and unpredictable.

- Frequency Domain Features

- **Alpha band power**

The alpha band power (typically defined as the spectral power in the 7–13 Hz frequency range, f_α) quantifies the amount of neural activity occurring in this rhythm, which has been associated with relaxed wakefulness, closed eyes, and reduced cognitive workload [99]. It is computed as:

$$P_\alpha = \int_{f \in f_\alpha} |X(f)|^2 \, df, \quad \text{where } X(f) = \mathcal{F}\{x(t)\} \tag{4.22}$$

where $x(t)$ is the EEG signal in the time domain and $X(f)$ is its Fourier Transform. The squared magnitude $|X(f)|^2$ represents the Power Spectral Density (PSD), and the integral yields the total power within the alpha band.

Alpha band power is commonly used in EEG analysis because it reflects cortical idling and inhibition, and is modulated by attentional and emotional states [100]. In the context of auditory stimulation using BBs, alpha power serves as a reliable biomarker of neural entrainment and relaxation. Binaural beats designed in the alpha range aim to induce or enhance alpha oscillations in the brain, and a measurable increase in alpha power during or after stimulation suggests a successful modulation of endogenous rhythms [48]. Therefore, alpha power is a relevant and physiologically meaningful index for evaluating the effects of binaural beat stimulation in neurophysiological studies.

- **Alpha/Beta Power Ratio**

The Alpha/Beta Power Ratio (ABR) is defined as the ratio between the total power in the alpha band (7–13 Hz,f_α) and the total power in the beta

band (typically 13–30 Hz,f_β). It provides a normalized index reflecting the balance between relaxed (α) and alert or cognitive (β) neural activity [101]. The ABR is calculated as:

$$\text{ABR} = \frac{P_\alpha}{P_\beta} = \frac{\int_{f \in f_\alpha} |X(f)|^2 \, df}{\int_{f \in f_\beta} |X(f)|^2 \, df} \tag{4.23}$$

where $X(f) = \mathcal{F}\{x(t)\}$ is the Fourier Transform of the EEG signal $x(t)$, and $|X(f)|^2$ denotes its PSD.

This ratio is particularly relevant when studying the effects of BBs, especially those targeting alpha entrainment. An increased ABR may indicate a shift toward a more relaxed or meditative brain state, as alpha power increases relative to beta, which is often associated with active thinking, anxiety, or arousal[102]. As such, the ABR is a useful index for evaluating brain states influenced by rhythmic auditory stimulation and can complement absolute power analyses by providing a relative measure of cortical activity balance [103].

- **Alpha/Theta Power Ratio**

The Alpha/Theta Ratio (ATR) is a commonly used EEG metric that quantifies the balance between alpha (7–13 Hz,f_α) and theta (4–7 Hz,f_θ) oscillatory activity. It is defined as:

$$\text{ATR} = \frac{P_\alpha}{P_\theta} = \frac{\int_{f \in f_\alpha} |X(f)|^2 \, df}{\int_{f \in f_\theta} |X(f)|^2 \, df} \tag{4.24}$$

where $X(f) = \mathcal{F}\{x(t)\}$ is the Fourier Transform of the EEG signal $x(t)$, and $|X(f)|^2$ is its Power Spectral Density (PSD).

The Alpha/Theta Ratio has been widely employed to evaluate meditative states, relaxation, and cognitive transitions. A high ATR is generally associated with a relaxed yet alert mental state, whereas a low ATR may reflect drowsiness, hypnagogic states, or decreased arousal[104].
In the context of *binaural beats*, the ATR is a sensitive indicator of neurophysiological changes induced by low-frequency auditory stimulation. For example, binaural beats designed to entrain alpha oscillations can result in an increased ATR, signaling a shift from internally focused or sleepy states (theta) toward more relaxed wakefulness (alpha). This makes the ATR particularly suitable

for assessing cognitive and emotional responses to auditory stimulation and neurofeedback.

- **Spectral Centroid**

  Spectral centroid is a feature that represents the weighted average frequency of a power spectrum and is often interpreted as an indicator of the spectral "center of gravity". In EEG analysis, it provides insight into the overall frequency shift of brain activity and can reflect changes in cortical activation or arousal states. It is defined as:

$$C = \frac{\sum_{i=1}^{N} f_i \cdot P(f_i)}{\sum_{i=1}^{N} P(f_i)} \tag{4.25}$$

  where f_i represents the i-th frequency bin and $P(f_i)$ is the corresponding PSD.

  In the context of this research using, the spectral centroid can help identify global shifts in EEG frequency content, such as increased high-frequency activity (e.g., beta) or enhanced low-frequency rhythms (e.g., alpha or theta), which are often associated with cognitive modulation, relaxation, or entrainment effects induced by the auditory stimulation. Thus, it serves as a complementary feature to traditional band-specific power measures for capturing broader spectral dynamics.

- **Shannon Entropy**

  Shannon entropy provides a single-value measure of the complexity and unpredictability of an EEG signal's amplitude distribution[105], it is especially useful to detect changes in neural dynamics induced by binaural-beat stimulation.[106] Because EEG complexity reflects the richness of underlying brain activity, Shannon entropy can capture subtle modulations in amplitude patterns during auditory entrainment paradigms[105].
  Moreover, binaural beats modulate low-frequency power and phase dynamics, producing measurable shifts in entropy that correlate with perceptual and cognitive effects[107].
  Entropy computation is efficient and robust to noise.

$$H(X) = -\sum_{i=1}^{n} p(x_i)\ \log_2 p(x_i) \tag{4.26}$$

  In this equation:
  $H(X)$ denotes the Shannon entropy of the discrete random variable X, representing the EEG amplitude or power values over time.

$p(x_i)$ is the probability of observing the value x_i, estimated from the empirical distribution of EEG data.
$\log_2 p(x_i)$ quantifies the information content (in bits) of the outcome x_i.

The summation runs over all possible discrete states x_i in the support of X, and the negative sign ensures that entropy is non-negative.

- **Spectral Coherence**

  Spectral coherence quantifies the linear correlation between two EEG signals at a specific frequency, reflecting the degree of phase synchrony between cortical regions[108].
  It is particularly relevant in EEG studies involving binaural beats, where neural entrainment and connectivity patterns may be modulated by rhythmic auditory stimulation[75].

$$C_{xy}(f) = \frac{|\mathcal{S}_{xy}(f)|^2}{\mathcal{S}_{xx}(f)\,\mathcal{S}_{yy}(f)} \tag{4.27}$$

  In this equation:
  $C_{xy}(f)$ is the magnitude-squared coherence between signals $x(t)$ and $y(t)$ at frequency f.
  $\mathcal{S}_{xy}(f)$ is the cross-spectral density between x and y, representing their shared power at frequency f.
  $\mathcal{S}_{xx}(f)$ and $\mathcal{S}_{yy}(f)$ are the auto-spectral densities of x and y, respectively.
  The coherence value ranges from 0 (no linear relationship) to 1 (perfect phase locking) at the given frequency.

- **Phase-Locking Value(PLV)**

  The Phase Locking Value (PLV) quantifies the stability of phase differences between two EEG signals over time, serving as a robust index of neural synchrony that is independent of signal amplitude[109].

  It is particularly useful for capturing frequency-specific functional connectivity between cortical regions, especially during cognitive or sensory tasks where oscillatory coordination plays a key role[110].

  PLV is frequently employed in studies of brain–brain and brain–stimulus interactions, and is sensitive to modulations induced by rhythmic auditory stimulation such as binaural beats[75].

$$\text{PLV} = \left| \frac{1}{N} \sum_{k=1}^{N} e^{j(\phi_x(k) - \phi_y(k))} \right| \tag{4.28}$$

In this equation:
$\phi_x(k)$ and $\phi_y(k)$ denote the instantaneous phase of EEG signals x and y at time point k, typically extracted using the Hilbert transform or complex Morlet wavelets.

N is the number of samples in the analysis window, and j is the imaginary unit.

The resulting PLV ranges from 0 to 1: a value near 1 indicates highly consistent phase differences (strong phase synchrony), while values near 0 reflect a lack of stable phase relationship.

Because PLV focuses solely on phase information, it is robust to artifacts in amplitude and useful in noisy or low-SNR EEG environments.

Binaural beats, by presenting slightly different frequencies to each ear, can entrain brain oscillations in specific frequency bands. PLV is a suitable measure to detect the emergence of phase-locked neural activity across regions in response to this rhythmic stimulation, making it an effective tool for studying large-scale synchronization phenomena[52].

4.4.2 ECG Features

- **Heart Rate**

  Heart rate (HR), typically measured in beats per minute (bpm), is a key indicator of autonomic nervous system (ANS) activity and physiological arousal.

  In the context of binaural beat stimulation (BBS), HR monitoring provides insight into how auditory-induced entrainment affects bodily relaxation or alertness states.

  Heart rate is commonly extracted from electrocardiogram (ECG) or photoplethysmographic (PPG) signals using peak detection algorithms that identify successive R-waves or pulse peaks.

  From this, the instantaneous HR is computed as:

$$\mathrm{HR}(t) = \frac{60}{\mathrm{RR}_i} \tag{4.29}$$

where RR_i is the interval (in seconds) between two consecutive heartbeats at time t (also known as the RR interval).

Binaural beats, particularly in the alpha band (7–13 Hz), are often associated with relaxation and reduced mental workload[111].
Multiple studies report that listening to alpha-frequency BBs can lead to a modest decrease in heart rate, suggesting a shift toward parasympathetic dominance and reduced arousal.
This effect supports the use of BBs as a tool in stress reduction, mindfulness practices, and cognitive recovery protocols[112].

- **Standard Deviation of NN Intervals(SDNN)**

  Heart Rate Variability (HRV) refers to the variation in time intervals between successive heartbeats and reflects the dynamic balance of sympathetic and parasympathetic activity within the autonomic nervous system (ANS).

  A commonly used time-domain measure of HRV is the SDNN, the standard deviation of normal-to-normal (NN) intervals:

$$\mathrm{SDNN} = \sqrt{\frac{1}{N-1}\sum_{i=1}^{N}\left(\mathrm{RR}_i - \overline{\mathrm{RR}}\right)^2} \tag{4.30}$$

  In this equation:
  RR_i is the duration of the i-th normal beat-to-beat interval,
  $\overline{\mathrm{RR}}$ is the mean of all RR intervals, and
  N is the total number of intervals within the analysis window.

  SDNN is expressed in milliseconds and represents overall heart rate variability — higher values generally indicate greater parasympathetic modulation and cardiovascular flexibility.
  Studies have shown that binaural beat stimulation, particularly in the alpha or theta frequency range, can influence SDNN values. Exposure to alpha-frequency BBs is often associated with increased SDNN, suggesting a shift toward parasympathetic dominance and a more relaxed physiological state[112].

This makes SDNN a useful non-invasive marker for assessing the relaxation or stress-modulating potential of auditory entrainment protocols.

- **Root Mean Square of the Successive Differences(RMSSD)**

  The Root Mean Square of the Successive Differences (RMSSD) is a widely used time-domain measure of Heart Rate Variability (HRV).
  It captures the short-term variability in beat-to-beat intervals and is considered a reliable index of parasympathetic (vagal) activity[113].

  The RMSSD is calculated as follows:

$$\text{RMSSD} = \sqrt{\frac{1}{N-1}\sum_{i=1}^{N-1}\left(\text{RR}_{i+1} - \text{RR}_i\right)^2} \tag{4.31}$$

  In this equation:
  RR_i represents the duration (in milliseconds) of the i-th normal beat-to-beat (NN) interval, and
  N is the number of valid RR intervals in the recording window.

  Unlike SDNN, which reflects both sympathetic and parasympathetic influences, RMSSD is more sensitive to vagally mediated changes in heart rate.

  Exposure to binaural beats in low-frequency ranges, such as alpha (7–13 Hz) or theta (4–7 Hz), has been associated with increased RMSSD values in several studies[112].
  This suggests enhanced parasympathetic tone and supports the use of BBs for stress reduction, relaxation, or meditation support.
  RMSSD is especially useful in short-term recordings and is less influenced by slow trends or respiration rates.

- **Coefficient of Variation of RR intervals (CVRR)**

  The Coefficient of Variation of RR intervals (CVRR) is a normalized measure of heart rate variability that reflects the relative dispersion of RR intervals around their mean.
  It is calculated as the ratio between the standard deviation of NN intervals (SDNN) and the mean RR interval:

$$\text{CVRR} = \frac{\text{SDNN}}{\overline{\text{RR}}} \tag{4.32}$$

In this equation:
SDNN is the standard deviation of normal-to-normal (NN) intervals, as defined in classical HRV analysis.
$\overline{RR}$ is the mean duration of RR intervals over the analysis window.
CVRR is dimensionless and often expressed as a percentage. It allows for inter-individual comparisons by removing the dependency on absolute heart rate values.

The CVRR provides insight into autonomic regulation of cardiac rhythm, and higher values typically reflect more flexible, adaptive physiological states.
In the context of binaural beat stimulation, particularly in the alpha and theta frequency bands, increased CVRR has been interpreted as a marker of parasympathetic activation and emotional regulation[114].
Due to its normalization, CVRR is particularly useful when comparing across individuals with different baseline heart rates or in longitudinal designs.

4.5 Feature Selection

For each individual subject, the initial feature set was defined by considering all measured variable indices. Experiments were conducted to reduce the feature set to 10% of the original dimensionality.
Next, until each target was reached, the following iterative procedure was applied:

- A linear SVM classifier was trained on the subject's current dataset.
- The feature weight vector from the model was extracted as a measure of each feature's importance in defining the separating hyperplane.
- The weight vector was sorted in ascending order, and in each iteration a small block of the least influential features was removed, gradually eliminating only those with the lowest discriminative contribution.

This Support Vector Machine–Recursive Feature Elimination approach was chosen for its effective balance between predictive accuracy and dimensionality reduction, ensuring robust and stable variable selection while minimizing the risk of overfitting. Finally, once the number of features fell below the predefined threshold, the final subset of indices corresponding to the most informative features for the classification task was obtained for each subject.

4.6 Model Training

For each subject, using their individual pre-selected feature set, two classifiers were trained: a Support Vector Machine (SVM) with an RBF kernel and a Random Forest. First, the 40 segments from both the sham and BBs conditions were merged, and any outliers were interpolated. This procedure was applied consistently for both Test 1 and Test 2. The full dataset (Test 1 + Test 2) was randomly divided into five segment-based folds, with a balanced representation of sham and BBs classes. This partitioning held out entire segments in each fold to avoid temporal dependence and ensure independent validation. Within each fold, the training data were normalized with min–max scaling (and the same transformation applied to the held-out segments), and only the subject-specific features were retained.

For the SVM classifier, hyperparameters C and γ were tuned via an exhaustive grid search over logarithmically spaced values from 10^{-2} to 10^{2}, evaluated through an internal three-fold cross-validation on the training portion to find the combination that maximized accuracy. The chosen SVM model was then retrained on the full training fold and tested on the held-out segments to calculate accuracy, build the confusion matrix, and list misclassified segments. Additionally, point-by-point predictions were recorded across the time series to assess the classifier's temporal discrimination ability.

For the Random Forest classifier, a model tuning process was performed to identify optimal hyperparameters. Specifically, combinations of the number of trees (`NumTrees` = [50, 100, 200]) and the minimum leaf size (`MinLeafSize` = [1, 5, 10]) were evaluated using out-of-bag (OOB) predictions to estimate training accuracy without the need for additional validation splits. The best-performing configuration was then used to train the final model using bootstrap aggregation. This tuned model was subsequently evaluated on the held-out segments by computing accuracy, generating a confusion matrix, and identifying misclassified segments. As with the SVM, point-by-point predictions were also recorded to assess temporal discrimination.

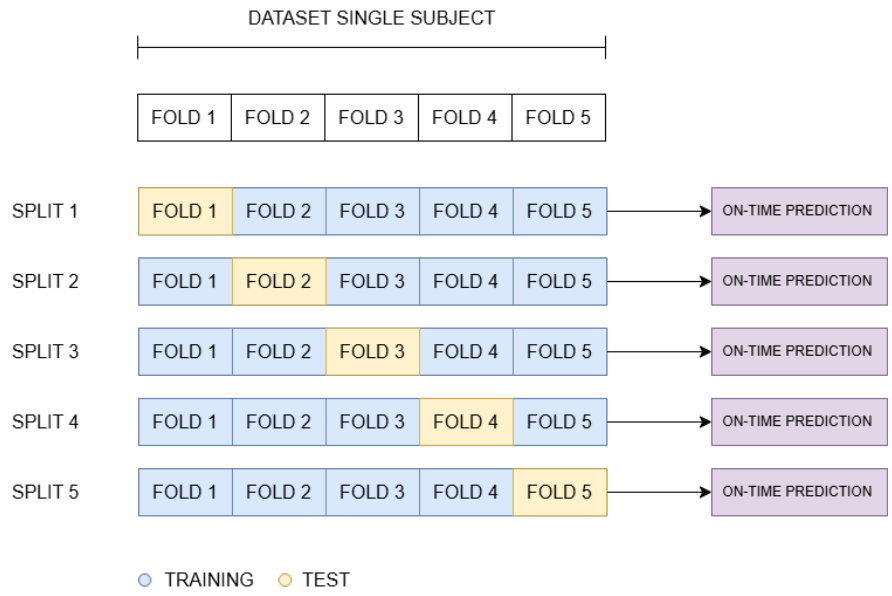

Figure 4.23: K-fold used to evaluate classificators' performances.

Finally, averaging these results across all five folds provided robust estimates of each classifier's ability to distinguish between the two experimental conditions.

4.7 Statistical Analysis: Sham vs BBs Comparison

To assess the significance of the differences between the Sham and Binaural Beats (BBs) conditions across the full experimental duration, a subject-specific statistical analysis was performed by aggregating data from both sessions (Test 1 and Test 2). For each subject, the three most informative features were selected based on prior feature selection rankings, ensuring that the most relevant descriptors of the individual's neurophysiological response were used in the analysis.

For each selected feature, all available segments (four 15-second windows per block, across five blocks and two sessions) were grouped by condition (Sham or BBs), resulting in up to 20 paired samples per feature and condition. The Wilcoxon signed-rank test was then applied to compare the two conditions, as it is a non-parametric test suitable for dependent samples without assuming normality. The test statistic is defined as:

$$W = \sum_{i=1}^{n} \text{sgn}(x_i - y_i) \cdot R_i \tag{4.33}$$

where x_i and y_i are the paired observations under the two conditions (e.g., Sham and BBs), R_i is the rank of the absolute difference $|x_i - y_i|$ among all non-zero differences, and $\text{sgn}(x_i - y_i)$ denotes the sign function.

This approach allowed us to statistically evaluate whether the most discriminative features showed consistent and significant differences between stimulation types across the entire protocol, while respecting the heterogeneity of individual subject responses.

Chapter 5

Results and Discussion

This chapter presents and discusses the results obtained from the protocol by analysing the collected data. The main objective is to identify the effect of brief, repeated stimulation with BBs, using the subjects' physiological parameters as a reference. An effort is made to shed light on the effects generated by binaural beats using pure alpha-band tones and their potential relaxing benefits, considering that the existing literature shows great heterogeneity in both the results obtained and the application of BBs.

The analysis will begin with the differences recorded between individual subjects and will then focus on the on-time predictions produced by the selected classifiers. The aim is to provide both a general overview of the presence and nature of the effect and to understand how the stimulation may be perceived differently by each subject, sometimes leading to very diverse outcomes.

5.1 Selected Features

Feature selection plays a crucial role in problems involving classifiers, as it is essential to reduce the number of features considered in order to mitigate issues such as redundancy, low representativeness, and overfitting.

Following a series of evaluations, Recursive Feature Elimination (RFE) was selected— as previously mentioned in Section 4.5 — to reduce the number of features per subject to 10% of the total, resulting in 15 selected features out of 148.

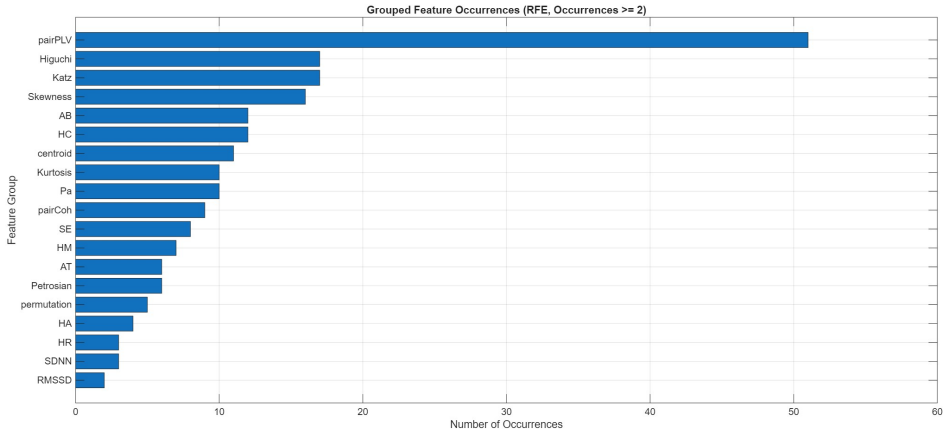

Figure 5.1: Most frequently selected features across all subjects (without distinguishing channels).

In Figure 5.1, it can be seen that, when considering the features most frequently selected across all subjects (without distinguishing individual channels), the PLV stands out with the highest number of occurrences (51). This is likely due to two main reasons: first, PLV is inherently overrepresented since it involves combinations across all available EEG channels; second, and more importantly, it reflects inter-regional brain synchronization, a phenomenon frequently associated with the effects of binaural beats in the literature. Indeed, previous studies such as [75] have shown how BBs can influence neural synchrony, supporting the interpretation that such high selection frequency reinforces the presence of a tangible neural effect even under short stimulation durations.

Fractal dimension metrics such as Higuchi and Katz were also prominently selected, with 17 occurrences both. This aligns with expectations, as both features are well-established indicators of EEG signal complexity. Their recurrent selection adds weight to the hypothesis of a meaningful modulation of the EEG trace induced by BB stimulation, suggesting changes in the nonlinear dynamics of the signal.

Features like AB (α/β power ratio), AT (α/θ power ratio), and Centroid are directly related to the spectral content of the EEG and its shifts across frequency bands. These metrics are crucial when investigating possible alterations in power distribution, particularly under the hypothesis of brain entrainment or modulation via auditory stimuli. Their relevance among the selected features confirms that detectable changes in the power spectrum occurred during the protocol.

Regarding ECG-derived metrics, 3 out of the 4 features considered were selected

(HR, SDNN, RMSSD, leaving out CVRR), although with a markedly lower frequency (up to 3 occurrences). This is most likely due to their single-channel nature, resulting in fewer candidate features overall. Nevertheless, their presence among the selected set suggests a certain degree of discriminative power, highlighting a possible secondary effect of BB stimulation on cardiac autonomic regulation.

Finally, the Hjorth parameters (HA, HC, and HM) were also selected multiple times, particularly HC, which appeared 12 times. This indicates that the complexity and structural characteristics of the EEG signal, as captured by time-domain descriptors, were affected by the experimental conditions, further supporting the hypothesis of BB-induced modulations.

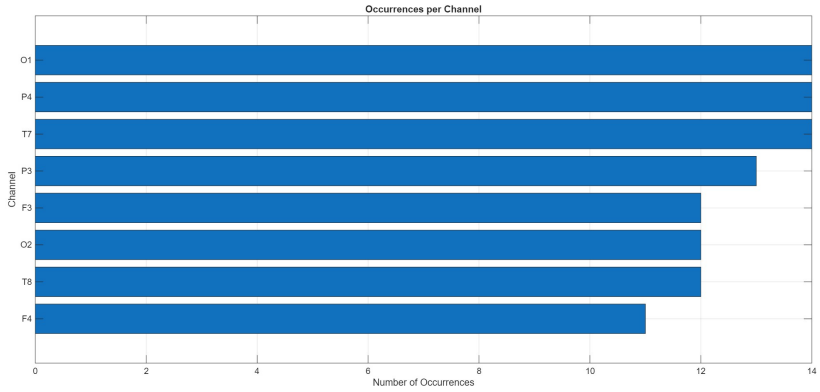

Figure 5.2: Number of selected features per channel.

Figure 5.2 shows the number of features selected during the feature selection phase, grouped by EEG channel. As can be observed, there is a high degree of homogeneity across the different channels. The most frequently selected channels are O1, P4, and T7, each with 14 occurrences, while the least selected channel is F4, with 11 occurrences. This relatively uniform distribution is somewhat unexpected, considering that the literature typically reports a stronger involvement of parietal areas (P3 and P4) and occipital areas (O1 and O2) during alpha-band stimulation[115].

The observed results suggest that the effect produced by binaural beats may not be limited to the areas typically associated with alpha-band activity—such as occipital and parietal regions, as commonly reported in the literature—but instead appears to involve a broader and more distributed network of cortical regions. This finding indicates that the neural modulation induced by the stimulation could extend beyond localized effects, potentially engaging more widespread brain dynamics (see also Figure 4.18).

5.2 On-time Predictor

While distinguishing between Sham and Binaural-Beat stimulation is fundamental to understanding the immediate effects of auditory entrainment on EEG patterns, the present study extended its focus beyond these static comparisons. In particular, this investigation sought to determine how repeated, alternating exposures to sham and BBs over an extended session modulate neural responsiveness and classifier discriminability over time. Given that neural entrainment may exhibit cumulative, residual, or habituation effects, it is crucial to characterize not only the binary classification performance at each block but also the temporal evolution of these effects across successive stimulations. By examining minute-by-minute and sub-block trends, the study aimed to uncover whether progressive exposure enhances the detectability of BBs-induced activity, diminishes recognition of sham blocks due to carry-over, or reveals subject-specific variations in adaptation. This temporal perspective allows for a more nuanced interpretation of how ongoing stimulation protocols interact with endogenous brain dynamics and informs the design of future neuromodulation studies.

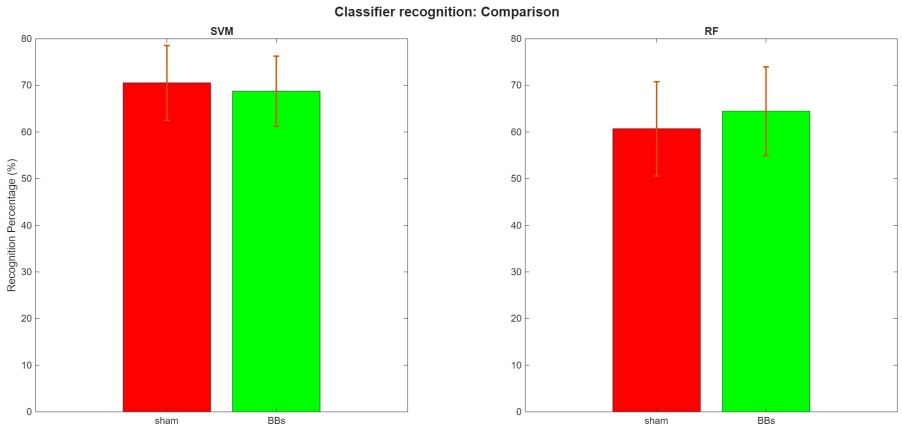

Figure 5.3: Recognition Percentage: SVM vs RF.

First, the overall performance of two classifiers—*Support Vector Machine* and *Random Forest* —was compared by computing the mean accuracy across all subjects and time points for both Test 1 and Test 2 sessions. When aggregating over the two tests, the SVM yielded a mean recognition rate for the sham condition of 70.54 % ($\pm$ 8.00 %) and for the BBs stimulation of 68.75 % ($\pm$ 7.54 %), whereas the RF achieved 60.71 % ($\pm$ 10.10 %) for sham and 64.46 % ($\pm$ 9.50 %) for BBs. Not only

does the SVM exhibit a higher overall average accuracy, but it also demonstrates a lower standard deviation across both conditions—indicative of greater classification stability. As illustrated in Figure 5.3, these differences underscore the SVM's superior balance of sensitivity and reliability in discriminating between sham and Binaural-Beat blocks across participants and sessions. Therefore, the SVM classifier was selected for further, more in-depth analysis, and the Random Forest approach was set aside.

Next, the classifier's minute-by-minute accuracy was examined separately for Test 1 and Test 2 by averaging each subject's performance at each one-minute interval (Figure 5.4).
The accuracy at each minute was computed by averaging the classifier's predictions over four consecutive 15-second blocks, and subsequently averaged across all subjects.

In Test 1, sham accuracy declined from $85.71\% \pm 10.10\%$ (block 1) to $69.64\% \pm 20.52\%$ (block 5), while BBs recognition increased from $57.14\% \pm 8.25\%$ (block 1) to $71.43\% \pm 15.43\%$ (block 5). This divergence likely reflects a combination of factors: during the first sham block, participants were responding to very distinct, unmodulated stimuli, yielding crisp, near-ceiling performance, whereas the initial entrainment to the binaural beats was still nascent and did not yet produce a robust neural signature. As the session progressed, however, repeated exposure to the BBs led to a gradual strengthening of alpha-band synchrony, producing more pronounced phase-locking and clearer perceptual differentiation of BBs stimuli. Simultaneously, these accumulating entrainment effects persisted into subsequent sham blocks, subtly biasing neural processing and thereby attenuating sensitivity to the now relatively unmodulated sham trials.

In Test 2, sham accuracy was $66.07\% \pm 10.71\%$ in block 1, whereas BBs recognition rose from $58.92\% \pm 12.20\%$ (block 1) to $82.14\% \pm 7.14\%$ (block 5), following a similar upward trend as observed in Test 1. The lower initial sham performance here suggests that the inter-test rest interval may have been insufficient to fully dissipate residual entrainment from the first BBs exposure. Consequently, lingering alpha-band resonance likely persisted into the start of Test 2, both depressing early sham detection by reducing the contrast between sham and BBs neural signatures, and simultaneously sharpening the fidelity of BBs-specific patterns. Over successive BBs blocks, these residual effects would compound with new entrainment, yielding the robust increase in BBs discriminability noted across the session.

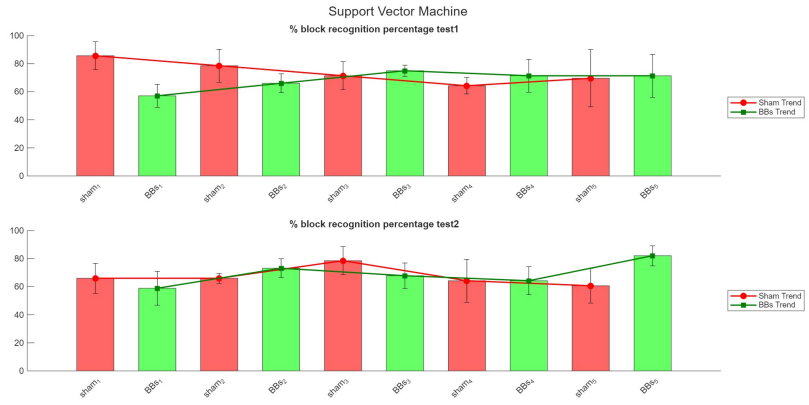

Figure 5.4: Minute-by-minute recognition accuracy for sham and BBs conditions in Test 1 and Test 2 (averaged across all subjects).

Classifier accuracy within each stimulus block was then investigated at 15-second resolution (Figure 5.5) to detect transient carry-over effects at block transitions: in both tests, the very first 15-s bin of a new block often showed a marked drop in recognition (e.g. $\text{sham}_1 \rightarrow \text{BBs}_1$, $\text{BBs}_2 \rightarrow \text{sham}_3$ in Test 1; $\text{sham}_3 \rightarrow \text{BBs}_3$, $\text{sham}_4 \rightarrow \text{BBs}_4$ in Test 2), consistent with residual activity from the preceding condition. Following these initial drops, performance typically rebounds within the next 15–30 seconds, reflecting a rapid recovery phase during which classifier performance re-stabilizes. This intra-block recovery may indicate the gradual dissipation of residual neural activity, an adaptive shift in attentional focus, or classifier recalibration. Quantitative analysis of this recovery trajectory—possibly through fitting an exponential decay or linear model—could help determine whether recovery rates differ systematically between conditions (sham vs. BBs) or between individuals. Furthermore, some internal-block anomalies (e.g. the second sham block of Test 1 and the third sham block of Test 2) warrant subject-specific investigation to discern if individual variations in susceptibility, fatigue, learning effects, or attentional states contribute to these deviations. This deeper exploration may facilitate more nuanced interpretations and enhance the robustness of conclusions drawn from classifier performance across experimental blocks.

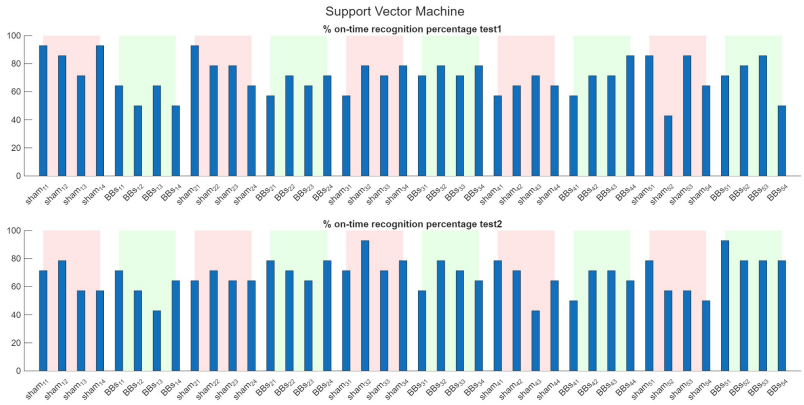

Figure 5.5: 15-second bin recognition accuracy at block transitions for Test 1 and Test 2.

Finally, the time courses of the subject with the highest overall recognition accuracy (Subject 12, 75% for Test 1 and 87.5% for Test 2) and of the subject with the lowest accuracy (Subject 2, 62.5% fo Test 1 and 55% for Test 2) are highlighted to illustrate the pronounced heterogeneity of EEG responses to the alternating sham and BBs protocols.

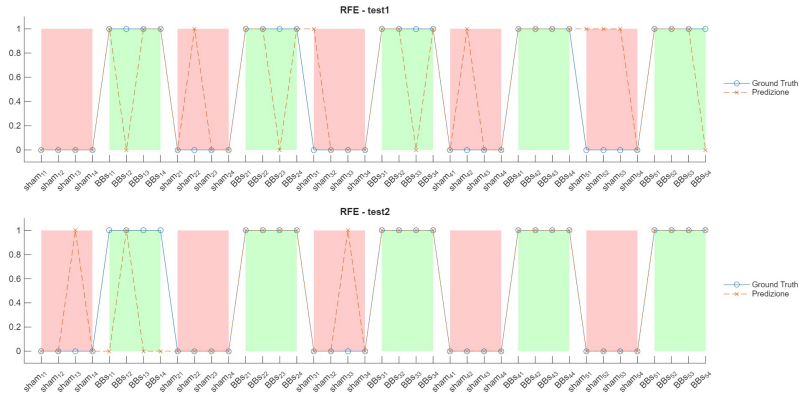

Figure 5.6: Recognition time-course for the subject with highest overall accuracy (subject 12).

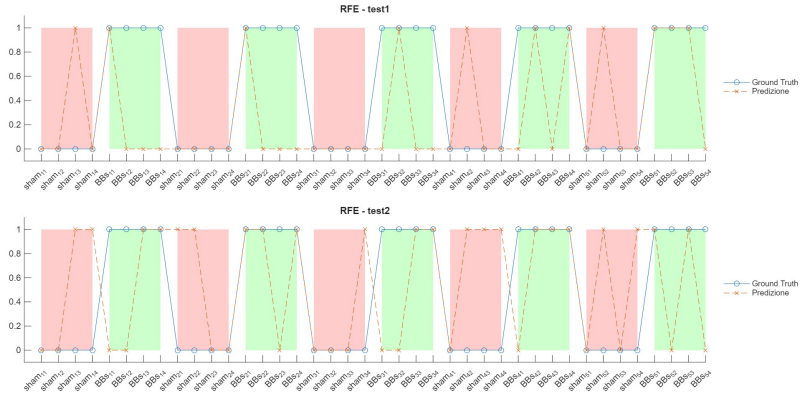

Figure 5.7: Recognition time-course for the subject with lowest overall accuracy (subject 2).

5.3 Inter-Subject Feature Comparison

This section focuses on the analysis of features obtained under sham and BBs conditions across different subjects. The aim is to investigate whether consistent effects can be identified despite inter-subject variability, and whether specific features are able to reflect a shared neural or physiological response to the stimulation.

By comparing the distribution of features between conditions, the analysis seeks to highlight distinguishing elements that may indicate the presence of a systematic effect induced by binaural beats. Particular attention is given not only to individual variability, but also to the potential emergence of condition-specific trends that are recurrent across subjects. This approach allows for a broader evaluation of how generalizable the observed responses are, and whether they align with findings reported in previous studies.
The features shown in this section are selected among those used to train the classifiers on a single-subject basis, ensuring that the analysis focuses on the most relevant and informative variables for distinguishing between conditions.

5.3.1 Neural Synchronization and Spectral Coherence

Overall, the boxplots reveal a general trend of increased synchronization between brain regions when subjects are exposed to BBs, compared to the sham condition. This increase is especially evident in adjacent cortical areas.

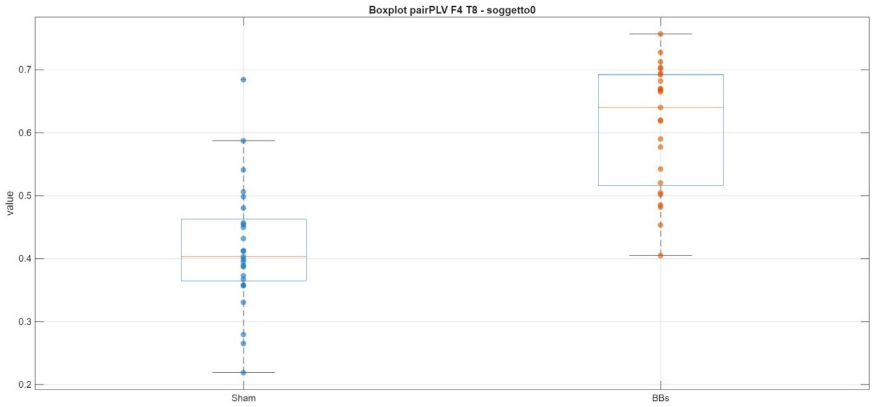

Figure 5.8: PLV between F4 and T8 for Subject 0.

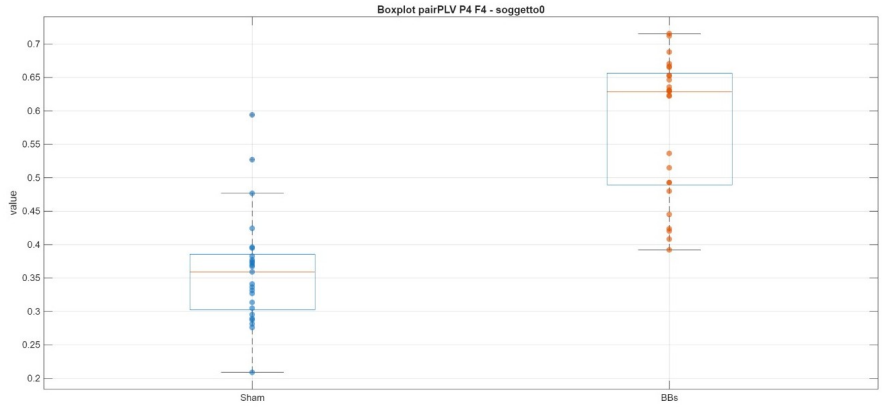

Figure 5.9: PLV between P4 and F4 for Subject 0.

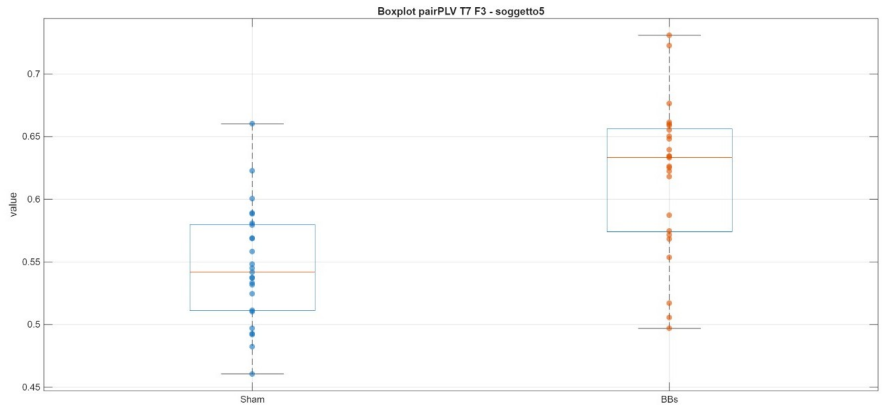

Figure 5.10: PLV between T7 and F3 for Subject 5.

For instance, in subject 0, significant enhancements in phase locking are observed between the pairs P4–F4 and F4–T8. A similar local increase is noted in subject 5 between T7 and F3. These results suggest that BB stimulation may effectively facilitate local neural entrainment (Figures 5.8, 5.9 and 5.10).

In particular, subjects 9 and 12 show notable increases in synchronization between homologous regions across hemispheres, especially in the F3–F4 pair (Figures 5.11 and 5.12). This cross-hemispheric enhancement supports the hypothesis that BB stimulation may promote the spreading of synchronized activity across wider cortical areas. Such findings are consistent with the idea that the brain, under BB exposure, tends to synchronize its rhythmic activity across multiple regions, leading to a broader entrainment effect.

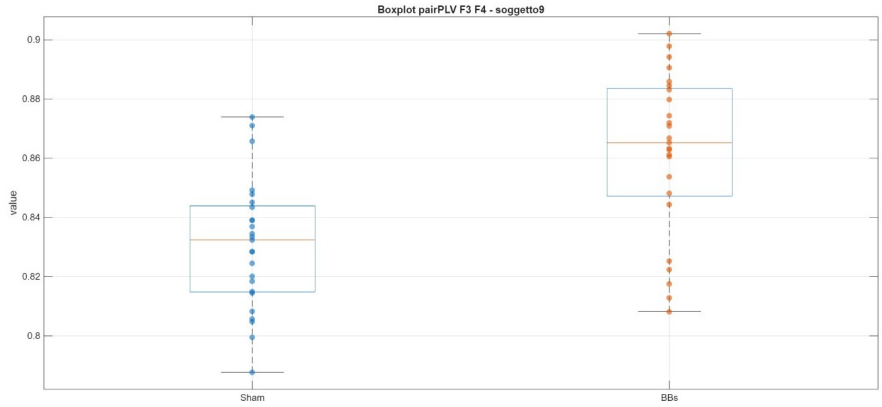

Figure 5.11: PLV between F3 and F4 for Subject 9.

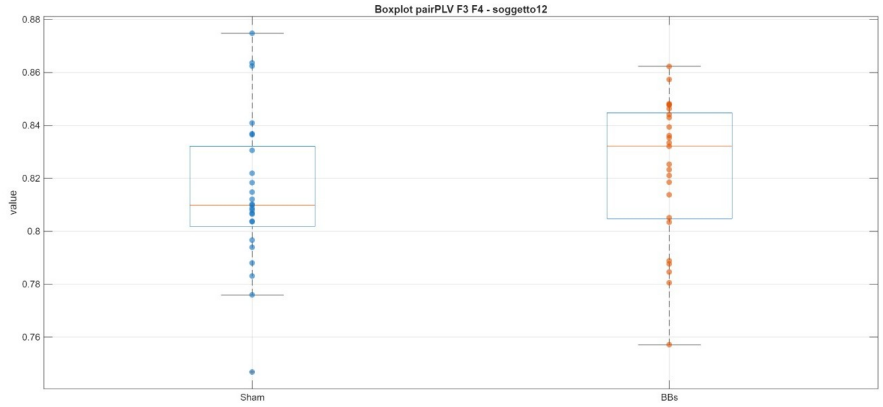

Figure 5.12: PLV between F3 and F4 for Subject 12.

Interestingly, in subject 12, an elevated synchronization is also observed between distant regions, such as T7–P4, suggesting that the effect of BBs may not be limited to anatomically adjacent areas. This could point to a more global mechanism of functional connectivity modulation, potentially involving large-scale brain networks (Figure 5.13).

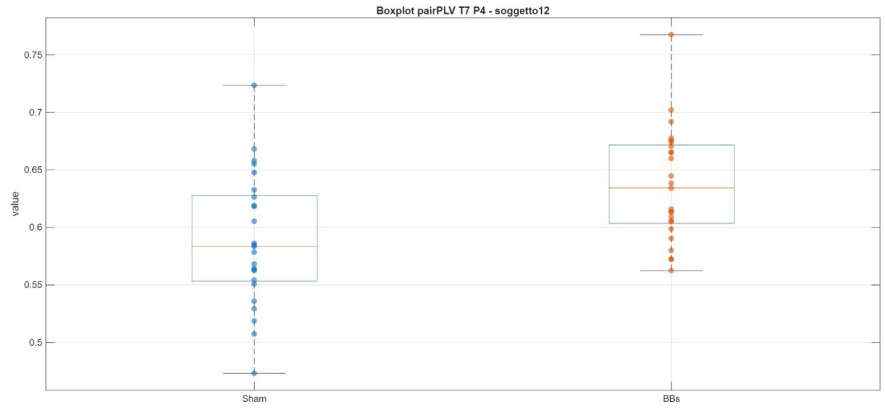

Figure 5.13: PLV between T7 and P4 for Subject 12.

However, not all observations align with this expected pattern (Figures 5.14 and 5.15). Subject 3, who was later identified as one of the least responsive individuals in terms of distinguishing between conditions, shows a clear decrease in synchronization for both F3–F4 and T7–P3. This behavior starkly contrasts with the rest of the cohort, further underlining the variability in individual responses to BB stimulation.

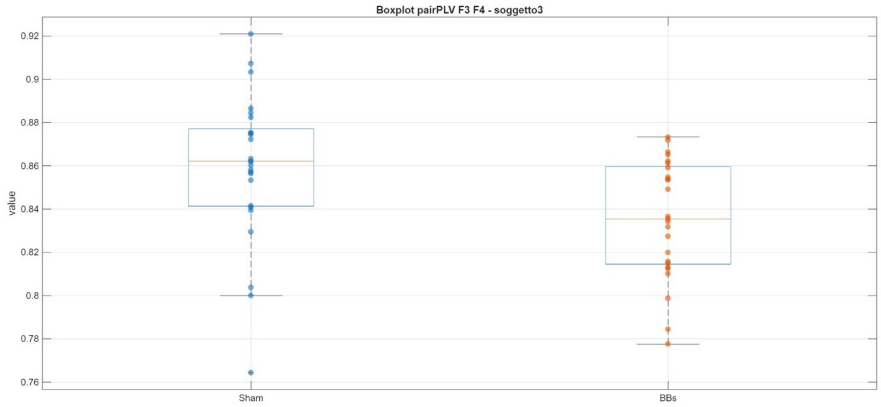

Figure 5.14: PLV between F3 and F4 for Subject 3.

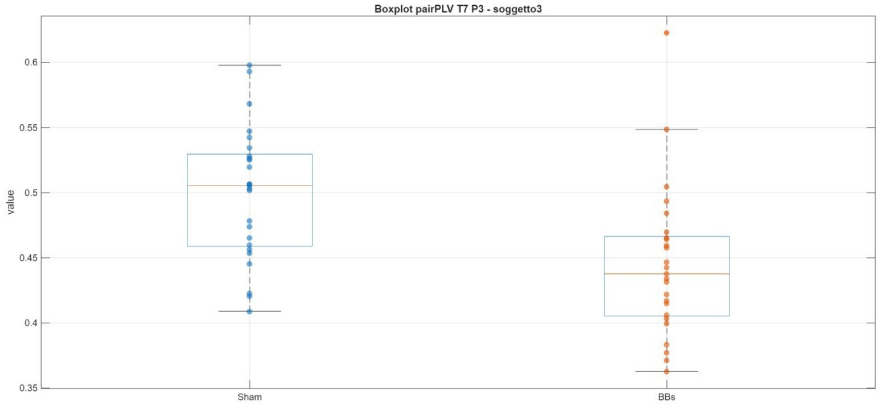

Figure 5.15: PLV between T7 and P3 for Subject 3.

With regard to spectral coherence, although it was considered a secondary feature for discriminating between conditions, some informative patterns emerge. Subject 9 shows an increase in coherence between F3–F4 under BB stimulation (Figure 5.16), while subject 3 displays a decrease for the same channel pair (Figure 5.17). This dichotomy highlights the subject-dependent nature of the BB effect and suggests that spectral coherence, although less consistent, may still provide valuable complementary insights into the dynamics of brain response to auditory entrainment.

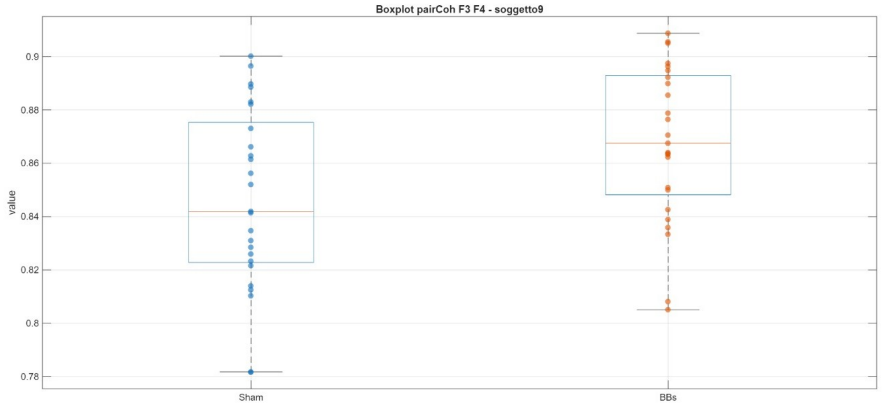

Figure 5.16: Spectral Coherence between F3 and F4 for Subject 9.

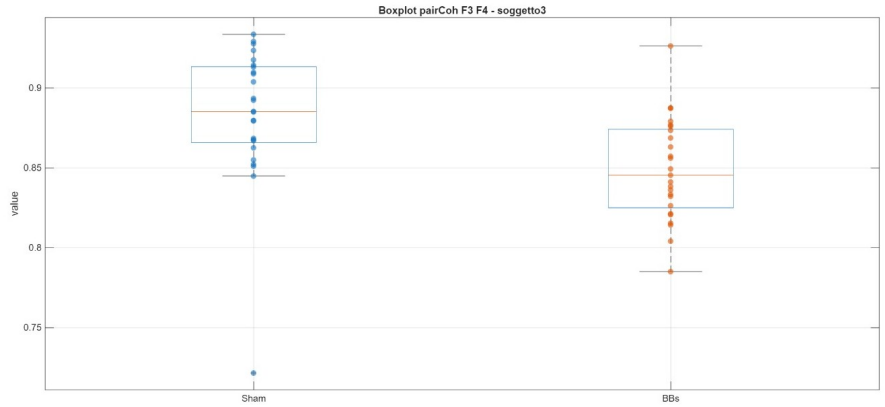

Figure 5.17: Spectral Coherence between F3 and F4 for Subject 3.

5.3.2 Fractal Dimension Analysis

Overall, across subjects and recording sites, both Higuchi's and Katz's fractal dimensions exhibited a consistent reduction under BBs stimulation compared to the sham condition. This decrease in fractal dimension was an anticipated finding, given that alpha-band entrainment by BBs is expected to drive the EEG signal toward a more regular, sinusoid-like waveform—and thus reduce its intrinsic complexity.

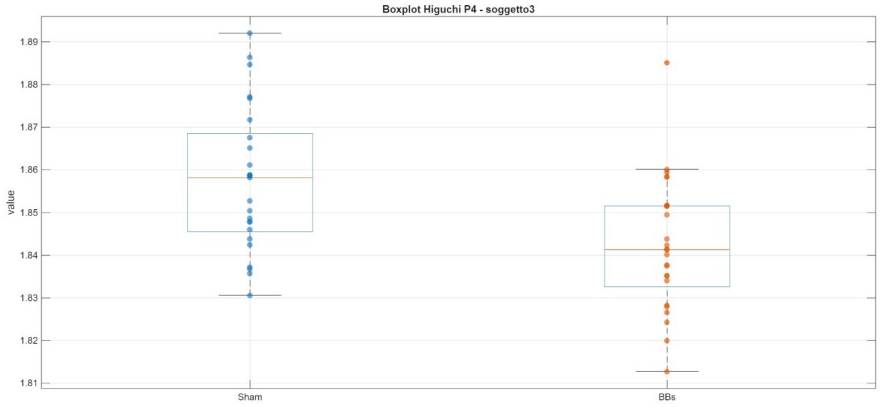

Figure 5.18: Higuchi P4 subject3 .

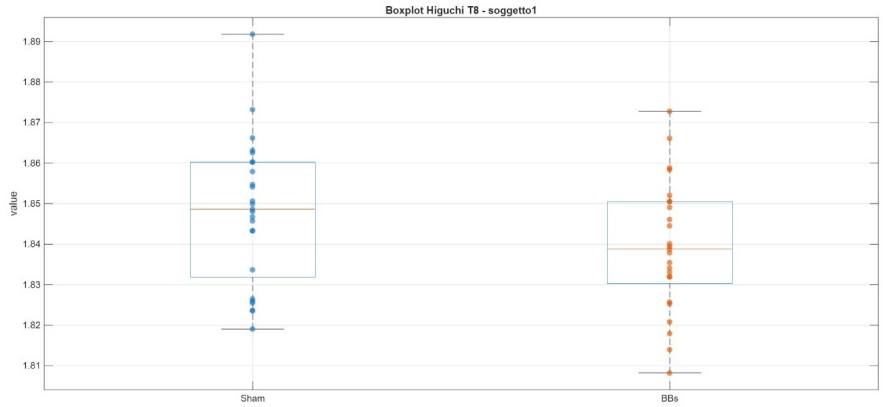

Figure 5.19: Higuchi T8 subject1.

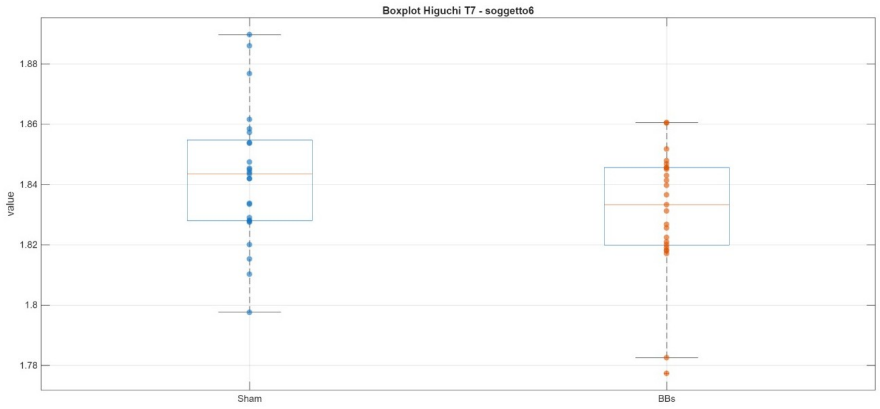

Figure 5.20: Higuchi T7 subject6.

Focusing first on Higuchi's dimension, the decline was observed in multiple cortical areas, suggesting a globally distributed effect of rhythmic BBs stimulation. For example, subject 1 showed a clear decrease at electrode T8 (Figure 5.19), subject 3 at P4 (Figure 5.18), and subject 6 at T7 (Figure 5.20). These reductions point to a widespread simplification of signal structure when the brain is coerced into its individual alpha rhythm. Nevertheless, not every individual conformed to this pattern: subject 0 at P3 (Figure 5.21) and subject 2 at O1 (Figure 5.22) actually displayed a slight increase in Higuchi dimension under BBs. Such exceptions likely reflect inter-individual variability in responsiveness to external rhythmic driving, perhaps related to baseline alpha power or phase-locking propensity.

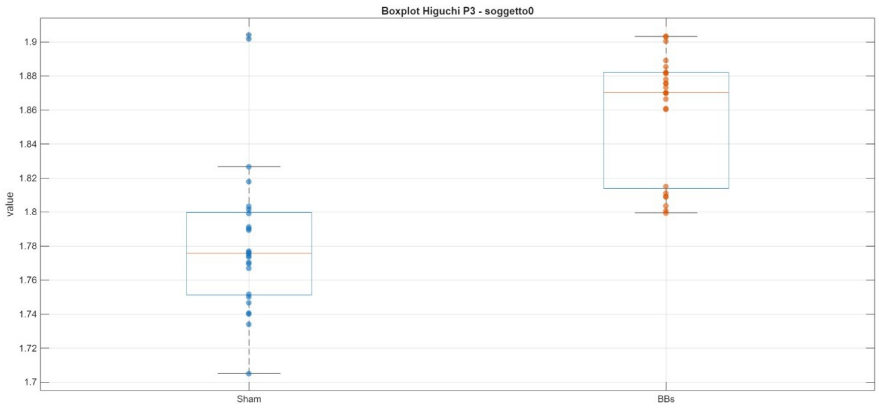

Figure 5.21: Higuchi P3 subject0.

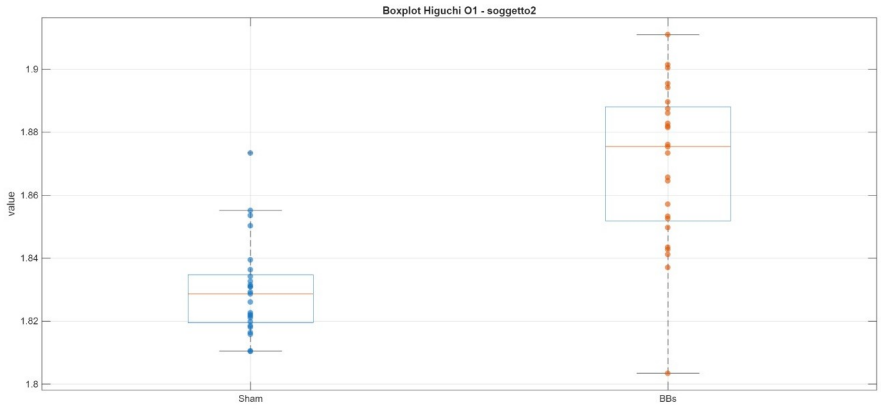

Figure 5.22: Higuchi O1 subject2.

A parallel picture emerged for Katz's dimension: most subjects again showed lower fractal dimensionality under BBs, implying a more stereotyped waveform

shape. Notably, subject 1 at T7 (Figure 5.23), subject 6 at O1 (Figure 5.24), and subject 12 at P3 (Figure 5.25) all exhibited this effect. Taken together, these results support the hypothesis that alpha-frequency BBs stimulation reduces the complexity of spontaneous EEG activity across widespread cortical regions—while also highlighting the importance of individual differences in neurophysiological entrainment.

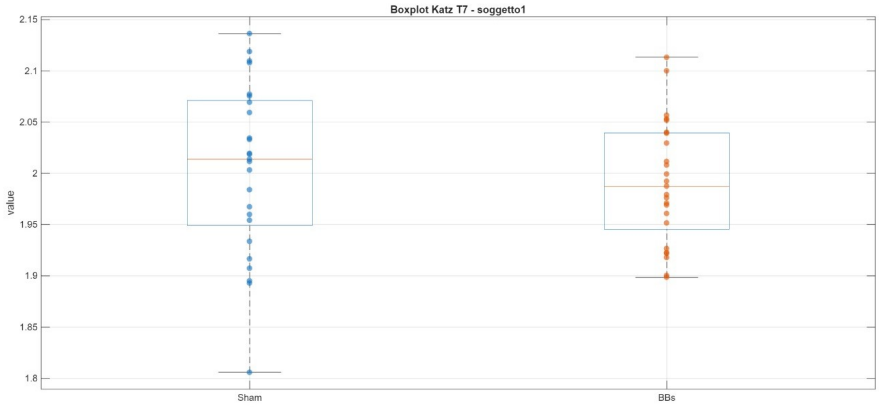

Figure 5.23: Katz T7 subject1.

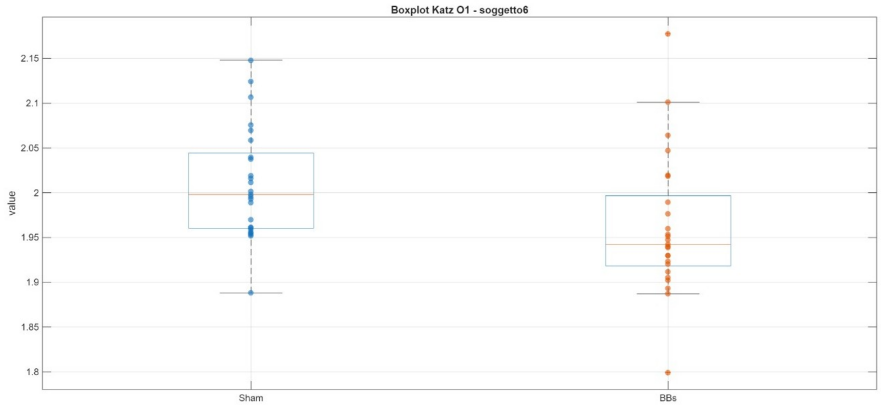

Figure 5.24: Katz O1 subject6.

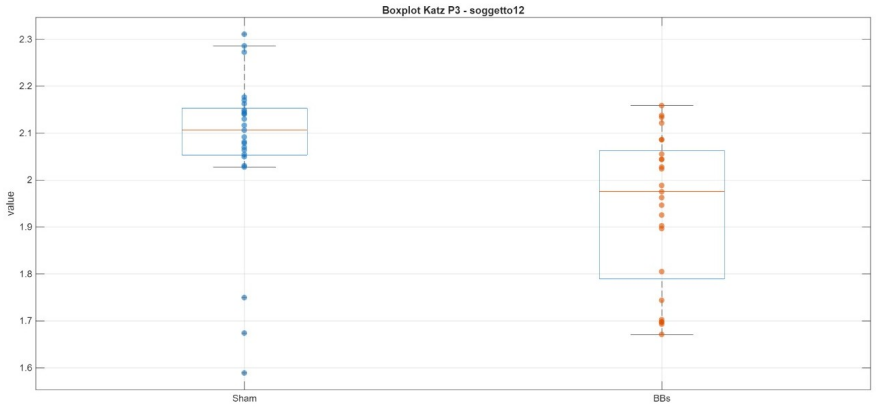

Figure 5.25: Katz P3 subject12.

5.3.3 Spectral Analysis

In the context of spectral analysis, we focused on three EEG features: the α/β power ratio (AB), the α/θ power ratio (AT), and the spectral centroid, defined as the power-weighted mean frequency. These measures help characterize brain states linked to arousal, relaxation, and attention.

When comparing the same cerebral areas across different subjects, we observed a consistent increase in the AB ratio in region F4 for subjects 3 and 14 (Figures 5.26 and 5.27), as well as in region O1 for subjects 8 and 10 (Figures 5.28 and 5.29). This increase is indicative of a spectral shift toward the alpha band, characterized by a significant enhancement of alpha power accompanied by a corresponding reduction in beta activity. Such a pattern is typically associated with a relaxed mental state, suggesting that the auditory stimulation may have induced a generalized relaxation response.

A similar phenomenon is evident in subject 0 in region P4, reinforcing the idea of a distributed effect spanning multiple cortical regions (Figure 5.30).

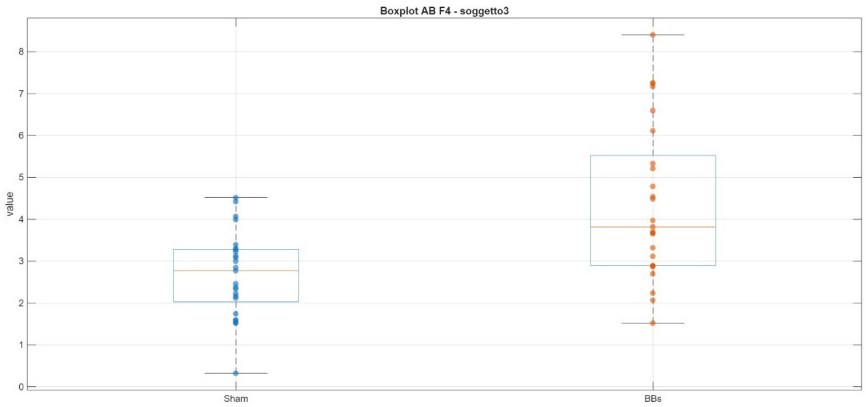

Figure 5.26: α/β power ratio F4 subject 3.

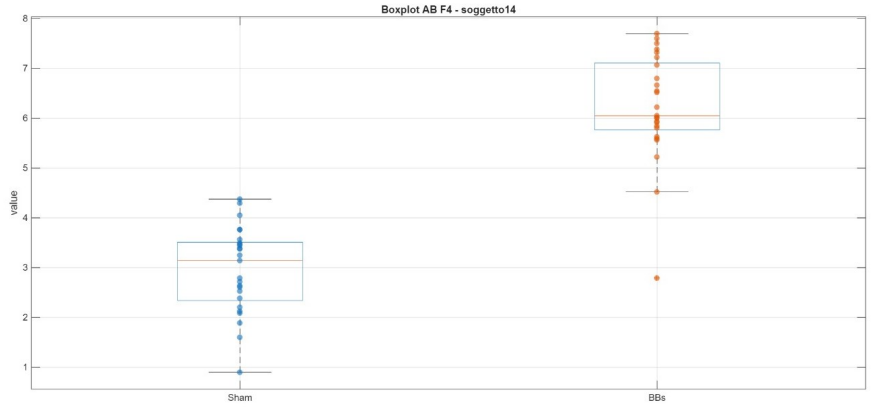

Figure 5.27: α/β power ratio F4 subject 14.

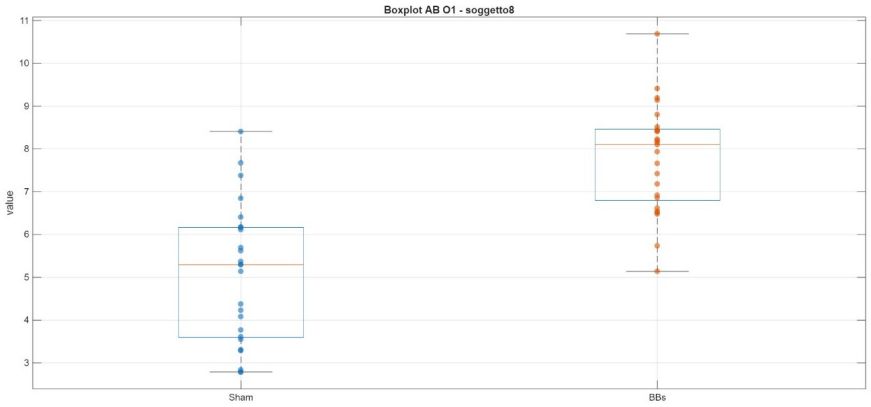

Figure 5.28: α/β power ratio O1 subject 8.

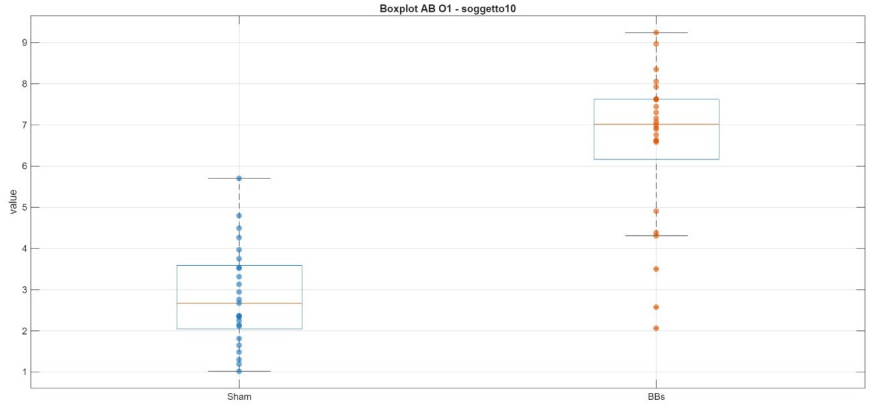

Figure 5.29: α/β power ratio O1 subject 10.

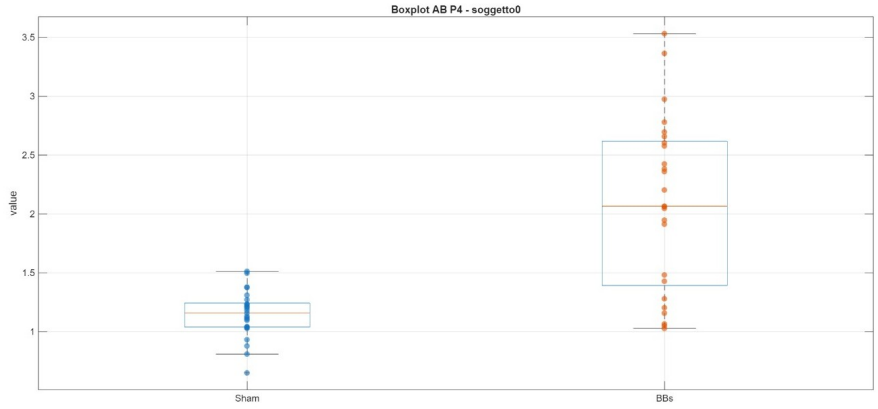

Figure 5.30: α/β power ratio P4 subject 0.

Analysis of the alpha/theta ratio revealed a more heterogeneous pattern. Specifically, subject 1 showed an increased AT ratio in region O2 (Figure 5.31), while subject 4 exhibited a marked decrease in the same region (Figure 5.32). This divergence highlights inter-subject variability, with opposing trends emerging within the same cortical area. A plausible interpretation is that subject 4 may have experienced a further reduction in cortical activity, with spectral energy shifting toward the theta band — a hallmark of deep relaxation or even drowsiness.

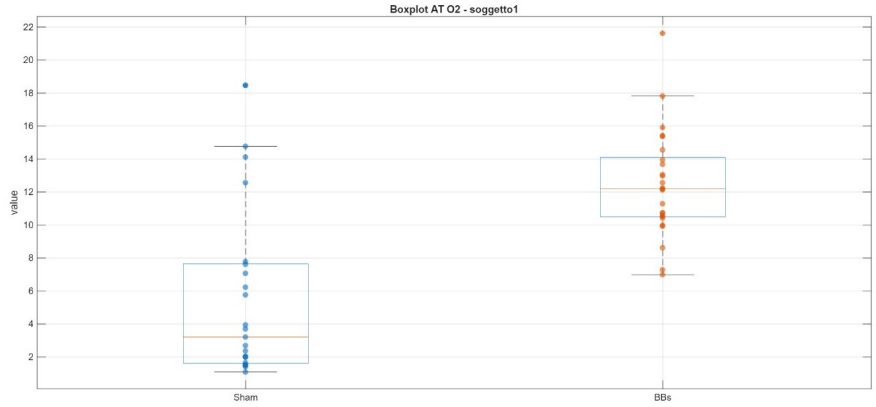

Figure 5.31: Increase of α/θ power ratio O2 subject 1.

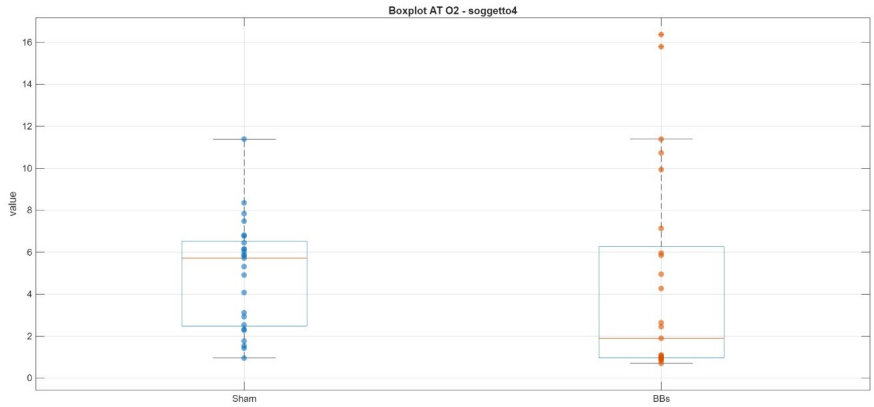

Figure 5.32: Decrease of α/θ power ratio O2 subject 4.

However, the most compelling findings pertain to the behavior of the spectral centroid. As illustrated in the figures, subjects 1 and 10 — in regions O1 and T8, respectively — exhibit a narrowing of the spectral distribution toward lower frequencies (Figures 5.33 and 5.34). Notably, the centroid values converge around the subjects' Individual Alpha Frequency (IAF), with subject 1 displaying an IAF of 10.26 Hz and subject 10 an IAF of 9.69 Hz. This observation strongly suggests a frequency-locking effect, whereby brain activity becomes increasingly aligned with the externally imposed stimulation frequency. Among all metrics, this shift in the spectral centroid provides the most robust evidence for entrainment, underscoring the capacity of rhythmic auditory stimulation to modulate ongoing neural oscillatory dynamics in a frequency-specific manner.

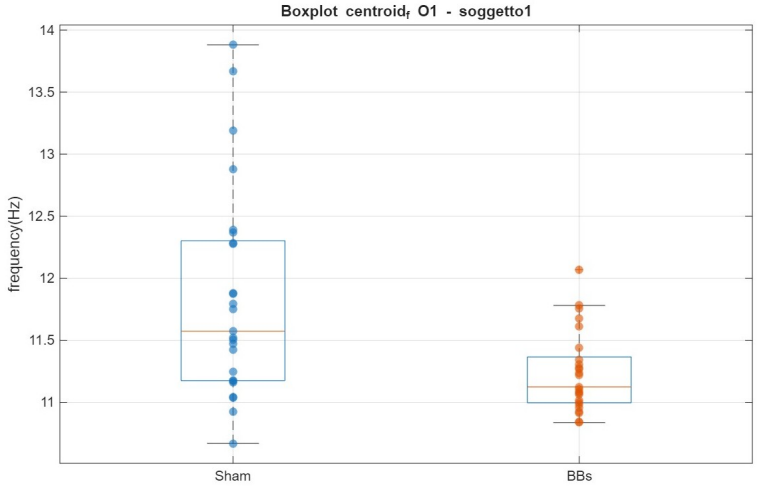

Figure 5.33: Centroid O1 subject 1.

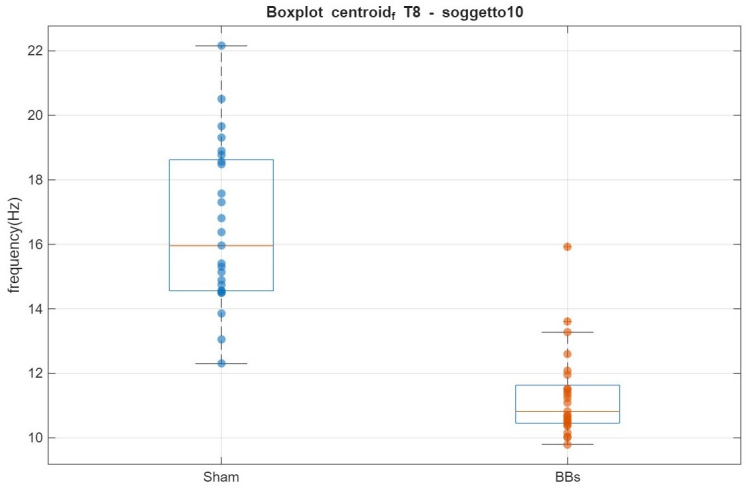

Figure 5.34: Centroid T8 subject 10.

5.3.4 Heart Rate Analysis

Among the ECG-derived features selected during the feature selection process, heart rate (HR) emerged as the most significant. As illustrated in the boxplots, both Subject 10 and Subject 13 exhibited a clear reduction in HR during the binaural beats (BBs) stimulation phase compared to the sham condition. Specifically, Subject 10 showed a decrease from approximately 70 bpm to 67 bpm (Figure 5.35), while Subject 13's HR dropped from around 80 bpm to 72 bpm (Figure 5.36).

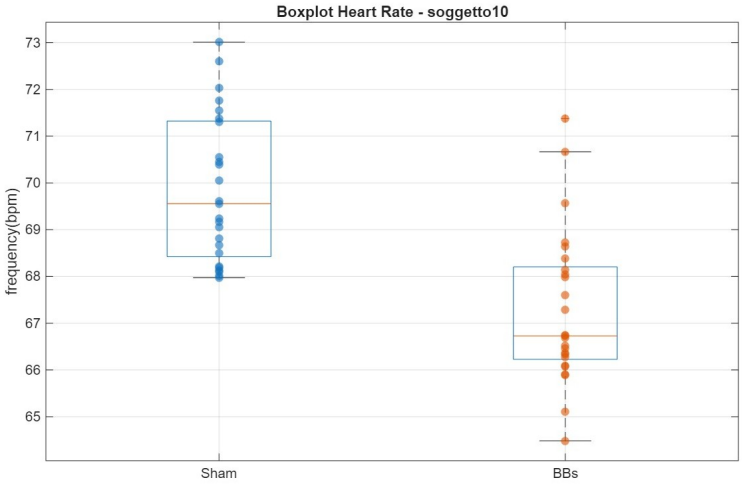

Figure 5.35: Heart rate subject 10.

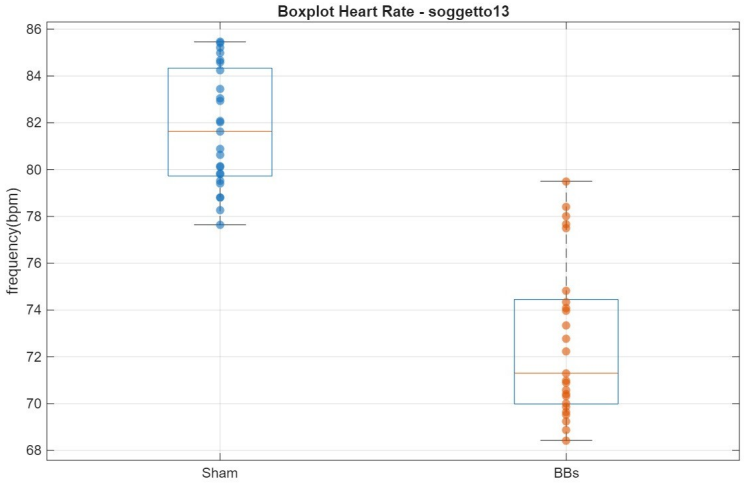

Figure 5.36: Heart rate subject 13.

These findings are particularly noteworthy as they suggest that the effects of BBs are not confined to cortical activity but extend to the autonomic nervous system, specifically influencing cardiac function. The observed reduction in heart rate is indicative of enhanced parasympathetic activation, a physiological marker commonly associated with a relaxed state. This supports the hypothesis that BBs may induce a general relaxation response, reinforcing the potential of this auditory stimulation as a modulator of both brain and cardiovascular dynamics.

5.4 Interpretation of the Wilcoxon Test Results

subject	feature	p_value	significative
0	HC_ch3	1.229e-05	yes
0	pairPLV_P4_F4	1.3898e-05	yes
0	AB_ch6	2.8639e-05	yes
1	Pa_ch4	1.229e-05	yes
1	AT_ch5	0.00023991	yes
1	SE_ch5	0.0011858	yes
2	Higuchi_ch4	6.451e-05	yes
2	Kurtosis_ch5	0.00023991	yes
2	HM_ch1	0.010181	yes
3	Higuchi_ch6	0.006848	yes
3	pairPLV_T7_P3	0.0026987	yes
3	AB_ch7	0.006848	yes
4	pairPLV_O1_F4	0.0035071	yes
4	permutation_entropy_ch3	0.051087	no
4	pairPLV_O1_O2	0.065311	no
5	HA_ch4	0.10355	no
5	pairPLV_T7_F3	0.00029577	yes
5	pairPLV_P4_T8	0.024657	yes
6	Pa_ch5	0.0022586	yes
6	Higuchi_ch1	0.011876	yes
6	Higuchi_ch3	0.0020642	yes
7	SE_ch1	0.0035071	yes
7	AB_ch4	0.45934	no
7	pairPLV_P3_P4	0.88235	no
8	SE_ch4	3.2229e-05	yes
8	AB_ch4	0.00014048	yes
8	centroid_f_ch2	0.011	yes
9	pairCoh_T7_T8	0.00040277	yes
9	pairPLV_F3_F4	0.00010105	yes
9	permutation_entropy_ch8	0.00021585	yes
10	centroid_f_ch8	1.7735e-05	yes
10	HR_mean	1.5705e-05	yes
10	AB_ch4	1.7735e-05	yes
11	AB_ch7	1.3898e-05	yes
11	HM_ch6	0.003822	yes
11	Higuchi_ch1	0.006848	yes
12	pairPLV_T7_P4	0.0094174	yes
12	centroid_f_ch5	0.0007333	yes
12	Katz_ch3	0.021418	yes
13	pairCoh_T7_T8	0.00019407	yes
13	HR_mean	1.229e-05	yes
13	HC_ch4	0.0015693	yes

Figure 5.37: Wilcoxon signed-rank test results for the top three features per subject, comparing Sham and Binaural Beats (BBs) conditions. Most subjects show statistically significant differences ($p < 0.05$), indicating distinct neurophysiological responses between conditions

The statistical analysis performed using the Wilcoxon signed-rank test revealed that, for the majority of subjects, the top three individually selected features

exhibited statistically significant differences between the Sham and BB conditions. As illustrated in Figure 5.37, nearly all subjects demonstrated at least two features with p-values well below the conventional threshold of 0.05, indicating a robust difference in neurophysiological responses across conditions. Notably, subject 4 represents a borderline case: although only one of the three features reached statistical significance, the remaining two features displayed p-values (0.051087 and 0.065311) that were very close to the 0.05 threshold, suggesting a potential underlying effect that may not have reached significance due to sample variability or individual response characteristics. Subject 7, on the other hand, showed no significant differences across the selected features. Overall, the consistency of significant results across subjects supports the hypothesis that BBs stimulation elicits measurable changes in EEG-derived features when compared to the Sham condition.

Chapter 6

Conclusion and Future Developments

6.1 Conclusion

This study has provided compelling evidence that alpha-band (7–13 Hz) auditory stimulation induces a pronounced relaxation effect, reflected in a widespread decrease in cortical activation across multiple regions. Such an outcome is particularly noteworthy given that, in much of the existing literature, alpha rhythms have been leveraged primarily to enhance concentration or memory performance—with limited or inconsistent success. Here, by contrast, alpha entrainment reliably suppressed spontaneous EEG power in parietal and occipital areas and extended this inhibitory influence into temporal and frontal cortices, highlighting a genuinely global modulatory capacity.

Importantly, the observed neural entrainment emerged rapidly: even brief, 60-second exposures to binaural-beat stimulation produced measurable increases in phase coherence that persisted and compounded over successive blocks. This cumulative effect underscores the capacity of the thalamo-cortical network to lock onto externally imposed rhythms even under low-duration protocols, thereby accelerating the onset of relaxation. Such rapid entrainment not only confirms the feasibility of short-duration neuromodulation but also suggests practical applications in contexts where time constraints or subject tolerance limit prolonged exposure.

The spatial distribution of entrainment further revealed that neighboring cortical regions synchronize readily, as expected, but that homologous areas across hemispheres also exhibit significant coherence increases. Moreover, distal sites—such as frontal poles, which are conventionally considered less amenable to alpha-band

modulation—demonstrated clear phase alignment with posterior areas. These findings challenge the prevailing assumption that alpha-entrainment effects remain confined to parieto-occipital sources and open the possibility that broader networks can be engaged via auditory stimulation.

At the individual level, substantial heterogeneity was evident in both the features selected for classification and the temporal dynamics of response. Some participants exhibited rapid and robust entrainment, while others required multiple exposures to reach comparable coherence levels. This variability likely reflects anatomical differences—such as skull conductivity and cortical folding patterns—and functional factors, including baseline alpha power and attentional state. Consequently, the SVM classifier's accuracy varied markedly across subjects, and its generalizability was limited when trained on a pooled dataset.

Indeed, the limited generalizability of the SVM underscores the necessity for subject-specific models. Given the sparse eight-electrode montage deployed, the classifier could sample only a fraction of the cortical manifold, making its performance highly sensitive to individual electrode–brain configurations. This constraint highlights the importance of dense coverage for future applications and suggests that personalized calibration of detection algorithms is essential when using low-density EEG systems. Despite these limitations, the temporal progression of classifier performance revealed two salient trends. First, recognition accuracy for binaural-beat blocks increased progressively across the session, suggesting either residual entrainment that carried over between blocks or a rapid habituation that sharpened neural responsiveness to the stimulus. Second, recognition of sham blocks declined over time, providing direct evidence of carry-over effects that reduce sensitivity to sham conditions. Together, these patterns emphasize that alternating protocols induce not only acute but also cumulative effects that must be considered when designing neuromodulation interventions.

6.2 Future Developments

Building on these results, several avenues for future research emerge. A primary goal should be to identify the minimal stimulation duration capable of eliciting a robust, reproducible alpha-entrainment effect across a heterogeneous subject pool. Systematic variation of block length—coupled with high-temporal-resolution measures of phase coherence—would elucidate the dose–response relationship and optimize protocol efficiency.

Enlarging the population is fundamental to minimizing subject-specific biases

and achieving the widest possible generalizability of the results. By recruiting individuals across diverse age ranges, gender identities, and neurophysiological profiles, the study can better account for inter-individual variability in alpha-band responsiveness. A larger sample size also increases statistical power, enabling the detection of subtle effects that may be obscured in smaller cohorts. Moreover, broader inclusion criteria facilitate the identification of subgroups with distinct entrainment patterns, thereby informing personalized stimulation protocols. Ultimately, a more extensive and heterogeneous participant pool will strengthen the external validity of the findings and support the development of universally applicable neuromodulation tools.

In parallel, increasing the density of EEG coverage—from eight electrodes to a high-density ($\geq$ 64 channels) array—will enable comprehensive mapping of network-level entrainment patterns. Denser montages will mitigate the confounding influence of individual skull and brain morphology, as more electrodes can capture signal from regions with optimal conductivity. Moreover, full-scalp recordings will facilitate source-level analyses, revealing the interplay between cortical generators and allowing for more precise localization of entrainment effects.

These methodological improvements will pave the way for developing a universal classification framework capable of detecting the presence of binaural-beat entrainment in real time, regardless of individual differences. By leveraging large datasets, transfer learning techniques, and individualized calibration procedures, it should be possible to train a single model that adapts dynamically to each user's individual alpha frequency (IAF). Such a system could operate in closed-loop fashion—continuously monitoring EEG and adjusting stimulus parameters to sustain optimal entrainment—thereby delivering targeted relaxation on demand.

In conclusion, this work lays the groundwork for next-generation neuromodulation tools that combine the rapid onset and global reach of alpha-band stimulation with adaptive, personalized algorithms. Through optimized protocols, expanded populations, and advanced analytics, future studies can transform binaural-beat entrainment from a promising experimental paradigm into a clinically viable and user-friendly technology for stress reduction, wellness promotion, and beyond.

Bibliography

[1] Alistair Farley, Carolyn Johnstone, Charles Hendry, and Ella McLafferty. «Nervous system: part 1». In: *Nursing Standard* 28.31 (Apr. 2014), pp. 46–51. ISSN: 2047-9018. DOI: 10.7748/ns2014.04.28.31.46.e7004. URL: http://dx.doi.org/10.7748/ns2014.04.28.31.46.e7004 (cit. on p. 1).

[2] Javed, Kinaan and Reddy, Vamsi and Lui, Forshing. «Neuroanatomy, cerebral cortex». en. In: *StatPearls*. Treasure Island (FL): StatPearls Publishing, Jan. 2025 (cit. on pp. 1, 2).

[3] https://www.researchgate.net/publication/361467779_Alessio_Scarito_La_cognizione_della_lingua_Psicolinguistica_ed_embodied_cognition_a_supporto_della_didattica_dell'italiano_nelle_scuole_secondarie_di_primo_grado/figures?lo=1. Accessed: 2025-7-15 (cit. on p. 2).

[4] https://cdn.idntimes.com/content-images/post/20220301/gray-and-white-matter-0535b6da1436b74336d6c76ec323e816.jpg. Accessed: 2025-6-3 (cit. on p. 3).

[5] Mark F Bear, Barry W Connors, and Michael A Paradiso. *Neuroscience*. 4th ed. Philadelphia, PA: Lippincott Williams and Wilkins, Feb. 2015 (cit. on p. 3).

[6] https://www.wikiwand.com/es/articles/Surco_(neuroanatomÃŋa). Accessed: 2025-6-3 (cit. on p. 3).

[7] M. Ángeles Fernández-Gil, R. Palacios-Bote, M. Leo-Barahona, and J.P. Mora-Encinas. «Anatomy of the Brainstem: A Gaze Into the Stem of Life». In: *Seminars in Ultrasound, CT and MRI* 31.3 (June 2010), pp. 196–219. ISSN: 0887-2171. DOI: 10.1053/j.sult.2010.03.006. URL: http://dx.doi.org/10.1053/j.sult.2010.03.006 (cit. on p. 4).

[8] Sopiko Jimsheleishvili and Marine Dididze. «Neuroanatomy, cerebellum». en. In: *StatPearls*. Treasure Island (FL): StatPearls Publishing, Jan. 2025 (cit. on p. 4).

[9] Tyler J Torrico and Sunil Munakomi. «Neuroanatomy, thalamus». en. In: *StatPearls*. Treasure Island (FL): StatPearls Publishing, Jan. 2025 (cit. on p. 4).

[10] Carly B Young, Vamsi Reddy, and James Sonne. «Neuroanatomy, basal ganglia». en. In: *StatPearls*. Treasure Island (FL): StatPearls Publishing, Jan. 2025 (cit. on p. 4).

[11] *10.1: Neurons and glial cells*. en. https://bio.libretexts.org/Bookshelves/Human_Biology/Human_Anatomy_Lab/10:_Nervous_Tissue/10.01:_Neurons_and_Glial_Cells. Accessed: 2025-1-27. June 2021 (cit. on p. 5).

[12] https://opentextbc.ca/biology/chapter/16-1-neurons-and-glial-cells/. Accessed: 2025-1-27 (cit. on p. 5).

[13] Michael J Caire, Vamsi Reddy, and Matthew A Varacallo. «Physiology, synapse». en. In: *StatPearls*. Treasure Island (FL): StatPearls Publishing, Jan. 2025 (cit. on pp. 6, 7).

[14] *Synapses*. https://theory.labster.com/synapses/. Accessed: 2025-5-8 (cit. on p. 6).

[15] *Google Search*. it. https://www.google.com/search?vsrid=CK2JidiXkIScExACGAEiJDQ4NjhmZGUzLTFmMTItNGUzNi04YzVlLTc2ZjU3ZmZmYjE3MjIGIgJsdSgBOJaAqfTPwY4D&vsint=CAIqDAoCCAcSAggKGAEgATojChYNAAAAPxUAAAA_HQAAgD8lAACAPzABEPcEGJgDJQAAgD8&udm=26&lns_mode=un&source=lns.web.gisbubb&vsdim=631,408&gsessionid=KK5pV4WXNI47Vjmppn6g3TxhtVSEn53fzDNh2tj0_d9qK-V8u6WdJQ&lsessionid=PpNFfIt2FwNQBjO1NKNtxBH5p0pn-nhJ1SsEv87GQ7w1c-dFu_2Clw&lns_surface=26&authuser=0&lns_vfs=e&qsubts=1752677345583&biw=1536&bih=695&hl=it. Accessed: 2025-7-16 (cit. on p. 6).

[16] Appaji Rayi and Najib I Murr. «Electroencephalogram». en. In: *StatPearls*. Treasure Island (FL): StatPearls Publishing, Jan. 2025 (cit. on pp. 7, 9).

[17] Vítor M. *Interfaces Cerebrais – O controlo pela mente*. pt. https://pplware.sapo.pt/high-tech/interfaces-cerebrais-o-controlo-pela-mente/. Accessed: 2025-6-4. June 2014 (cit. on p. 7).

[18] https://iastate.pressbooks.pub/curehumanphysiology/chapter/eeg/. Accessed: 2025-6-5 (cit. on p. 8).

[19] Sándor Beniczky and Donald L Schomer. «Electroencephalography: basic biophysical and technological aspects important for clinical applications». en. In: *Epileptic Disord.* 22.6 (Dec. 2020), pp. 697–715 (cit. on pp. 9, 10).

[20] Sophie Apprich. *Multimodal fNIRS-EEG measurements — Integration on the head*. en. https://www.artinis.com/blogpost-all/2023/multimodal-fnirs-eeg-measurements-integration-on-the-head. Accessed: 2025-5-9. June 2023 (cit. on p. 10).

[21] Ernst Niedermeyer and Fernando Lopes da Silva. *Electroencephalography: Basic Principles, Clinical Applications, and Related Fields*. Lippincott Williams & Wilkins, 2005 (cit. on p. 10).

[22] Bruce J Fisch. *Practical Guide for Clinical Neurophysiologic Testing: EEG*. Lippincott Williams & Wilkins, 1999 (cit. on p. 11).

[23] Fabien Lotte, Marco Congedo, Anatole Lécuyer, François Lamarche, and Bruno Arnaldi. «A review of classification algorithms for EEG-based brain–computer interfaces: a 10 year update». In: *Journal of neural engineering* 15.3 (2018), p. 031005 (cit. on p. 11).

[24] Christoph M Michel, Micah M Murray, Géraldine Lantz, Silvia Gonzalez, Luigi Spinelli, and Rolando Grave de Peralta. «EEG source imaging». In: *Clinical neurophysiology* 115.10 (2004), pp. 2195–2222 (cit. on p. 11).

[25] https://www.researchgate.net/figure/The-type-of-EEG-channels-Bipolar-type-top-and-unipolar-type-or-monopolar-bottom_fig4_358241749. Accessed: 2025-6-6 (cit. on p. 11).

[26] Chetan S Nayak and Arayamparambil C Anilkumar. «EEG normal waveforms». en. In: *StatPearls*. Treasure Island (FL): StatPearls Publishing, Jan. 2025 (cit. on p. 12).

[27] Alamy Limited. *Brain waves oscillating electric voltage Delta, Theta, Alpha, Beta, Gamma vector infographic illustration chart, brain neurons activity study*. en. https://www.alamy.com/brain-waves-oscillating-electric-voltage-delta-theta-alpha-beta-gamma-vector-infographic-illustration-chart-brain-neurons-activity-study-image503840463.html. Accessed: 2025-4-29 (cit. on p. 13).

[28] R. Chaudhry, J. H. Miao, and A. Rehman. «Physiology, Cardiovascular». In: *StatPearls* (2022) (cit. on p. 13).

[29] J. G. Betts. *Anatomy & Physiology*. 2013 (cit. on p. 13).

[30] IQWiG. *In brief: How does the blood circulatory system work?* 2023 (cit. on p. 13).

[31] R. Chaudhry, J. H. Miao, and A. Rehman. «Physiology, Cardiac». In: *StatPearls* (2022) (cit. on p. 13).

[32] *El sistema circulatorio: sus 4 partes principales y cómo funcionan*. es. https://es.fusedlearning.com/circulatory-system. Accessed: 2025-6-9 (cit. on p. 14).

[33] Robert H Whitaker. «Anatomy of the heart». en. In: *Medicine (Abingdon)* 38.7 (July 2010), pp. 333–335 (cit. on pp. 14, 15).

[34] *Anatomia macroscopica del cuore, sistema circolatorio e circolazione coronarica*. it. https://medicinaonline.co/2022/05/02/anatomia-macroscopica-del-cuore-sistema-circolatorio-e-circolazione-coronarica/. Accessed: 2025-7-16. May 2022 (cit. on p. 15).

[35] A C Guyton, T G Coleman, and H J Granger. «Circulation: overall regulation». en. In: *Annu. Rev. Physiol.* 34.1 (1972), pp. 13–46 (cit. on pp. 15, 16).

[36] U F O Themes. *Lymphatic system*. en. https://basicmedicalkey.com/lymphatic-system/. Accessed: 2025-6-9. May 2016 (cit. on p. 16).

[37] Yasar Sattar and Lovely Chhabra. «Electrocardiogram». en. In: *StatPearls*. Treasure Island (FL): StatPearls Publishing, Jan. 2025 (cit. on pp. 16, 17, 19).

[38] *Electrocardiograph (1903)*. https://1001inventionsinfo.blogspot.com/2021/01/electrocardiograph-1903-einthovens.html. Accessed: 2025-6-12. Jan. 2021 (cit. on p. 17).

[39] *Basic Cardiac Electrophysiology and ECG Concepts_20120902_*. en. https://www.slideshare.net/thrs/basic-cardiac-electrophysiology-and-ecg-concepts20120902. Accessed: 2025-6-12 (cit. on p. 18).

[40] Paul Kligfield et al. «Recommendations for the standardization and interpretation of the electrocardiogram: part I: The electrocardiogram and its technology: a scientific statement from the American Heart Association Electrocardiography and Arrhythmias Committee, Council on Clinical Cardiology; the American College of Cardiology Foundation; and the Heart Rhythm Society: endorsed by the International Society for Computerized Electrocardiology». en. In: *Circulation* 115.10 (Mar. 2007), pp. 1306–1324 (cit. on pp. 17, 18).

[41] https://www.researchgate.net/figure/Normal-ECG-signal-with-his-different-features_fig1_299575422. Accessed: 2025-4-30 (cit. on p. 19).

[42] Yasar Sattar and Lovely Chhabra. «Electrocardiogram». en. In: *StatPearls*. Treasure Island (FL): StatPearls Publishing, Jan. 2025 (cit. on p. 20).

[43] Sridhar Srinivasan, Andreas Keil, Kyle Stratis, Aaron F Osborne, Colin Cerwonka, Jennifer Wong, Brenda L Rieger, Valerie Polcz, and David W Smith. «Interaural attention modulates outer hair cell function». en. In: *Eur. J. Neurosci.* 40.12 (Dec. 2014), pp. 3785–3792 (cit. on p. 20).

[44] Rodrigo Donoso-San Martín, Alexis Leiva, Constantino D Dragicevic, Vicente Medel, and Paul H Delano. «The corticofugal oscillatory modulation of the cochlear receptor during auditory and visual attention is preserved in tinnitus». en. In: *Front. Neural Circuits* 17 (2023), p. 1301962 (cit. on p. 20).

[45] Gregory Hickok and David Poeppel. «Dorsal and ventral streams: a framework for understanding aspects of the functional anatomy of language». en. In: *Cognition* 92.1-2 (May 2004), pp. 67–99 (cit. on p. 20).

[46] Srinivasa P Kommajosyula, Edward L Bartlett, Rui Cai, Lynne Ling, and Donald M Caspary. «Corticothalamic projections deliver enhanced responses to medial geniculate body as a function of the temporal reliability of the stimulus». en. In: *J. Physiol.* 599.24 (Dec. 2021), pp. 5465–5484 (cit. on p. 20).

[47] *Dalle vibrazioni dell' aria all' esperienza uditiva*. it. `https://www.peopleandneuroscience.it/libri-e-altri-scritti/dalle-vibrazioni-dell-aria-all-esperienza-uditiva`. Accessed: 2025-5-2 (cit. on p. 21).

[48] G Oster. «Auditory beats in the brain». en. In: *Sci. Am.* 229.4 (Oct. 1973), pp. 94–102 (cit. on pp. 22, 61).

[49] Hillel Pratt, Arnold Starr, Henry J Michalewski, Andrew Dimitrijevic, Naomi Bleich, and Nomi Mittelman. «Cortical evoked potentials to an auditory illusion: binaural beats». en. In: *Clin. Neurophysiol.* 120.8 (Aug. 2009), pp. 1514–1524 (cit. on p. 22).

[50] J S Wernick and A Starr. «Binaural interaction in the superior olivary complex of the cat: an analysis of field potentials evoked by binaural-beat stimuli». en. In: *J. Neurophysiol.* 31.3 (May 1968), pp. 428–441 (cit. on p. 22).

[51] G Oster. «Auditory beats in the brain». en. In: *Sci. Am.* 229.4 (Oct. 1973), pp. 94–102 (cit. on pp. 22, 24).

[52] Marco Solcà, Anaıs Mottaz, and Adrian G Guggisberg. «Binaural beats increase interhemispheric alpha-band coherence between auditory cortices». en. In: *Hear. Res.* 332 (Feb. 2016), pp. 233–237 (cit. on pp. 23, 26, 65).

[53] Helané Wahbeh, Carlo Calabrese, and Heather Zwickey. «Binaural beat technology in humans: a pilot study to assess psychologic and physiologic effects». en. In: *J. Altern. Complement. Med.* 13.1 (Jan. 2007), pp. 25–32 (cit. on p. 23).

[54] Donna D Zampi. «Efficacy of theta binaural beats for the treatment of chronic pain». en. In: *Altern. Ther. Health Med.* 22.1 (Jan. 2016), pp. 32–38 (cit. on p. 23).

[55] Jakub Kraus, Katedra psychologie, Fakulta sociálních studií, Masarykova Univerzita Joštova 10, 602 00 Brno, Czech Republic, Michaela Porubanová, and Farmingdale State College - SUNY, Farmingdale, New York, USA. «The effect of binaural beats on working memory capacity». In: *Stud. Psychol. (Bratisl.)* 57.2 (2015), pp. 135–145 (cit. on p. 23).

[56] J C R Licklider, J C Webster, and J M Hedlun. «On the frequency limits of binaural beats». en. In: *J. Acoust. Soc. Am.* 22.4 (July 1950), pp. 468–473 (cit. on p. 23).

[57] Salomé Sudre, Richard Kronland-Martinet, Laetitia Petit, Jocelyn Rozé, Sølvi Ystad, and Mitsuko Aramaki. «A new perspective on binaural beats: Investigating the effects of spatially moving sounds on human mental states». en. In: *PLoS One* 19.7 (July 2024), e0306427 (cit. on p. 23).

[58] Tina L Huang and Christine Charyton. «A comprehensive review of the psychological effects of brainwave entrainment». en. In: *Altern. Ther. Health Med.* 14.5 (Sept. 2008), pp. 38–50 (cit. on pp. 24, 54).

[59] D W F Schwarz and P Taylor. «Human auditory steady state responses to binaural and monaural beats». en. In: *Clin. Neurophysiol.* 116.3 (Mar. 2005), pp. 658–668 (cit. on p. 24).

[60] Rossitza Draganova, Bernhard Ross, Andreas Wollbrink, and Christo Pantev. «Cortical steady-state responses to central and peripheral auditory beats». en. In: *Cereb. Cortex* 18.5 (May 2008), pp. 1193–1200 (cit. on p. 24).

[61] Ruth Maria Ingendoh, Ella S Posny, and Angela Heine. «Binaural beats to entrain the brain? A systematic review of the effects of binaural beat stimulation on brain oscillatory activity, and the implications for psychological research and intervention». en. In: *PLoS One* 18.5 (May 2023), e0286023 (cit. on pp. 24, 25).

[62] Mahmut Taha Ölçücü, Kayhan Yılmaz, Kaan Karamık, Yahya Okuducu, Çağatay Özsoy, Yasin Aktaş, Serdar Çakır, and Mutlu Ateş. «Effects of listening to binaural beats on anxiety levels and pain scores in male patients undergoing cystoscopy and ureteral Stent removal: A randomized placebo-controlled trial». en. In: *J. Endourol.* 35.1 (Jan. 2021), pp. 54–61 (cit. on p. 25).

[63] B K Isik, A Esen, B Büyükerkmen, A Kilinç, and D Menziletoglu. «Effectiveness of binaural beats in reducing preoperative dental anxiety». en. In: *Br. J. Oral Maxillofac. Surg.* 55.6 (July 2017), pp. 571–574 (cit. on p. 25).

[64] Werner Schmid, Peter Marhofer, Philipp Opfermann, Markus Zadrazil, Oliver Kimberger, Lydia Triffterer, Daniela Marhofer, and Wolfgang Klug. «Brainwave entrainment to minimise sedative drug doses in paediatric surgery: a randomised controlled trial». en. In: *Br. J. Anaesth.* 125.3 (Sept. 2020), pp. 330–335 (cit. on p. 25).

[65] Maurício da Silva Junior, Rafaela Covello de Freitas, Wellington Pinheiro dos Santos, Washington Wagner Azevedo da Silva, Marcelo Cairrão Araújo Rodrigues, and Erick Francisco Quintas Conde. «Exploratory study of the effect of binaural beat stimulation on the EEG activity pattern in resting state using artificial neural networks». en. In: *Cogn. Syst. Res.* 54 (May 2019), pp. 1–20 (cit. on p. 25).

[66] D Vernon, G Peryer, J Louch, and M Shaw. «Tracking EEG changes in response to alpha and beta binaural beats». en. In: *Int. J. Psychophysiol.* 93.1 (July 2014), pp. 134–139 (cit. on p. 25).

[67] Elham Shamsi, Mohammad Ali Ahmadi-Pajouh, and Tirdad Seifi Ala. «Higuchi fractal dimension: An efficient approach to detection of brain entrainment to theta binaural beats». en. In: *Biomed. Signal Process. Control* 68.102580 (July 2021), p. 102580 (cit. on p. 25).

[68] Shotaro Karino, Masato Yumoto, Kenji Itoh, Akira Uno, Keiko Yamakawa, Sotaro Sekimoto, and Kimitaka Kaga. «Neuromagnetic responses to binaural beat in human cerebral cortex». en. In: *J. Neurophysiol.* 96.4 (Oct. 2006), pp. 1927–1938 (cit. on p. 25).

[69] C. Kasprzak. «Influence of Binaural Beats on EEG Signal». In: *International Journal of Psychophysiology* 79 (2011), pp. 1–9 (cit. on p. 25).

[70] Christos I. Ioannou, Ernesto Pereda, Job P. Lindsen, and Joydeep Bhattacharya. «Electrical Brain Responses to an Auditory Illusion and the Impact of Musical Expertise». In: *PLoS ONE* 10.6 (2015), e0129486. DOI: 10.1371/journal.pone.0129486 (cit. on p. 26).

[71] D Vernon, G Peryer, J Louch, and M Shaw. «Tracking EEG changes in response to alpha and beta binaural beats». en. In: *Int. J. Psychophysiol.* 93.1 (July 2014), pp. 134–139 (cit. on p. 26).

[72] César E Corona-González, Luz María Alonso-Valerdi, and David I Ibarra-Zarate. «Personalized theta and beta binaural beats for brain entrainment: An electroencephalographic analysis». en. In: *Front. Psychol.* 12 (Nov. 2021), p. 764068 (cit. on p. 26).

[73] Elizabeth Krasnoff and Gaétan Chevalier. «Case report: binaural beats music assessment experiment». en. In: *Front. Hum. Neurosci.* 17 (May 2023), p. 1138650 (cit. on p. 26).

[74] B Brady and L Stevens. «Binaural-beat induced theta EEG activity and hypnotic susceptibility». en. In: *Am. J. Clin. Hypn.* 43.1 (July 2000), pp. 53–69 (cit. on p. 26).

[75] Xiang Gao, Hongbao Cao, Dong Ming, Hongzhi Qi, Xuemin Wang, Xiaolu Wang, Runge Chen, and Peng Zhou. «Analysis of EEG activity in response to binaural beats with different frequencies». en. In: *Int. J. Psychophysiol.* 94.3 (Dec. 2014), pp. 399–406 (cit. on pp. 27, 64, 73).

[76] Thomas Mitchell. *Machine Learning*. en. McGraw-Hill series in computer science. New York, NY: McGraw-Hill Professional, Mar. 1997 (cit. on p. 28).

[77] M I Jordan and T M Mitchell. «Machine learning: Trends, perspectives, and prospects». en. In: *Science* 349.6245 (July 2015), pp. 255–260 (cit. on p. 28).

[78] Trevor Hastie, Robert Tibshirani, and Jerome Friedman. *The elements of statistical learning*. en. 2nd ed. Springer series in statistics. New York, NY: Springer, Feb. 2009 (cit. on p. 28).

[79] Kevin P Murphy. *Machine Learning*. en. Adaptive Computation and Machine Learning series. London, England: MIT Press, Aug. 2012 (cit. on p. 28).

[80] Leo Breiman. In: *Mach. Learn.* 45.1 (2001), pp. 5–32 (cit. on p. 29).

[81] Corinna Cortes and Vladimir Vapnik. «Support-vector networks». In: *Machine learning* 20.3 (1995), pp. 273–297 (cit. on pp. 30–32).

[82] M.A. Aizerman, E.M. Braverman, and L.I. Rozonoer. «Theoretical foundations of the potential function method in pattern recognition learning». In: *Automation and Remote Control* 25 (1964), pp. 821–837 (cit. on p. 31).

[83] Vladimir N. Vapnik. *Estimation of Dependencies Based on Empirical Data*. Springer-Verlag, 1982 (cit. on p. 31).

[84] Léon Bottou et al. «Comparison of classifier methods: A case study in handwritten digit recognition». In: *International Conference on Pattern Recognition*. 1994 (cit. on p. 32).

[85] *Enobio 8*. en. `https://www.neuroelectrics.com/products/research/enobio/enobio8`. Accessed: 2025-4-28 (cit. on pp. 33–37).

[86] *Neurgel - gel conduttivo*. it. `https://www.geasoluzioni.it/prodotti/biofeedback-e-monitoraggio/neurofeedback-digitrack-3/850-gel-conduttivo-neurgel.html`. Accessed: 2025-4-29 (cit. on p. 35).

[87] *FIAB*. `https://www.fiab.it/en/category.php?id=21`. Accessed: 2025-4-29 (cit. on p. 36).

[88] *Manuals - enobio*. en. `https://www.neuroelectrics.com/manuals-enobio`. Accessed: 2025-4-30 (cit. on pp. 38–41).

[89] *Manuale JBL Tune 660NC (Italiano - 22 pagine)*. it. https://www.manualeduso.it/jbl/tune-660nc/manuale?p=2&file=1293724. Accessed: 2025-5-2 (cit. on pp. 41, 42).

[90] *Polar H10*. it. https://www.polar.com/it/sensors/h10-heart-rate-sensor. Accessed: 2025-5-2 (cit. on pp. 42, 43).

[91] https://it.mathworks.com/products/matlab.html. Accessed: 2025-5-4 (cit. on p. 44).

[92] Henry Schein, Inc. *Monoject curved syringes - Henry Schein Dental*. en. https://www.henryschein.com/monoject-syringe-curved.aspx?msockid=37f19e6d1f316ea729068a9c1eec6f36. Accessed: 2025-5-9 (cit. on p. 45).

[93] Bo Hjorth. «EEG analysis based on time domain properties». en. In: *Electroencephalogr. Clin. Neurophysiol.* 29.3 (Sept. 1970), pp. 306–310 (cit. on p. 54).

[94] T Higuchi. «Approach to an irregular time series on the basis of the fractal theory». en. In: *Physica D* 31.2 (June 1988), pp. 277–283 (cit. on p. 56).

[95] Hiie Hinrikus, Maie Bachmann, Deniss Karai, Włodzimierz Klonowski, Jaanus Lass, Pavel Stepien, Robert Stepien, and Viiu Tuulik. «Higuchi's fractal dimension for analysis of the effect of external periodic stressor on electrical oscillations in the brain». en. In: *Med. Biol. Eng. Comput.* 49.5 (May 2011), pp. 585–591 (cit. on p. 56).

[96] Michael J Katz. «Fractals and the analysis of waveforms». en. In: *Comput. Biol. Med.* 18.3 (Jan. 1988), pp. 145–156 (cit. on p. 57).

[97] A Petrosian. «Kolmogorov complexity of finite sequences and recognition of different preictal EEG patterns». In: *Proceedings Eighth IEEE Symposium on Computer-Based Medical Systems*. Lubbock, TX, USA: IEEE Comput. Soc. Press, 2002 (cit. on p. 58).

[98] Christoph Bandt and Bernd Pompe. «Permutation entropy: a natural complexity measure for time series». en. In: *Phys. Rev. Lett.* 88.17 (Apr. 2002), p. 174102 (cit. on p. 60).

[99] Wolfgang Klimesch. «EEG alpha and theta oscillations reflect cognitive and memory performance: a review and analysis». en. In: *Brain Res. Rev.* 29.2-3 (Apr. 1999), pp. 169–195 (cit. on p. 61).

[100] Satu Palva and J Matias Palva. «New vistas for alpha-frequency band oscillations». en. In: *Trends Neurosci.* 30.4 (Apr. 2007), pp. 150–158 (cit. on p. 61).

[101] D Corydon Hammond. «Neurofeedback treatment of depression and anxiety». en. In: *J. Adult Dev.* 12.2-3 (Aug. 2005), pp. 131–137 (cit. on p. 62).

[102] Bahar Güntekin and Erol Başar. «Review of evoked and event-related delta responses in the human brain». en. In: *Int. J. Psychophysiol.* 103 (May 2016), pp. 43–52 (cit. on p. 62).

[103] J-A Micoulaud-Franchi, A McGonigal, R Lopez, C Daudet, I Kotwas, and F Bartolomei. «Electroencephalographic neurofeedback: Level of evidence in mental and brain disorders and suggestions for good clinical practice». en. In: *Neurophysiol. Clin.* 45.6 (Dec. 2015), pp. 423–433 (cit. on p. 62).

[104] Tato M Sokhadze, Christopher M Stewart, and Michael Hollifield. «Integrating cognitive neuroscience research and cognitive behavioral treatment with neurofeedback therapy in drug addiction comorbid with posttraumatic stress disorder: A conceptual review». en. In: *J. Neurother.* 11.2 (July 2007), pp. 13–44 (cit. on p. 62).

[105] Yingjie Li, Shanbao Tong, Dan Liu, Yi Gai, Xiuyuan Wang, Jijun Wang, Yihong Qiu, and Yisheng Zhu. «Abnormal EEG complexity in patients with schizophrenia and depression». en. In: *Clin. Neurophysiol.* 119.6 (June 2008), pp. 1232–1241 (cit. on p. 63).

[106] C E Shannon. «A mathematical theory of communication». In: *Bell Syst. Tech. J.* 27.3 (July 1948), pp. 379–423 (cit. on p. 63).

[107] Maryam Sadeghijam, Saeed Talebian, Samer Mohsen, Mehdi Akbari, and Akram Pourbakht. «Shannon entropy measures for EEG signals in tinnitus». en. In: *Neurosci. Lett.* 762.136153 (Sept. 2021), p. 136153 (cit. on p. 63).

[108] Ramesh Srinivasan, William R Winter, Jian Ding, and Paul L Nunez. «EEG and MEG coherence: measures of functional connectivity at distinct spatial scales of neocortical dynamics». en. In: *J. Neurosci. Methods* 166.1 (Oct. 2007), pp. 41–52 (cit. on p. 64).

[109] J P Lachaux, E Rodriguez, J Martinerie, and F J Varela. «Measuring phase synchrony in brain signals». en. In: *Hum. Brain Mapp.* 8.4 (1999), pp. 194–208 (cit. on p. 64).

[110] Sergul Aydore, Dimitrios Pantazis, and Richard M Leahy. «A note on the phase locking value and its properties». en. In: *Neuroimage* 74 (July 2013), pp. 231–244 (cit. on p. 64).

[111] Peter Goodin, Joseph Ciorciari, Kate Baker, Anne-Marie Carey, Michelle Harper, and Jordy Kaufman. «A high-density EEG investigation into steady state binaural beat stimulation». en. In: *PLoS One* 7.4 (Apr. 2012), e34789 (cit. on p. 66).

[112] Helané Wahbeh, Carlo Calabrese, and Heather Zwickey. «Binaural beat technology in humans: a pilot study to assess psychologic and physiologic effects». en. In: *J. Altern. Complement. Med.* 13.1 (Jan. 2007), pp. 25–32 (cit. on pp. 66, 67).

[113] Fred Shaffer and J P Ginsberg. «An overview of heart rate variability metrics and norms». In: *Front. Public Health* 5 (Sept. 2017) (cit. on p. 67).

[114] Patrick A McConnell, Brett Froeliger, Eric L Garland, Jeffrey C Ives, and Gary A Sforzo. «Auditory driving of the autonomic nervous system: Listening to theta-frequency binaural beats post-exercise increases parasympathetic activation and sympathetic withdrawal». en. In: *Front. Psychol.* 5 (Nov. 2014), p. 1248 (cit. on p. 68).

[115] S I Gonçalves et al. «Correlating the alpha rhythm to BOLD using simultaneous EEG/fMRI: inter-subject variability». en. In: *Neuroimage* 30.1 (Mar. 2006), pp. 203–213 (cit. on p. 74).